DESIGN AND DEVELOPMENT OF 2D MATERIALS BASED NANOCOMPOSITES

BY

AKASH SINGH

DISSERTATION

Submitted in partial fulfillment of the requirements
for the degree of Doctor of Philosophy in Systems and Entrepreneurial Engineering
in the Graduate College of the
University of Illinois Urbana-Champaign, 2024

Urbana, Illinois

Doctoral Committee:

Assistant Professor Yumeng Li, Chair and Director of Research
Professor Pingfeng Wang
Associate Professor Girish Krishnan
Associate Professor Qing Cao

Abstract

In the forefront of materials science, 2D materials have emerged as a captivating research domain over the past two decades. Among these, graphene stands out as an exceptional 2D material with distinctive mechanical, thermal, and electrical properties, making it a critical component in applications spanning lightweight structural materials, versatile coatings, and flexible electronics. However, the high cost and complexity of experimental investigations have driven the adoption of computational simulations, particularly molecular dynamics (MD), to unveil the underlying microscopic origins of graphene's unique properties. Yet, such simulations have yielded varying results, owing to the use of diverse empirical interatomic potentials used in these MD simulations.

This dissertation aims to create an accurate interatomic potentials for 2D materials like graphene by using an artificial neural network (ANN)-based interatomic potential. These ANN based machine learning interatomic potentials for graphene are trained from the training data developed using first-principle based atomistic simulations. Machine learning potential (MLP) helps us to run high-fidelity Molecular Dynamics (MD) simulations approaching the accuracy of first principle simulations but with a fraction of computational cost. These MLP enables larger-scale simulations and extended timeframes, thereby accelerating the design, development and discovery of novel graphene/graphene based nanomaterials. Also, this dissertation aims to showcase MLP's capability in estimating critical material properties of graphene, including coefficient of thermal expansion (CTE), lattice parameters, Young's modulus, yield strength with comparable accuracy of that of experimental and first-principle calculations found from previous literatures. Remarkably, MLP's capability in capturing dominant mechanisms governing the behaviour of CTE in graphene, including effects of changing lattice parameters and increasing/decreasing out-of-plane rippling with temperature, is a significant highlight of this dissertation. Furthermore, this MLP development method can be extended to other 2D materials, promising to expedite research on novel 2D materials and their unique atomic structures.

Moving on to 2D materials-based nanocomposites, in today's scientific and technological landscape, have assumed a position of significant importance. These hybrid material systems merge organic molecules with inorganic 2D materials, creating a new dimension of functional materials with varied applications i.e. materials for photovoltaics, electronics, nanotribology to aerospace applications. The interfaces between these 2D material and polymers serves as prototype material systems for studying confinement-induced phase transitions in 2D material based nanocomposites. Thorough understanding of dynamic and static behaviour of atoms in these interfaces at small length (nanometers) and time scales (nanoseconds) is critical as it material behaviour at this scale dictates overall material property of the resulting material system. Thus understanding the interfacial behaviour at atomic level will lead in the development of deliberately engineered 2D material and polymer based nanocomposites. But till date, the complexities of experimental testing at these small length and time scales as well as theoretical modeling have hindered a comprehensive understanding of these hetero-interfaces and thereby our ability to use these materials for practical purposes.

To address this issues, this dissertation aims to understand the behaviour of 2D material and polymer at these interfaces using molecular dynamics (MD) simulations. By conducting MD simulations we focus on the assembly of polyethylene chains on surface of two dimensional $MoSe_2$ sheet (which serves as a representative material system in this study to analyse the behaviour of 2D material based nanocomposites). All-atom models were created to simulate the dynamic assembly of n-pentacosane chains, which serves as a proxy for polyethylene in this study, on the surface of two dimensional $MoSe_2$ sheet. This study reveals that polyethylene molecules starts crystallizing from 2D $MoSe_2$-polyethylene interface and the crystallization growth front (plane of crystallized polymer chains) moves quickly towards the bulk polyethylene chains starting from the 2D material-polymer interface. At equilibrium, the directional registry of polyethylene chains on the 2D material surface happens through the interplay of free energy of the surface, adhesive interfacial interactions, conformational entropy, and the presence of substrate corrugation. The results suggests the potential of 2D materials, such as $MoSe_2$, as a template for creating 2D material-polymer nanocomposites with specific crystallization orientations creating deliberate anisotropy and thereby resulting in a material system with tunable material properties.

To my teachers, family and friends for their continuous love and support all the way

Acknowledgments

Firstly I would like to extend my heartfelt thanks to my adviser, Dr. Yumeng Li, who went through my numerous revisions during thesis writing. She also helped me make sense of things, at every step, whenever I had confusions and doubts throughout my PhD. Also I want to extend my thanks to my committee members, Dr. Pingfeng Wang, Dr. Girish Krishnan and Dr. Qing Cao who offered guidance and support. And finally, I want like to thank my wife Annie, my parents and my pet dog/son hamburger who endured this long process with me, always offering support and love.

Publication Note

Most of the work in this thesis is already published primarily in these three journal articles authored by me i.e. (a) "Reliable machine learning potentials based on artificial neural network for graphene" https://doi.org/10.1016/j.commatsci.2023.112272 (b) "Templating Effect of $MoSe_2$ on Crystallization of Polyethylene: A Molecular Dynamics Simulation Study" https://doi.org/10.1021/acs.jpcc.3c06850 (c) "Atomic Edge-Guided Polyethylene Crystallization on Monolayer Two-Dimensional Materials" https://doi.org/10.1021/acs.macromol.1c01978. Generative AI has been used to improve the writing quality of this thesis in some sections of this thesis but all the writing has been double checked and read through (multiple times) under human supervision to get rid of the discrepancies.

Table of contents

Chapter 1 INTRODUCTION **1**
1.1 Background and Motivation 1
1.2 Research Statement and Objectives 3
Chapter 2 MACHINE LEARNING INTER-ATOMIC POTENTIALS FOR GRAPHENE **4**
2.1 Introduction 4
2.2 Methodology 6
2.3 Prediction of thermal and mechanical properties 15
2.4 Uncertainty quantification of machine learning potentials 23
2.5 Conclusions 26
Chapter 3 TEMPLATING EFFECTS OF 2D MATERIALS **30**
3.1 Introduction 30
3.2 Methodology 33
3.3 Interfacial crystallography and surface guided crystallisation of polyethylene chains on $MoSe_2$ surface 40
3.4 Edge guided crystallization of polyethylene on $MoSe_2$ surface 53
3.5 Strained 2D substrate to induce anisotropy in nanocomposite 59
3.6 Conclusion 72
Chapter 4 CONCLUSIONS AND FUTURE WORK **74**
References **76**

Chapter 1

INTRODUCTION

1.1 Background and Motivation

The rapid advancement in materials science has led to the discovery and exploration of two dimensional (2D) materials, unveiling a new realm of possibilities for technological advancements. Among these novel materials, graphene has gained substantial attention due to its exceptional mechanical, electrical, thermal and chemical properties. Graphene is a single layer two dimensional material in which carbon atoms organized in a hexagonal lattice. Graphene given its unique material properties has become one of the most researched material till date. This surge of interest in graphene has paved the way in the discovery of other two dimensional materials like Phosphorene, MoS_2, h-BN, $MoSe_2$ etc., each possessing unique attributes that can be utilized for diverse applications. Graphene, among all the two dimensional materials, extraordinarily stands out due to the combination of high electrical conductivity, high mechanical strength, high surface area, and single atomic layer thickness. Over the years graphene has been used for variety of applications, ranging from high specific strength materials such as bullet proof vests, energy storage materials like batteries, sensor materials like gas detectors, flexible electronics like human-like skin in robots etc. to name a few.

Despite the immense potential of 2D materials, their utilization is often hindered by challenges arising from their extremely small thickness and unique characteristics. Experimental characterization and testing of these materials become particularly challenging and costly due to small relevant length and time scales involved. Consequently, the need for innovative methods to systematically evaluate their properties has increased over time. Computational simulations, such as first-principle calculations and classical molecular dynamics (MD) simulations, offer a cost and time efficient method to explore the properties of these materials. While first-principle calculations provide high accuracy in evaluating material properties but they come at a computational cost that limits simulation size and time. On the other hand, classical MD simulations offer computational efficiency, making them suitable for investigating larger and more realistic material models. However, classical MD simulations rely on empirical potentials, whose accuracy is influenced by the fidelity of empirical interatomic potentials. In recent years, the emergence of machine learning techniques has provided a promising solution to bridge the gap between accuracy and efficiency in material simulations by developing accurate interatomic potentials for MD simulations using machine learning methods. By training machine learning models to represent potential energy surfaces derived from first-principle calculations, researchers have unlocked the potential machine learning to combine the accuracy of first-principle calculations with the computational efficiency of classical MD simulations. This has enabled the investigation of material

behaviors at different scales, from the atomic level to the macroscopic properties of nanocomposites. From this stems the first aim of this dissertation i.e. to develop better interatomic potentials for 2D materials like graphene and to be able to use them in MD simulations to achieve an accuracy in evaluating material properties that is comparable to that of first-principle calculations like Density Functional Theory (DFT) simulations. The developed machine learning based interatomic potentials (MLPs) will help simulate 2D materials like graphene with an accuracy of first-principle simulations and evaluate material properties of graphene like coefficient of thermal expansion which are difficult to characterize experimentally due to small thickness and size effects of 2D materials.

Once we have developed better interatomic potentials for 2D materials but stilling putting them to practical applications is far fetched idea due to our limited understanding of behaviour of 2D materials with 3D materials (most 2D materials are used with combining them with 3D materials for practical purposes) as 2D materials can not be used solely due to their single atomic layer thickness that creates handling issues (2D materials are usually fragile in out of plane direction). To, leverage the excellent material properties of these 2D materials we need to use them with polymers to create 2D material based nanocomposites (which are 3D materials) with superior material properties. This allows us to use these 2D materials in a practical applications in our day to day life. In this study we are targeting one specific material system i.e $MoSe_2$ (2D material) and polyethylene (3D polymer) which creates a 2D material nanocomposite. From this stems the second aim of this dissertation, i.e. design and development of nanocomposites based on 2D materials where we will use $MoSe_2$/graphene as our 2D material and polyethylene as our polymer. The focus in these 2D materials based nanocomposites is on harnessing the potential of 2D materials like graphene and $MoSe_2$ to act as nucleating agents for specific crystallization behaviour of polyethylene. Note that polyethylene is a semi-crystalline material where directionally crystallized polyethylene chains can create anisotropic behaviour in crystallized polyethylene which is our focus in this study. Thus, directional assembly of polyethylene chains on the surfaces of these 2D materials offers a unique opportunity to engineer the properties of resulting nanocomposites. But till date we don't have a very clear understanding on how these 2D materials guide the crystallization of polymers such a polyethylene. For this understanding the interfacial interactions, characteristics at 2D material and polymer interface is critical. As we have mentioned before, experimental studies have limitations of capturing the material behaviour at these time and length scales. This steers us to computational simulations which offers a powerful tool in unraveling the behavior of 2D materials based nanocomposites at these small length and time scales. Thus by investigating the crystallization of polyethylene on the surfaces of 2D material $MoSe_2$/graphene through MD simulations, this study seeks to generate new knowledge in the development of 2D materials based nanocomposites. This will open new directions for the design of advanced nanocomposite materials with tailored properties. We also investigated the templating effects of these 2D materials on the crystallization of polyethylene by straining the 2D materials to generate positive reinforcement to crystallize polyethylene chains on 2D material surface in a particular direction. This gives us a tuning knob (percentage strain in 2D material) to guide crystallization of polyethylene chains thereby tunable material properties of the resulting 2D material based nanocomposite by deliberately creating anisotropy in the nanocomposites. This can help in the development of flexible electronics, flexible human like skin for robots etc. where different material properties are needed in different directions.

1.2 Research Statement and Objectives

The research conducted in this dissertation is dedicated to utilize the potential of two dimensional (2D) materials for the development of 2D material based nanocomposites. We have chosen graphene and $MoSe_2$ as our 2D material and polyethylene as our representative polymer in this study. The primary goal is to advance our understanding of the intricate interplay between 2D materials and polymers, ultimately culminating in the design and development of innovative 2D materials based nanocomposites with tunable material properties.

Objective 1: Machine learning for developing interatomic potentials for graphene

The first objective of this research is to use machine learning model to learn the complex interatomic potential function of 2D material i.e graphene in this study. By developing artificial neural network-based machine learning interatomic potentials (MLPs) for graphene (This method is equally applicable to other 2D materials), we aim to fuse the accuracy of first-principle calculations with the computational efficiency of classical molecular dynamics (MD) simulations. In this study, we developed artificial neural network-based machine learning interatomic potentials for graphene that can be used in MD simulations which gives the accuracy comparable to that of first-principle simulation but with a fraction of computational cost compared to it.

Objective 2: Templating effects of 2D material for crystallization of polyethylene

The second objective is to understand the templating effects of 2D material i.e. $MoSe_2$ in this study for crystallizing polyethylene chains and creating deliberate anisotropy in the resulting 2D material based nanocomposite. In this study, we have used MD simulations to investigate the assembly of polyethylene chains on the surface of 2D material $MoSe_2$. The aim of this study is to investigate and understand the crystallization processes of polyethylene chains in the presence of $MoSe_2$ by characterizing the crystallization orientations of polyethylene chains, crystallographic behavior of crystallized polyethylene chains and change in free energy of at the interface. Thus, through a systematic exploration of 2D-polymer interface, we seek to uncover the underlying mechanisms that govern the formation of nanocomposites with tailored material properties.

Objective 3: Comparing templating effects of different 2D materials

The third objective emphasizes a comprehensive characterization of 2D material polymer interface using different 2D materials, i.e. graphene and $MoSe_2$ in this study. In this section, we also aim to discern the impact of strained 2D material substrate on the crystallization orientation of polyethylene chains of $MoSe_2$-polyethylene material system. This investigation will provide a deeper understanding of how these interfacial characteristics influence the macro-level material properties, including mechanical strength, electrical conductivity, and other relevant attributes. The insights gained will contribute to the strategic design of nanocomposites with enhanced functionalities.

Chapter 2

MACHINE LEARNING INTER-ATOMIC POTENTIALS FOR GRAPHENE

2.1 Introduction

The discovery of graphene, a unique 2D material with exceptional mechanical, electrical, and chemical properties [1], [2], has opened a new chapter of 2D materials in materials science. This breakthrough discovery of graphene sparked a rapid exploration of other 2D materials, such as h-BN, phosphorene, MoS2, and MoSe2 [3]–[5]. Graphene's single layer of carbon atoms forming a honeycomb lattice structure creates the foundation for its remarkable material properties. This honeycomb lattice structure of graphene makes it not only one of the lightest materials but also one of the strongest [6] naturally occurring material on earth. The strong covalent bonds (sp2 hybridization) between carbon atoms, in the hexagonal lattice structure of graphene, contribute to graphene's remarkable stability and the ability to form single layer long 2D sheets [1], [2]. These sp2 hybridized covalent bonds also give graphene exceptional high in-plane tensile strength [1], [2]. With three out of four valence electrons participating in covalent bonding of carbon atoms in graphene, the remaining one valence electron provides graphene an outstanding electrical and thermal conductivity [7], [8]. Thus, unique combination of material properties make graphene a prime candidate for the development of next-generation composite materials. The potential applications of graphene spans a wide range, including bulletproof vests, mechanical resonators, high energy storage batteries, and gas detectors [7] etc. Given these extraordinary material properties of graphene, it can be considered as a metamaterial with the potential to revolutionize diverse fields in the future to come, like composites, batteries, and superconductors [7].

Over the last decade, there has been extensive experimental research on graphene and graphene-based nanocomposites to unravel their unique material properties and establish their structure-property relationships. Lee et al. [9] investigated the Young's modulus of graphene, determining it to be 1 ± 0.1 TPa, thus confirming graphene as the strongest material measured to date. Another investigation by Lee U. et al. [10] utilized Raman spectroscopy to estimate the Young's modulus of single-layer graphene and found it to be 2.4 TPa. Bao et al. [11] experimentally determined the coefficient of thermal expansion of graphene, noting its transition from negative to positive values between room temperature and 375 K, with a monotonic increase from 300 K

to 400 K. Similarly, Yoon et al. [12] utilized Raman spectroscopy to predict a monotonically increasing, yet negative, coefficient of thermal expansion across the temperature range of 200 K to 400 K. Yang et al. [13] compiled experimental data on in-plane lattice parameter of graphene, suggesting a constant value of 2.46 Å in the temperature range of 200 K to 1000 K. Manigandan et al. [14] explored the topological properties of graphene-based nanocomposites doped in Kevlar, finding an increase in nanocomposite strength with higher graphene percentages, ranging from 0% to 5%. These discrepancies in experimental data in evaluating Young's modulus and coefficient of thermal expansion of graphene may stem from the challenges associated with characterizing and testing the extremely thin dimensions of 2D materials experimentally, making it imperative to explore alternative methods for systematically evaluating graphene's material properties.

Analytical and computational simulations offers a cost and time-efficient alternative to experimental studies for investigating the behaviour of 2D materials. First-principle calculations and classical molecular dynamics (MD) simulations are commonly used for such investigations [15], [16] where experimental scientists find it difficult to characterize a material. First-principle calculations, utilizing Density Functional Theory (DFT) simulations and ab initio MD simulations, explore the electronic structure of many-body systems to assess material properties of 2D materials like graphene. Tianjiao et al. [15] conducted first-principle calculations using quasi-harmonic approximations (QHA) to evaluate the Young's modulus of graphene across a temperature range of 20 K to 1000 K, yielding a constant value of 1.15 TPa. Mounet et al. [16] utilized DFT simulations to determine the lattice parameter of graphene, observing a slight decrease in lattice parameter with temperature within the temperature range of 20 K to 1000 K. Their study also analyzed the coefficient of thermal expansion (CTE) of graphene with respect to temperature, noting a negative, non-monotonic trend decreasing from 20 K to 250 K, followed by an increase in lattice parameter from 250 K to 2000 K. Classical MD simulations are also prevalent for establishing, evaluating, and analyzing material properties due to their computational efficiency [17]–[19]. These MD simulations rely on simplified empirical potentials, often derived from parameter fitting based on experimental or first-principle calculation results. Consequently, the success of classical MD simulations heavily depends on the fidelity and availability of empirical potentials. Rahman et al. [20] investigated the mechanical performance and fracture behavior of silicon-doped graphene using classical MD simulations. In another study employing classical MD simulations, Li et al. [19] explored the effect of functionalized interfaces between graphene and polyethylene, revealing varied Young's modulus with differing numbers of different functional groups. These investigations, including that of Rahman et.al. and Li et.al. [19], [20], demonstrate the feasibility of characterizing the mechanical properties of graphene and graphene-based nanocomposites through classical MD simulations, overcoming experimental challenges. Also, their study suggest the capability of classical MD simulations to simulate larger, more realistic material models with reasonable accuracy, a task currently challenging for DFT and ab-initio MD simulations. First-principle calculations delve into the electronic structure of atoms, yielding highly precise results for evaluating material property and their behaviour. However, this precision comes with a computational burden that constrains the size and duration of first-principle simulations for the targeted material system. Consequently, we encounter a stalemate where one simulation type is computationally fast but less reliable (classical MD), while the other emphasizes on accuracy (DFT) but is computationally expensive. Recently, a few studies have explored the possibility of representing the potential energy surface of materials using machine learning techniques, derived from DFT simulations **SINGH2023112272 Wen˙et˙al**, [21]. In this methodology, a machine learning model is trained to depict the potential energy surface for a specific material system, offering scalability and adaptability. Subsequently, this trained machine learning model can be integrated into classical MD simulations to analyze material behaviors and assess material properties with an accuracy comparable to that

of first-principle simulations. Such machine learning-driven interatomic potential (MLP) enables the accuracy of DFT simulations with the computational efficiency of classical MD simulations [21], [22] helping us get the better of both the computational simulation types. In this research, we have developed an artificial neural network-based machine learning interatomic potential (MLP) specifically tailored for graphene. The training dataset was constructed using first-principle calculations of graphene, as outlined in the study by Rowe et al. [22]. Atomic configurations within the training dataset were encoded using a symmetry function-based atom-centered coordinate system. The trained artificial neural network (ANN) with optimized weights and biases effectively represents graphene's interatomic potentials under diverse loading and experimental scenarios which was extensively validated before being put to use in MD simulations. Classical molecular dynamics (MD) simulations were conducted using LAMMPS [23], an open-source MD simulation software, combined with n2p2 software [24] to incorporate machine learning interatomic potentials. In this study, we evaluated lattice parameter, coefficient of thermal expansion, Young's modulus, and ultimate tensile strength of graphene to validate the accuracy and predicting power of ANN-based MLP. Finally, a comparative analysis of these material properties of graphene with experimental findings and DFT simulations suggests the efficacy and practical applicability of machine learning interatomic potentials in the context of graphene research.

2.2 Methodology

In this section, artificial neural network (ANN)-based machine learning model was used to develop interatomic potentials that characterize the potential energy surface of graphene. To enable effective training of ANN, atomic configurations were translated into a global representation using symmetry functions [25]. These symmetry functions offered an invariant representation of atomic coordinates for the material system i.e new coordinate system is universal in nature and does not depend on a reference frame. During the iterative training process, the ANN's weights and biases were optimized through backpropagation, aiming to minimize the discrepancy between predicted energy values and reference energy values. The training iterations were stopped for a specific ANN once a desired level of accuracy was attained for the network's weights and biases. The resulting ensemble of optimized weights and biases within a trained ANN encapsulates a sophisticated interatomic potential function, which defines the intricate connection between atomic structure and energy for the desired material system i.e graphene in this study. This ensemble, termed as machine learning interatomic potential (MLP) for graphene, serves as a model capable of estimating energy values based on atomic configurations. The subsequent content of this section is divided into two distinct subsections. First subsection delves into the details of the symmetry functions used to encode the spatial coordinates of atoms for graphene, while the second subsection focuses on the training methodology applied to the ANN to training the MLP.

Symmetry Functions

Before initiating the training process for an artificial neural network (ANN), it's imperative to represent each atomic structure in the training dataset in a way that's invariant to translation, rotation, and the exchange of equivalent atoms. In this research, this invariance was achieved by encoding atomic structures using symmetry functions [25], [26]. This approach ensured that each reference atomic structure was consistently represented, obviating the need for a specific coordinate system. Since, the basis functions were centered on individual atoms, the evaluation of energy after the training of machine learning interatomic potentials remained independent of the choice of coordinate system. This eliminated the need of multiple coordinate

transformations across datasets with various coordinate systems. Two different type of symmetry functions were adopted for characterizing the atomic structures in this study: radial symmetry functions and angular symmetry functions. Radial symmetry functions, detailed in Equations 1 and 2, accounts for two-body interactions surrounding the central atom. On the other hand, angular symmetry functions, described in Equation 3, consider the three-body interactions centered around the central atom. The combination of radial and angular symmetry functions creates a comprehensive depiction of the atomic environment within a material system comprising a single atomic species i.e graphene in this study.

A radial symmetry function can be defines as follows:

$$G_r^i(\sigma) = \sum_{j \neq i}^{nr} g_r^i(R_{ij}) = \sum_{j \neq i}^{nr} \exp^{-\eta(R_{ij}-R_s)^2} f_c(R_{ij}) \tag{2.1}$$

Here, σ represents three-dimensional atomic coordinates, $R_{ij} = |R_i - R_j|$ signifies the distance between the central atom i and its neighboring atom j, R_c is the cutoff radius, η is the radial parameter, nr denotes the number of neighboring atoms around atom i within the specified cutoff distance, and f_c is the cutoff function.

An angular symmetry function can be expressed as follows:

$$G_a^i(\theta) = \sum_{j \neq i, k \neq i, j \neq k}^{na} g_a^i(\theta_{ijk}) \quad = 2^{1-\zeta} \sum_{j \neq i} \sum_{k \neq i, j \neq k} (1 + \lambda \cos(\theta_{ijk}))^{\zeta} \exp^{-\eta(R_{ij}^2 + R_{ik}^2 + R_{kj}^2)} f_c \tag{2.2}$$

In this equation, θ_{ijk} denotes the angle between the central atom i and its neighboring atoms j and k. Parameters ζ, λ, and η are used to define the angular symmetry function. na represents the number of atoms around atom i within the designated cutoff distance, and, f_c is the cutoff function. A composite vector denoted as $G_i = [G_{r1}, G_{r2}, ..., G_{r10}, G_{a1}, G_{a2}, ..., G_{a20}]$ was constructed based on a collection of all the radial and angular symmetry functions. This vector was used to encode the atomic surroundings for each atom contained within the reference dataset. Consequently, the total energy of an individual atomic structure was represented as the sum of energies contributed by each atom. This summation could be further expressed in terms of radial and angular symmetry functions, as outlined in Equation 4. The formulation for the total energy of a single structure can be expressed as follows:

$$E_{\text{tot}} = \sum_{i=1}^{n} E_i \approx \sum_{i=1}^{n} E_i^{\text{ANN}}(G_r(R), G_a(R, \theta)) \tag{2.3}$$

In this equation, E_{tot} signifies the total energy of the reference dataset, E_i represents the energy of the individual atom indexed as i, n corresponds to the total count of atoms present in the structure, and $E_i^{\text{ANN}}(G_r(R), G_a(R, \theta))$ denotes the energy attributed to atom i through the artificial neural network potential, that is determined by the radial and angular symmetry functions. As a result, for each distinct structure, the input provided to the artificial neural network is a matrix of dimensions n by m, where n denotes the number of atoms within the structure, and m signifies the total count of symmetry functions associated with each atom. Here is the tabular information for the parameters related to the radial symmetry functions (G_r type) with $R_c = 6.5$ Å and $R_s = 0$:

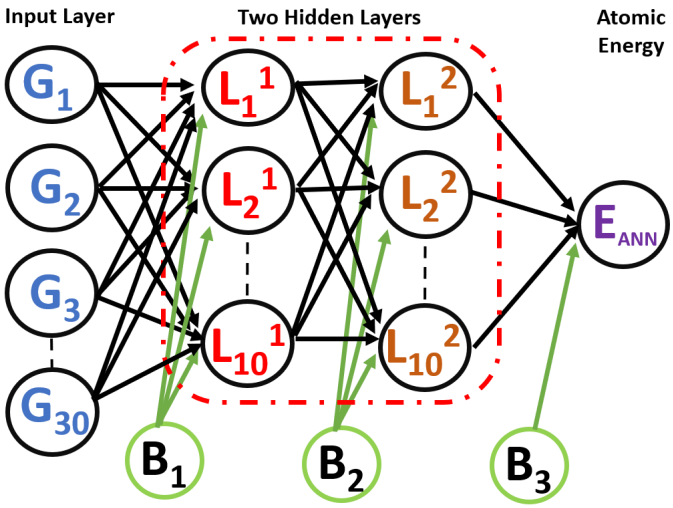

Figure 2.1: Diagram of atomic artificial neural network deployed in this study. Input to the atomic ANN are the symmetry function values. This atomic ANN has two hidden layers with 10 neurons each. Output from the atomic ANN is atomic energy of the given atom. Reprinted (adapted) with permission from Singh et.al. https://doi.org/10.1016/j.commatsci.2023.112272. Copyright 2023 Elsevier

Table 2.1: Parameters for G_r type of radial symmetry functions (R_c = 6.5 Å and R_s = 0)

S.No	η	S.No	η
1	0.004938	6	0.493827
2	0.012404	7	1.240438
3	0.031158	8	3.115839
4	0.078266	9	7.826633
5	0.196596	10	19.659613

Table 2.2: Parameters for G_a type of angular symmetry functions (R_c = 6.5 Å and R_s = 0)

S.No	η	ζ	λ	S.No	η	ζ	λ
1	0.000049	2	1	11	0.000049	2	-1
2	0.000124	4	1	12	0.000124	4	-1
3	0.000312	6	1	13	0.000312	6	-1
4	0.000783	8	1	14	0.000783	8	-1
5	0.001966	10	1	15	0.001966	10	-1
6	0.004938	12	1	16	0.004938	12	-1
7	0.012404	14	1	17	0.012404	14	-1
8	0.031158	16	1	18	0.031158	16	-1
9	0.078266	18	1	19	0.078266	18	-1
10	0.196596	20	1	20	0.196596	20	-1

Artificial Neural Network

The feedforward artificial neural network [27] is one of the earliest machine learning neural networks developed. In this particular type of neural network functions the information flows in a single direction without any cyclic processes, as depicted in Figure 2.1. The configuration of an artificial neural network is characterized by three fundamental parameters: the quantity of hidden layers, the activation functions used, and the number of nodes situated within hidden layers.

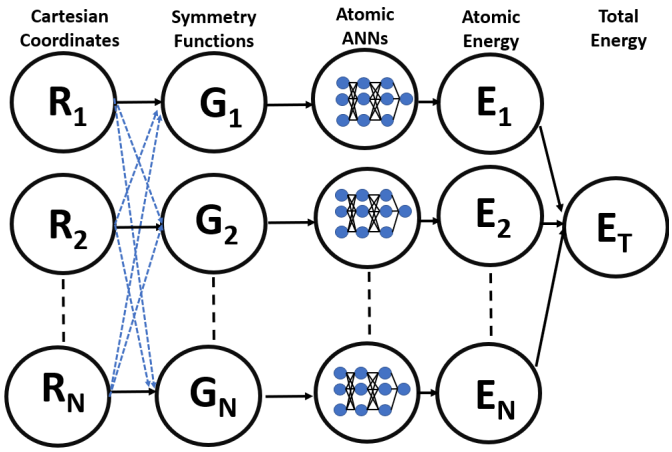

Figure 2.2: Schematic of artificial neural network (ANN) potential for graphene. Each atom is represented by a line with cartesian coordinates R_i. First step converts cartesian coordinates into symmetry function values G_i using the cartesian coordinate information of all the other atoms with the cutoff radius i.e in the local environment of that atom, shown by blue dotted arrows. Then, the symmetry function values are fed to the ANN providing energy contribution from each atom E_i. Finally the total structural energy is evaluated as the sum of all E_i. Reprinted (adapted) with permission from Singh et.al. https://doi.org/10.1016/j.commatsci.2023.112272. Copyright 2023 Elsevier

For training the artificial neural network, an energy-based loss function was used. This loss function is used to minimize the discrepancy between the predicted energy outcomes derived from the artificial neural network and the reference energy values extracted from a dataset established through Density Functional Theory (DFT) simulations. In this study, root mean squared error (RMSE) function was evaluated as the loss function between ANN and DFT results, as shown in Equation 5.

$$\epsilon(w_m, b_m) = \frac{1}{2}\sum_{s=1}^{c}[E_s^{\mathrm{ANN}}(\sigma, w, b) - E_s^{\mathrm{ref}}]^2 \quad = \frac{1}{2}\sum_{s=1}^{c}\left[\sum_{i=1}^{n} E_{s,i}^{\mathrm{ANN}}((G_r^i, G_a^i), w, b) - E_s^{\mathrm{ref}}\right]^2 \tag{2.4}$$

Here, c is the total number of configurations in the dataset, ref is utilized to signify the reference dataset. The term E_s^{ANN} denotes the energy evaluated using artificial neural network, while E_s^{ref} is the reference energy computed using DFT calculations. Given that the neural network predicts the energy values on an atomic scale, whereas DFT calculations do not directly provide atomic energies, therefore all the atomic artificial neural networks are concurrently trained across all atoms present in each dataset (evaluating total energy of each dataset). The cumulative energies predicted by the individual atomic neural networks are then summed to yield the total energy, as shown in Figure 2.2. During the training process of atomic artificial neural networks (ANNs), the gradient of the loss function which is used to evaluate the weight parameters, was computed using the backpropagation technique. This enabled iterative adjustments to the weights. Two distinct training methods, namely Gradient Descent (GD) and Levenberg-Marquardt (LM), were used to fine-tune the ANN weights. The weight parameters were updated within each training epoch using the following formulations:

For Gradient Descent:

$$w^{i+1} = w^i + \Delta w^i \tag{2.5}$$

$$\Delta w^i = -h\nabla\epsilon \tag{2.6}$$

For Levenberg-Marquardt:

$$\Delta w^i = -(J^{T,i-1}J^{i-1} + \lambda I)^{-1}\nabla\epsilon \tag{2.7}$$

The expression for the gradient of the loss function ($\nabla\epsilon$) is given by Equation 8, where ϵ represents the loss function, E_s^{ANN} denotes the ANN-predicted energy, E_s^{ref} signifies the reference energy, n is the total number of atoms, and $\frac{\delta[E_{S,i}^{\text{ANN}}(G_r^i, G_a^i, w, b)]}{\delta w_m}$ symbolizes the derivative of the ANN-predicted energy with respect to the weight parameter w_m.

For our material system i.e. graphene the Levenberg-Marquardt backpropagation method converges quickly compared to Gradient Descent method due to its second-order correction. However, since the size of the Hessian matrix that needs to be inverted increases rapidly if the dimensions of artificial neural network becomes large that usually make Levenberg-Marquardt more inefficient. Under such circumstances, alternative training algorithms like BFGS should be considered. Fortunately, the complexity of our training dataset did not necessitate such an approach and Levenberg-Marquardt worked flawlessly for us.

2.2.1 Training and Validation of Machine Learning Potentials for Graphene

This section outlines the creation of training data, necessary coordinate transformation involved, training methods, and validation steps used for the development of machine learning interatomic potential for graphene. First subsection outlines the process of generating the training dataset, second subsection delves into the depiction of graphene's atomic environment, third subsection explores the two training methods used for the machine learning potentials (MLP) and their effectiveness, while fourth subsection outlines the validation steps taken to assess the performance of the MLP.

Training Dataset

The efficacy of the developed machine learning potential relies heavily on the quality and representation of structures within the training dataset. Our training dataset was constructed by using finely-tuned Density Functional Theory (DFT) simulations on reference configurations derived while taking snapshots of cartesian coordinates while straining the graphene sheet along armchair and zig-zag directions at regular intervals. This dataset is called the reference dataset in this study where all the reference graphene structures (atomic coordinates) of each carbon atom consisted of a single layer with 24 carbon atoms in each structure. For straining the graphene and creating the reference dataset, Molecular Dynamics simulations were conducted to induce stretching in graphene sheets, generating different atomic configuration structures. Note only atomic coordinates were captured using MD simulations for each structure but not the atomic energies. For each atomic configuration captured, i.e atomic coordinates/cartesian coordinates for a configuration, the reference energy was evaluated using DFT simulations. A total of 320 reference configurations (each with a different coordinates of all 24 carbon atoms depending on the level of applied strain) were created, obtained by systematically extracting snapshots from stretched trajectories of graphene i.e. 160 configurations snapshots were obtained by stretching graphene along the armchair direction, while the remaining 160 snapshots were captured from stretching graphene along the zigzag direction. DFT simulations for each reference configuration were conducted which evaluated the total potential energy of each reference structure in the dataset. This was accomplished utilizing the Perdew-Burke-Ernzerhof (PBE) exchange-correlation functional, implemented through the PWSCF module of the Quantum ESPRESSO package [28]. The wave functions were represented using in-plane wave basis sets with energy cutoffs set at 40 Ry and 120 Ry, respectively. GBRV ultrasoft pseudopotentials were used for the core regions of atoms. For the integration of the Brillouin

zone, a gamma-centered k-point mesh (4-16-1 k-points) was used for the crystal cell containing 24 carbon atoms.

Symmetry Functions and Description of Graphene's Atomic Environment

Graphene, being composed solely of carbon atoms, represents a relatively simple material system. The choice of symmetry function parameters plays a pivotal role in enhancing the stability and accuracy of the developed MLP. To achieve this, a strategy proposed by Artrith et.al. [29] for selecting symmetry function descriptors was adopted in this study. This strategy involves employing combined descriptors to effectively represent the local atomic structure and composition. Artrith's findings suggest that the mathematical completeness of descriptors isn't necessary for nonlinear machine learning models, as long as they can adequately distinguish between pertinent samples. Consequently, the potential energy surface can be depicted using a compact basis set, corresponding to a coarse depiction of radial and angular symmetry functions.

Radial symmetry functions, as represented in Equation 2.1, incorporated a Gaussian function suffixed with a cutoff function. The cutoff function f_c serves to encode energetically significant regions proximal to the central atom within atom-centered symmetry functions. Parameters η and R_s regulate the width and positioning of the Gaussian function, respectively. For angular symmetry functions, as per Equation 2.2, the term within the brackets characterizes the angular distribution. Parameter λ shifts the angular term's peak value between 0° and 180°, while parameter ζ controls the Gaussian function's angular width. The introduction of terms involving r_{ij} introduces asymmetry into angular functions. This leads to the selection of four parameters $(\eta, R_s, \lambda, \zeta)$ for constructing appropriate sets of atom-centered symmetry functions.

Choosing λ and ζ for angular symmetry functions is relatively straightforward. Typically, utilizing two sets of angular symmetry functions with $\lambda = 1$ and $\lambda =$ -1 is the general approach, as it covers the full range of angles present in the local environment. Parameter ζ governs angular resolution, where lower values of ζ yielding higher resolution. In our case, values of ζ ranging from 2 to 24 in increments of 2 units were used. R_s parameter horizontally displaces the Gaussian function. In our study, R_s was set to 0 for the symmetery functions either radial or angular. Among all the parameters, η exerts the most significant impact on descriptor the performance for both radial and angular symmetry functions. Typically, the value of η for the radial symmetry function with the smallest effective range (corresponding to the shortest interatomic distances in the dataset) is determined by spatial extension. The choice of lowest η for radial symmetry functions is guided by the correlation between symmetry function values (with at least 90% linear independence) for all atoms present in the reference training dataset. To ensure even spatial coverage from r_o to r_c, an auxiliary radial grid is introduced. This auxiliary grid comprises N equidistant points spanning from r_o to r_c. Consequently, the values of η are defined as $\eta_i = 1/2r_i^2$ while adhering to the aforementioned constraints. In our study, a total of 10 radial and 20 angular symmetry functions were used to characterize the local atomic environment in the simulation system. This results in a 30-dimensional transformed coordinates that serves as an input vector for the training of atomic ANN. All the parameter selections used in the calculations of radial and angular symmetry functions can be found in Table 2.1 and Table 2.2.

Training of Machine Learning Potential (MLP)

This study employs a high-dimensional atom-based artificial neural network, depicted in Figure 2.2, comprising N atoms, with each line signifying a graphene atom. The initial step involves converting the Cartesian coordinates $R_i = (X_i, Y_i, Z_i)$ into symmetry functions G_i, which serve as suitable inputs for the atomic ANNs. These atomic ANNs predict the energy associated with each atom, the sum of which yields the total energy of

the structure. The feedforward ANN architecture utilized in this research encompasses 2 hidden layers, each comprising 10 nodes. The hyperbolic tangent function serves as the activation function within the hidden layers, which helps in the MLP training creating smoothly terminating functions. The reference dataset was divided in a manner where we allocated 90% of reference dataset for training the MLP and the remaining 10% for testing the MLP. The training progress was monitored through the evolution of the root mean squared error (RMSE) of the reference structures, depicted in Equation 2.8.

$$RMSE = \sqrt{\frac{1}{n}\sum_{i=1}^{nt}(E_i - E_i^{ANN})^2} \tag{2.8}$$

Two distinct training methods, Gradient Descent (GD) and Levenberg-Marquardt (LM), were implemented and compared in this study. The GD method is known for its computational efficiency in comparison to the LM method. Thus, to compare the performance of these two methods, error histories of the predicted energy against reference DFT values were plotted during the training process, as displayed in Figure 2.3. Notably, both methods can achieve well-converged ANN structures within a reasonable number of iterations. However, it is evident that LM method can attain an accuracy of 5 meV/atom in less than 50 iterations for our reference training dataset, while the GD method converges to a lower accuracy, exhibiting an RMSE error of 115 meV/atom even after 400 iterations. Although the number of training iterations doesn't directly correlate with computing time, considering the dimensions of the current ANN and the relatively small training dataset used in this study, the LM method proves to be more efficient. As a result in this study, the weights and biases corresponding to the LM training method were used to develop the MLP in its current form.

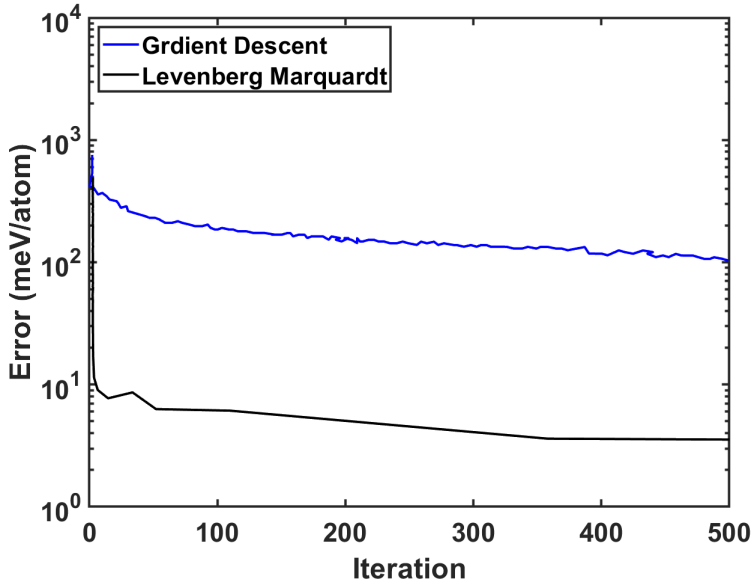

Figure 2.3: Training error of MLP with error history using Gradient Descent method and Levenberg-Marquardt method is shown. It can be noted that LM method converges quickly for our training dataset

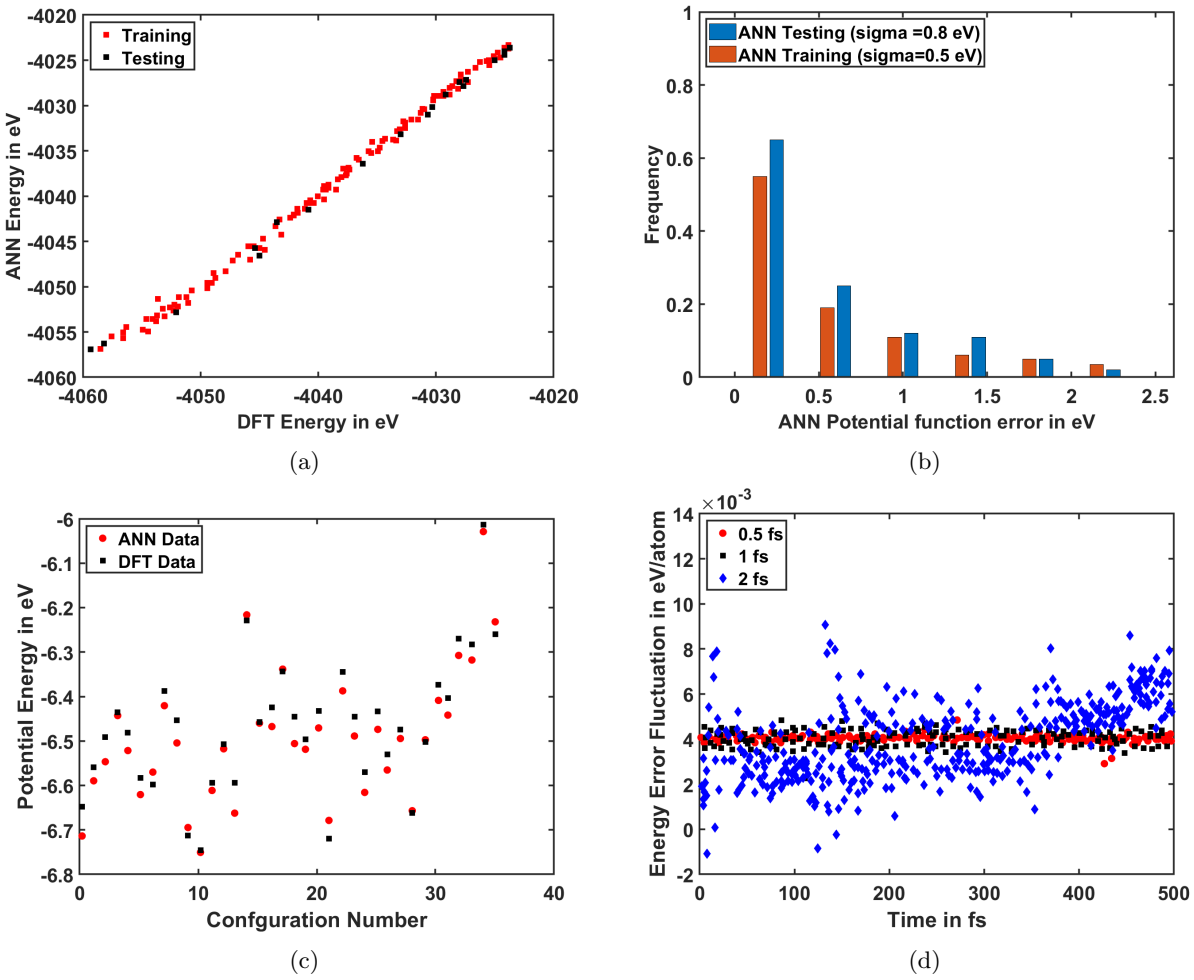

Figure 2.4: Figure: (a) Correlation of ANN energies with training and testing dataset with DFT energies (b) Histogram of energy error distribution for training and testing datasets (c) Potential energy fluctuations for different configurations for ANN and DFT simulations (d) Effect of different time steps on potential energy evaluated from ANN potentials

Validation of the Machine Learning Potential

Validating the accuracy and reliability of the developed machine learning potential (MLP) is a crucial step in ensuring its effectiveness. The correlation between predicted MLP energies and the corresponding reference energies obtained through density functional theory (DFT) is a fundamental aspect of validation. As depicted in Figure 2.4a, this correlation demonstrates a strong agreement between the predicted and reference energies for both the training and testing datasets. The fitting function y = x indicates that the predicted energies closely match the reference energies across a variety of atomic configurations, attesting to the MLP's accuracy in capturing the potential energy landscape. The distribution of energy errors is another insightful measure of MLP performance. Illustrated in Figure 2.4b, the energy error histogram for both the testing and training datasets showcases the error distribution in electron-volts. Approximately 75% of the training errors and 70% of the testing errors are below the designated target accuracy, indicating the MLP's capability to achieve accurate energy predictions. To further assess MLP reliability, monitoring the potential energy fluctuations within different molecular dynamics (MD) simulation trajectories is also critical. Figure 2.4c presents the

MLP-predicted energies with the corresponding DFT energies for 36 reference structures. The results reveal the MLP's robust performance in estimating the energy of metastable atomic configurations, with deviations of less than 3 meV/atom. MLP's ability to yield a smooth and continuous potential energy surface is equally important as it facilitates easy numerical integration of equations of motion during MD simulations with unseen atomic configurations. Demonstrated in Figure 2.4d, the total energy profiles of a single-layer graphene sheet over 500 fs using time steps of 0.5 fs, 1 fs, and 2 fs within the NVE ensemble at room temperature are compared. The plots indicate that the total energy of the material system remains well conserved, with fluctuations confined to a few meV for MD simulations using step sizes of 0.5 fs and 1 fs. However, a slight drift is observed for the 2 fs step size case, warranting further investigation. Another crucial metric for assessing the efficacy of the MLP lies in its capacity to accurately predict atomic forces. Since our MLP was exclusively trained on DFT-derived potential energies, evaluating its performance in force prediction is very important. To this end, a selection of 300 random samples from MD simulations was utilized to compare the forces predicted by the MLP with those from DFT simulations. The results, depicted in Figure 2.5, reveal some scattering in predicted force values, yet it suggests a robust correlation between the forces predicted by the MLP and those obtained through DFT simulations. Notably, the predicted forces largely remain within 1.5 eV/Å of the standard deviation. Furthermore, the alignment of the majority of force vectors predicted by the MLP was also investigated, as demonstrated in Figure 2.6. It can be observed that the direction of these force vectors exhibits a strong correlation with the DFT simulation results, with deviations within 20 degrees. This suggests the MLP's ability not only to predict magnitude of forces accurately but also to approximate their directional components effectively.

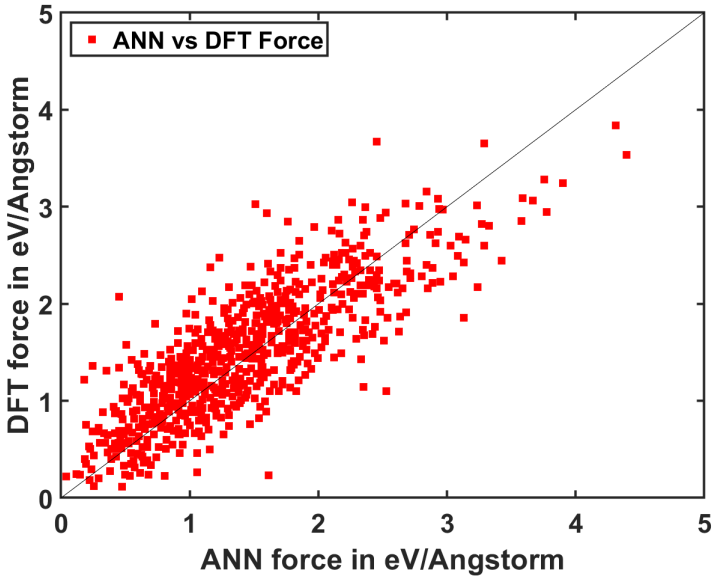

Figure 2.5: Correlation of magnitude of atomic forces in graphene predicted by ANN and corresponding DFT simulations

In atomistic simulations, accurately calibrated phonon dispersion is a fundamental prerequisite for interatomic potentials to yield a precise representation of lattice dynamics. Phonon dispersion, a property that can be experimentally measured, also serves as an excellent independent metric for validating the overall quality of an interatomic potential. Hence, the validation of phonon dispersion was also done for MLP

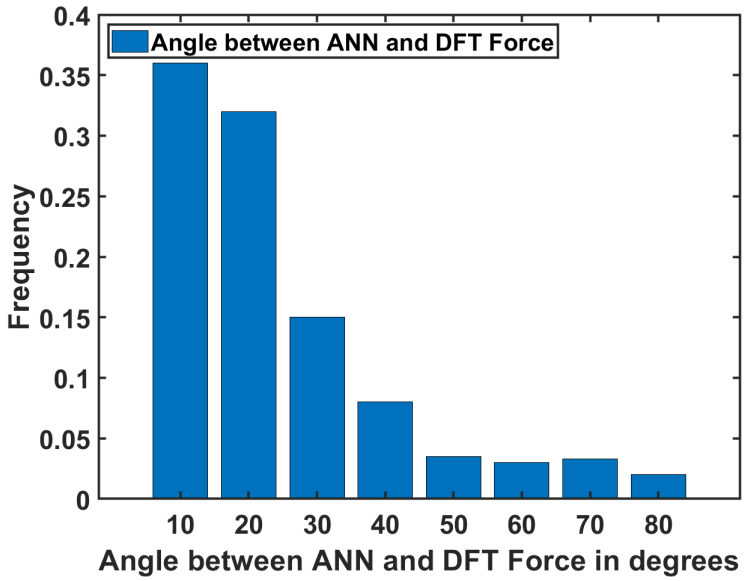

Figure 2.6: Histogram plot showing similarity in angle predicted by ANN and corresponding DFT forces

developed in this study using the small displacement method.

Figure 2.7 illustrates the phonon map of graphene as predicted by the MLP, employing different reference datasets. The green lines depict the outcomes of atomistic simulations, while the red lines correspond to the findings of experimental studies. In Figure 2.7 (a), an MLP trained with 124 samples in training dataset accurately captures the general shape and trend of most phonon branches but exhibits an underestimation of absolute values. Subsequently, in Figure 2.7 (b), an enhancement in predicted phonon energies can be observed upon increasing the sample size of training dataset to 300. This enhancement is particularly pronounced for the low-energy branches, where predictions display strong correlation, while overestimations persist for higher energy branches. Interestingly, additional refining of representation strategy for atomic configurations in the reference dataset was done by expanding the cutoff distance from 4.5 Å to 6.5 Å which leads to improved phonon dispersion predictions, as demonstrated in Figure 2.7 (c). This implies that the quality of the MLP can be systematically enhanced by adjusting various parameters, such as the size of the training dataset and the degree of the digitization process. However, a comprehensive understanding of the complete set of factors governing an optimal tuning strategy for the MLP necessitates further systematic uncertainty quantification. Through comprehensive validation procedures shown above, the developed MLP exhibits strong predictive accuracy, reliability in capturing metastable structures, and the capability to sustain smooth energy profiles using MD simulations. These findings collectively highlight the effectiveness of the developed machine learning interatomic potential for graphene in this study.

2.3 Prediction of thermal and mechanical properties

This section presents temperature dependence of mechanical and thermal properties of graphene by conducting Machine Learning interatomic Potentials based Molecular Dynamics (MLMD) simulations. Section 2.3.1 discusses the evaluation of thermal properties of graphene i.e. coefficient of thermal expansion and lattice parameter between 125 K - 1000 K temperature range. Section 2.3.2 discusses the mechanical performance of

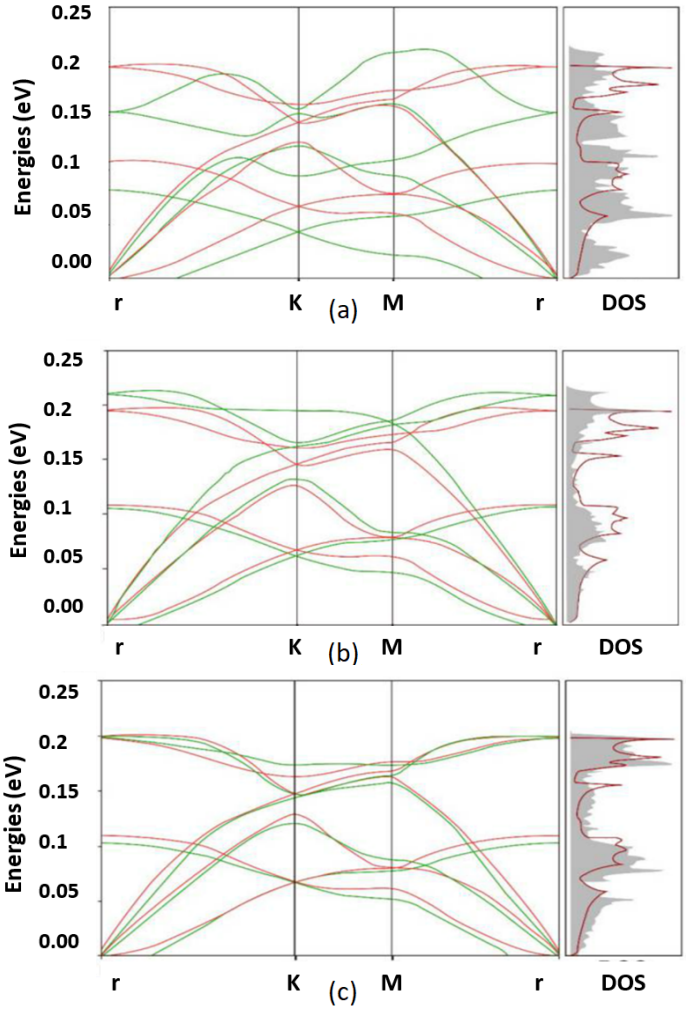

Figure 2.7: Comparison of predicted phonon dispersion using MLP (small displacement method) with experimental results (a) using 124 samples with a cutoff distance 4.5 Å (b) using 300 samples with a cutoff distance 4.5 Å (c) using 300 samples with increased cutoff distance of 6.5 Å

graphene i.e. Young's modulus and ultimate tensile strength between 125 K - 2000 K temperature range. These estimated mechanical and thermal properties of graphene are also compared with first principle calculation and experimental results from previous literatures in this section.

2.3.1 Lattice parameter and coefficient of thermal expansion

Lattice parameter stands out as a critical property of a material system that can be evaluated for an atomistic model of graphene. It influences various intrinsic material properties of graphene, such as Young's modulus, yield strength, coefficient of thermal expansion etc. In nanocomposites, the nature and extent of interaction between graphene and polymers can significantly alter material properties, contingent upon the degree of lattice matching between the two materials [30]. Our investigation compares lattice parameters predicted by MLMD simulations with those from computational and experimental studies documented in the literature [15], [16], [31]–[33], as shown in Figures 2.8a and 2.8c. We evaluated the in-plane lattice parameter for a freestanding graphene sheet containing 12400 atoms over a temperature range of 125 K to 1000 K. MLMD simulations were conducted using NPT ensemble using Nosé-Hoover thermostat, maintaining isobaric-isothermal conditions with pressure set at 1 bar. Simulations at 300 K were equilibrated for 10 ns, and three realizations were used for each temperature. Lattice parameters were computed and averaged over a 20 ns duration for each simulation. Figure 2.8a illustrates that DFT simulations by Mounet et al. [16] predicting a marginally decreasing lattice parameter, measuring 2.469 Å at 125 K and 2.463 Å at 1000 K. In another study by Tianjiao et al. [15], DFT simulations employing quasi-harmonic approximation (QHA) suggested a constant lattice parameter around 2.454 Å over the temperature span of 125 K to 1000 K. Monte Carlo simulations by Zakharchenko et al. [34] and classical MD simulations using the empirical potential LCBOP [31] suggest a similar prediction of the lattice parameter, remaining constant at 2.457 Å over the temperature range of 125 K to 1000 K. Classical MD simulation using AIREBO [32] potential predicts a much smaller lattice parameter of 2.418 Å compared to the predictions in other works. Our MLMD simulation forecasts a comparable lattice parameter with DFT simulations, approximately around 2.456 Å, within the explored temperature range. Figure 2.8c presents the normalized lattice parameter (lattice parameter normalized with the value of the lattice parameter at 20 K), demonstrating the temperature-dependent lattice parameter's variations. DFT simulations by Mounet et al. depict a monotonically decreasing lattice parameter, while DFT-QHA simulations by Tianjiao et al. show a non-monotonic and slightly increasing lattice parameter in the temperature range of 125 K to 1000 K. Classical MD simulations based on AIREBO potential display a similar non-monotonic trend as the DFT-QHA simulation results, while MD simulations using the LCBOP potential reveal a monotonic decreasing lattice parameter. Our MLMD simulation results follow a similar trend as the DFT simulation by Mounet et al. [16], indicating a monotonically decreasing lattice parameter between 20 K and 1000 K.

Coefficient of thermal expansion (CTE) serves as a crucial thermal property of graphene, offering insights into the anharmonicity of bonding interactions between atoms, relative strengths of in-plane and out-of-plane forces within the material system, and the vibrational coupling between harmonic and anharmonic modes. Equation 2.9 outlines the mathematical formulation utilized in this investigation for computing the coefficient of thermal expansion for graphene.

$$CTE = \frac{1}{A_t}\frac{\partial A_t}{\partial T} \tag{2.9}$$

where A_t represents the area of the graphene sheet at temperature T in Kelvin. To evaluate the derivative

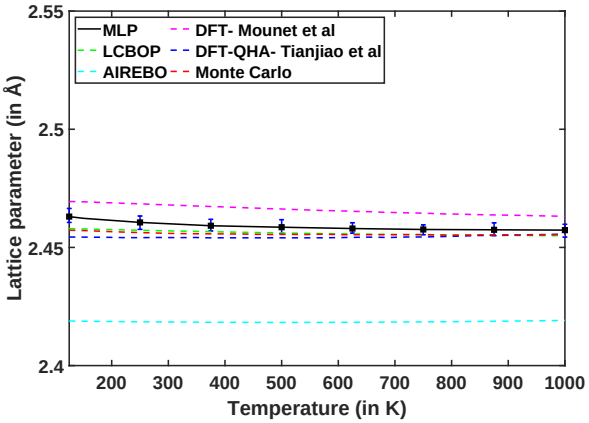

(a)

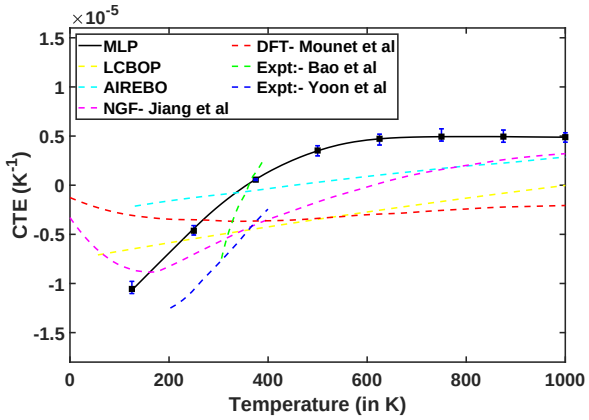

(b)

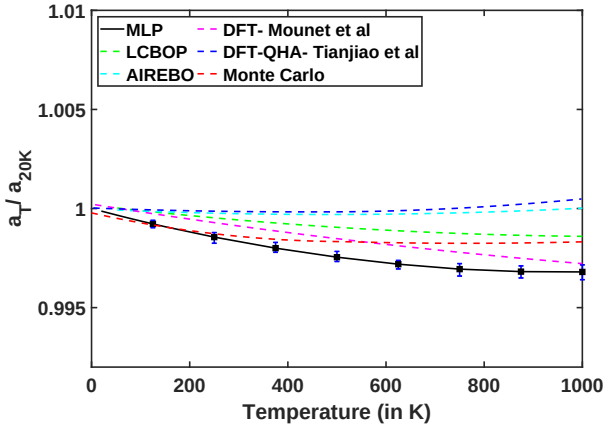

(c)

Figure 2.8: (a) Comparison of temperature dependence of lattice parameter for different interatomic potentials from literature and machine learning potentials (MLP) developed in this study (b) Comparison of MLP evaluated coefficient of thermal expansion for graphene as a function of temperature between 125 K to 1000 K with different interatomic potentials from literature (c) Thermal dependence of normalised lattice parameter with lattice parameter value at 20 K - a varied range of predictions were observed i.e. monotonically increasing, decreasing to more complex non monotonic behaviour. Third order polynomial fitting was used to evaluate the lattice parameter value at 20 K

of the area with respect to temperature, spline interpolation was used between the evaluated areas at each temperature. In-plane CTE was determined using MLMD simulations on freestanding graphene sheets containing 12400 atoms across a temperature range of 125 K to 1000 K. CTE was assessed at discrete temperatures within this range. MD simulations were conducted under NPT ensemble using (Nosé-Hoover thermostat) isobaric-isothermal conditions, with pressure set at 1 bar and temperature at 300 K. Simulations were equilibrated for 10 ns at 300 K, followed by a temperature increase to reach the desired temperature with a ramping rate of 25 K/ns. Three similar simulations were conducted for CTE at a particular temperature, and the final CTE was averaged for each temperature. The behavior of CTE concerning temperature for graphene remains a contentious topic, with conflicting findings from previous literature studies. Experimental research by Bao et al. [11] suggests a transition of CTE from negative to positive (approximately at 375 K) within the temperature range of 300 - 400 K, while another experimental study by Yoon et al. [12] predicts only negative CTE within the temperature range of 200 - 400 K. Overall, experimental studies suggest that the coefficient of thermal expansion of graphene is negative at moderate temperatures (0 - 500 K) [11], [12], indicating that low lying bending phonon modes cause graphene to crumple and thereby shrink in the in-plane direction. Raman spectroscopy and micromechanical measurements suggest graphene to have a negative in-plane coefficient of thermal expansion within the temperature range of 30 K - 300 K [35]–[37]. However, typical experimental evaluations of graphene involve graphene adsorbed on a substrate material, inducing strain from the substrate that significantly affects the lattice parameter and coefficient of thermal expansion value, making the study of freestanding graphene an intriguing topic for theoretical scientists [34], [38]. Ab-initio MD simulation results broadly agree that the coefficient of thermal expansion of graphene is negative over a moderate temperature range but differ in predicting its magnitude. Non-equilibrium green function (NGF) study [39] demonstrates a non-monotonic behavior of CTE with negative CTE observed at moderate temperatures and positive CTE at high temperatures (500 K and above). CTE switches sign at 600 K in this study. Another study using density functional theory by Mounet et al. [16] also predicts a non-monotonic behavior for CTE, but suggests CTE remains negative up to 1000 K, with a minimum value of CTE observed at 300 K. Studies using empirical potential show even more variations in predicting CTE. Adaptive intermolecular reactive empirical bond order (AIREBO) potentials predict a monotonously increasing CTE which remains positive over a wide temperature range and only turns negative below 200 K. Another empirical potential, long-range bond-order potential (LCBOP), predicts CTE to be entirely negative between 0 - 1000 K but with a monotonously increasing behavior [40].

Our MLMD simulations, illustrated in Figure 2.8b, reveal a similar trend in the coefficient of thermal expansion (CTE) as observed in the experimental study by Yoon et al. [12]. Our MLMD simulations suggest that the CTE increases with rising temperature within the range of 125 K to 600 K, with a transition from negative to positive CTE occurring at around 375 K. Beyond 600 K, the CTE stabilizes and does not show further increase up to 1000 K. Classic MD simulations conducted by Gao et al. [41] propose that thermal fluctuations and out-of-plane rippling at moderate temperatures may cause the graphene membrane to contract, exhibiting a negative coefficient of thermal expansion. Such behavior might not be readily apparent in DFT simulations due to the limited number of atoms used to observe rippling. However, classic MD simulations employing empirical potentials may not offer reliable predictions regarding the lattice parameter of graphene, as previously depicted in Figure 2.8a. Experimental studies face limitations in conducting tests on freestanding graphene sheets. Therefore, our MLMD simulations serve as a bridge, facilitating efficient classic MD simulations with comparable accuracy to DFT simulations. In our MLMD simulations, we adopted high sampling of data within the moderate temperature range (125 K - 500 K), obtaining CTE values at

every 25 K interval to precisely capture thermal rippling and out-of-plane fluctuations. Moreover, our model incorporates a much larger graphene sheet size (18 nm x 18 nm), enabling an accurate representation of the rippling effect. Consequently, within the moderate temperature range, MLMD simulations predict that the CTE of graphene should be more negative compared to the findings of Mounet et al. [16], aligning closely with the experimental studies of Yoon et al. [12]. In the high-temperature range (500 K - 1000 K), our results indicate positive CTE values, consistent with the NGF studies conducted by Jiang et al. [39].

The coefficient of thermal expansion (CTE) of graphene is believed to be influenced by two competing mechanisms. Firstly, the rippling effect leading to a linear decrease in CTE with increasing temperature. Secondly, thermal strain which initially results in a non-linear decrease in CTE (0 K - 300 K), followed by a non-linear increase with temperature (300 K - 1000 K) [41]. These mechanisms collectively contribute to an increasing, yet negative, CTE within the temperature range of 0 K - 300 K. During this temperature range, the rate of decrease in thermal strain diminishes with rising temperature, consequently leading to a reduced rate of increase in CTE. Simultaneously, the rippling effect leads in a steady decrease of CTE in the temperature range of 0 K - 1000 K. At approximately 300 K, an inflection point is observed in the thermal strain curve concerning temperature [41]. Beyond 300 K, thermal strain starts to increase with increasing temperature, counteracting the decreasing effect of thermal rippling on CTE. Consequently, CTE undergoes a sign change from negative to positive at 375 K. In the temperature range of 375 K - 1000 K, the increasing thermal strain (with a diminishing slope, which tends to become linear beyond 600 K) and the linear decrease in CTE due to the rippling effect contribute to the stabilization of CTE, eventually reaching a constant value. This behavior of CTE is accurately captured by MLP, as shown in Figure 2.8b.

2.3.2 Young's modulus and ultimate tensile strength

The uniaxial tensile test stands out as one of the most effective method to validate the mechanical properties of graphene and thus was used to assess the efficacy of MLP. The computation of the stress-strain curve in this study involved loading graphene in the armchair direction at a strain rate of 1% per ns across a temperature range of 300 K to 1800 K, as shown in Figure 2.9a. MLMD simulations were conducted using the NPT ensemble with a Nosé-Hoover thermostat, maintaining a constant pressure set at 1 bar. For each temperature at which Young's modulus and ultimate tensile strength needed evaluation, simulations were equilibrated for 10 ns before conducting the uniaxial tensile test. Three tensile tests were performed for each temperature, and Young's modulus and ultimate tensile strength were determined by averaging the results of three similar simulations. As illustrated in Figure 2.9a, the stress-strain curve exhibits a monotonically increasing stress response with increasing strain. Notably, the curve does not display a specific yield point, and the rate of stress increase diminishes with increasing strain. At higher temperatures, a decrease in ultimate tensile strength, strain to failure, and maximum stress can be observed.

Graphene demonstrates an exceptionally high elastic modulus, also known as Young's modulus, making it one of the stiffest naturally occurring materials. In this study, secant modulus was utilized to assess Young's modulus for graphene. Experimental investigations conducted by Lee et al. [9] at 300 K predicted a Young's modulus of 1000 $\pm$ 100 GPa. Similarly, DFT-QHA studies [15] reported a consistent Young's modulus of approximately 1044 GPa for graphene across a temperature range of 10 K to 1000 K. MD simulations employing empirical potentials by Shen et al. [42] projected a Young's modulus of 1002 GPa within the temperature range of 300 K to 700 K. Our MLMD simulations indicated a constant Young's modulus of 975 $\pm$ 80 GPa in the temperature range of 300 K to 1800 K, suggesting a close agreement with previously conducted experimental, DFT, and MD studies, as shown in Figure 2.9b. The stability of Young's modulus with

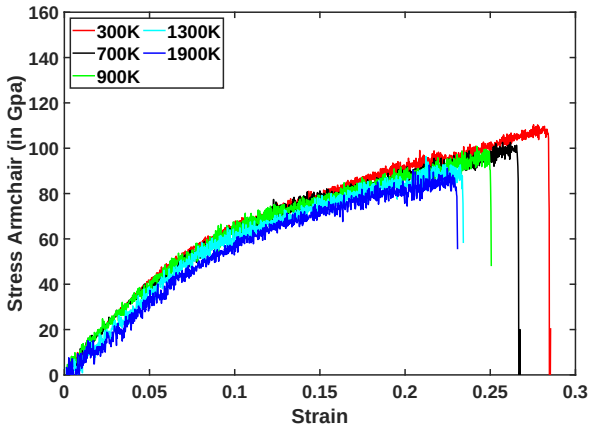

(a)

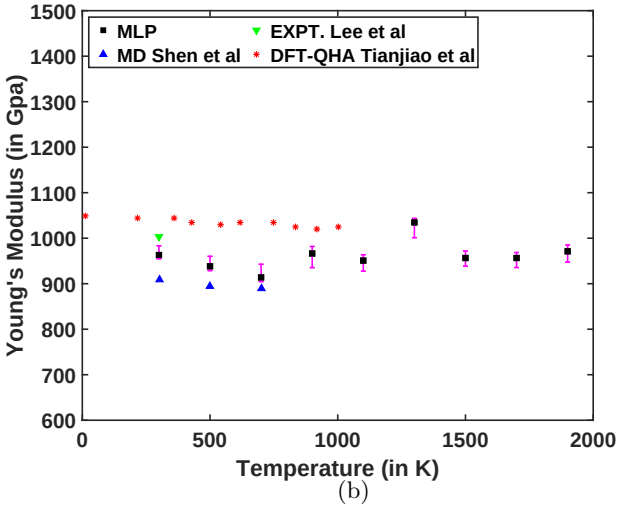

(b)

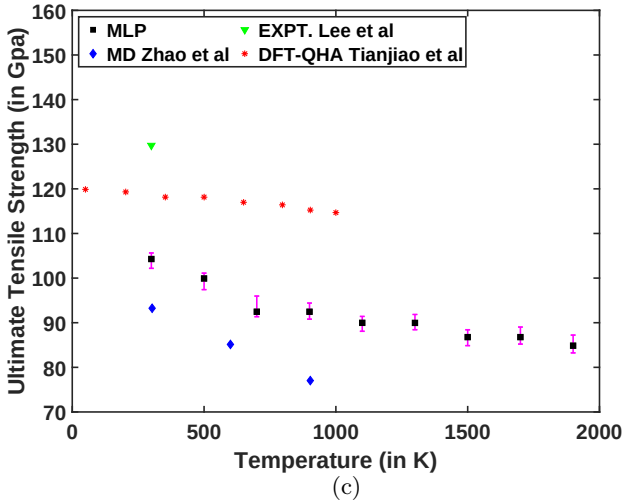

(c)

Figure 2.9: (a) Stress Strain curves for single layer graphene when stretched in armchair direction using MLMD simulations for temperature range of 300 K- 2000 K. It can be noticed that slope of all stress-strain curves at all temperatures are constant but a decrease in ultimate tensile strength with temperature can be observed (b) Temperature independence of Young's modulus and its comparison with other theoretical and experimental results from previous literature studies (c) Monotonically decreasing ultimate strength found using MLMD simulations and comparison with theoretical and experimental results from previous literature studies

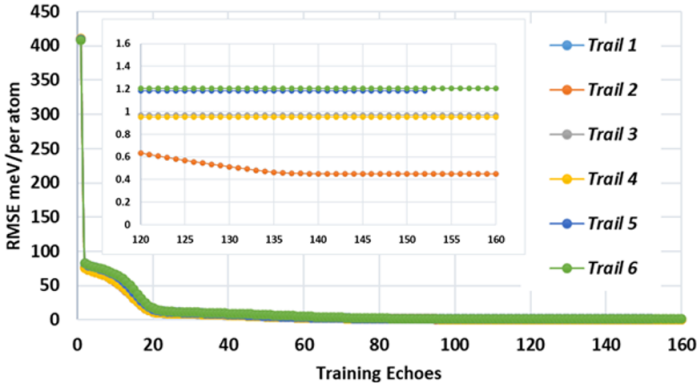

(a)

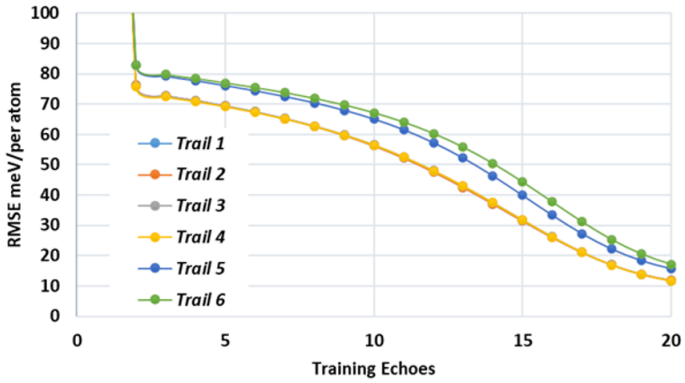

(b)

Figure 2.10: Training history of MLPs using training data generated using 29 symmetry functions is shown

temperature suggests graphene's ability to maintain its exceptional mechanical properties even at elevated temperatures, rendering it a promising candidate for aerospace applications where superior Young's modulus is a sought-after attribute.

Ultimate tensile strength denotes the maximum stress a material can withstand while being stretched just before breaking. The ultimate tensile strength for graphene was compared with experimental, DFT, and MD simulations, as shown in Figure 2.9c. Experimental findings by Lee et al. [9] at 300 K reported an ultimate tensile strength of 129.7 GPa. DFT-QHA simulations by Tianjiao et al. [15] indicated a linearly decreasing ultimate tensile strength with temperature, i.e., 119.9 GPa at 50 K and 114.7 GPa at 1000 K. MD studies conducted by Zhao et al. [43] also suggested a linearly decreasing ultimate tensile strength with increase in temperature, with 93.2 GPa at 300 K and 77.1 GPa at 900 K. The softening in ultimate strength in graphene arises from weaker inter-atomic interactions due to stronger atomic vibrations with increasing temperature. Our MLMD simulations also demonstrated a linearly decreasing ultimate tensile strength, with 104.3 GPa at 300 K and 84.85 GPa at 1800 K. The results from MLMD simulations for ultimate tensile strength closely align with experimental, DFT, and MD studies, exhibiting a similar trend and thereby validating the effectiveness of MLPs.

2.4 Uncertainty quantification of machine learning potentials

Machine learning potentials (MLPs) have the power to change the way of conducting atomistic simulations by enabling reliable and efficient high-throughput computations, which accelerate material discovery and design with unique functionalities and properties. MLPs addresses the challenges of parameterization encountered by empirical potentials and minimize model bias by employing machine learning techniques to interpolate complex potential energy surfaces based on first-principles calculations. Despite their numerous advantages, such as automation and flexible model functions, accurately quantifying systematic uncertainty remains a significant challenge in the development of MLPs. This uncertainty management is crucial for assessing and reducing uncertainties inherent in the developed machine learning interpolated atomic potential energy surface. In this section, we aim to identify the sources of uncertainty associated with the development of machine learning potentials. Subsequently, we will perform systematic sensitivity analysis to quantify the uncertainty and evaluate the reliability of the developed machine learning potential for graphene, a promising two-dimensional material.

2.4.1 Introduction of Uncertainty quantification in machine learning potentials

Despite the construction of machine learning potentials for various material systems in the past two decades, two major challenges persist in applying this new class of potentials for molecular dynamics simulations. Firstly, there's the challenge of quantifying model uncertainty considering various uncertainty resources. Secondly, there's the challenge of mitigating uncertainty to ensure the tractability and fidelity of the developed machine learning potential efficiently. To fully realize the potentials of machine learning force field interatomic potentials, these questions need answers by developing efficient methodologies for uncertainty quantification and management to enhance the validity and predictability of their applications in atomistic simulations. In our previous studies [21], [44], we quantified and illustrated the uncertainty associated with the configuration and training process of artificial neural networks used for developing machine learning potential. Here, we focus on the uncertainty resources in symmetry functions. In this section, sensitivity analysis is conducted for machine learning potentials to investigate the influence of encoding methods on the fidelity of the developed

potential. Specifically, we employ the Behler–Parrinello (B-P) approach combined with high-dimensional ANNs potential for the development of machine learning potentials. Sensitivity analysis is conducted to study the effects of encoding methods to represent the atomic structures in the reference dataset on the quality of the developed machine learning potential. We demonstrate this using sensitivity analysis for graphene with the 30 symmetry functions we used in the previous section.

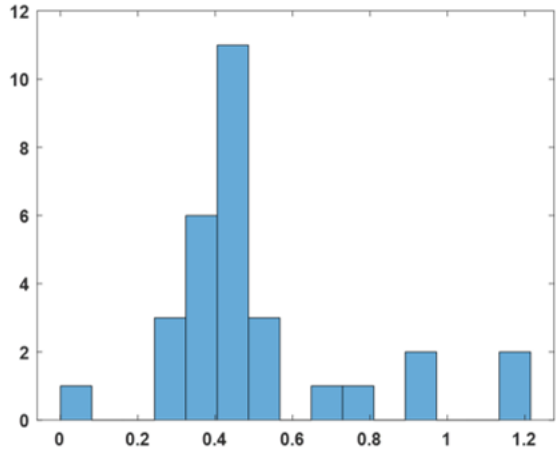

(a)

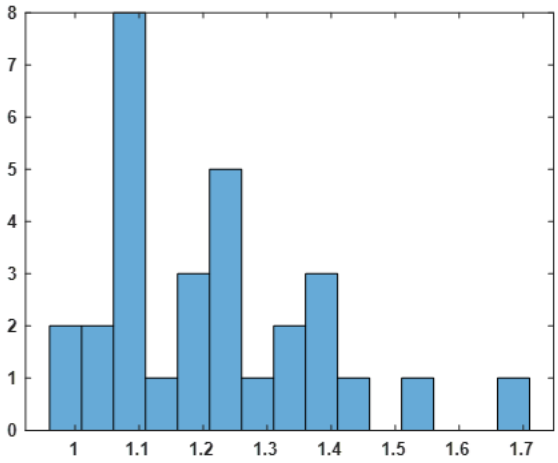

(b)

Figure 2.11: Histogram of converged RMSE for the cases using 29 symmetry functions (a) training dataset (b)testing dataset

2.4.2 Uncertainty quantification in machine learning interatomic potentials

Typically, the density of the encoding process in symmetry function-based systems is determined by the number of symmetry functions employed to transform the coordinates from 3 dimensional cartesian to atomic centered coordinates. Increasing the number of symmetry functions can improve the system's ability to differentiate between various atomic environments and predict their corresponding energies, which is crucial for conducting dynamic trajectory calculations in molecular dynamics (MD) simulations. However, a

higher number of symmetry functions also leads to increased computational costs associated with evaluating the developed machine learning potential at each time step. Additionally, the choice of encoding systems determines the configuration of inputs for training artificial neural networks (ANNs). An increase in the number of symmetry functions results in a higher dimensionality of input layer nodes in ANNs, potentially impact the training process and the final performance of the machine learning potential. Therefore, it is essential to determine the optimal number of symmetry functions and parameters to strike a balance between the accuracy and efficiency of the encoding process.

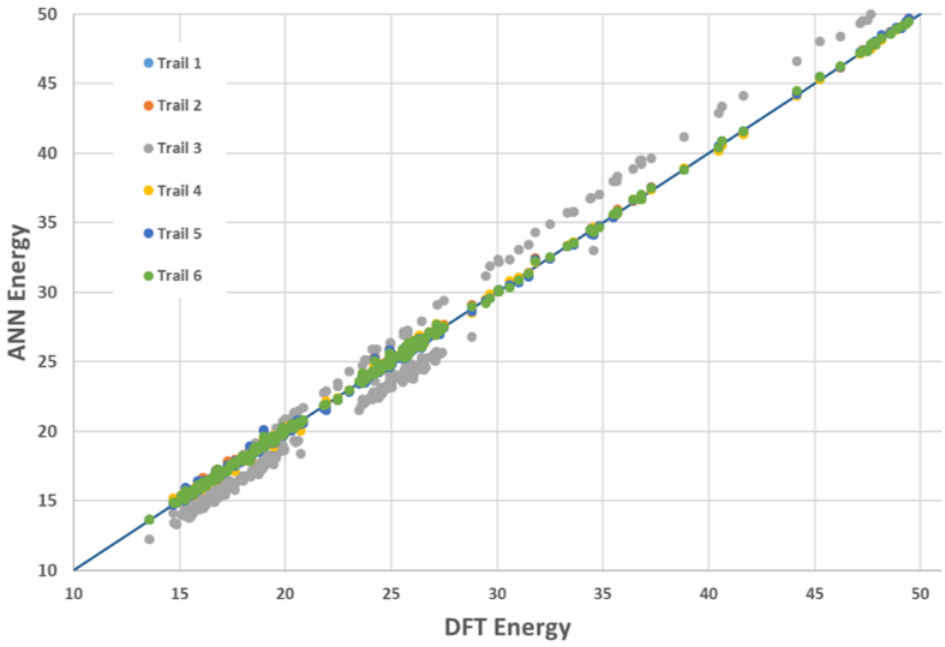

Figure 2.12: Correlation of predicted ANN energy and corresponding DFT energy from first principle calculations for the training data

In our study on graphene, we used a total of 30 symmetry functions, consisting of 10 radial and 20 angular symmetry functions. As a result, the input vector had a dimensionality of 30, corresponding to the number of symmetry functions utilized. To evaluate how the encoding system affects the performance of the machine learning potential, we vary the number of symmetry functions by excluding certain types and quantities of symmetry functions from the encoding system. The baseline scenario involves 30 symmetry functions, resulting in a converged root mean square error (RSME) of approximately 0.57 meV per atom. Initially, we remove one symmetry function, resulting in 30 different cases with 29 symmetry functions each. The RSME history for six different trials with 29 symmetry functions is depicted in Figures 2.10a and 2.10b.

The training process demonstrates rapid convergence of root mean square error (RMSE) within 20 steps, as shown in Figure 2.10b. Although the converged errors vary across the six trials (as shown in the inset of Figure 2.10a), they all remain below 5 meV per atom, meeting the target criterion. To visualize the statistical distribution of the converged error, a histogram of the RMSE for the training data with 29 symmetry functions is presented as shown in Figure 2.11a. Remarkably, the prediction errors are centered around 0.4 meV per atom, with only four cases showing RMSE values exceeding 0.8 meV per atom. This indicates that the removal of one symmetry function out of 30 generally does not significantly affect the training of the ANN-based machine learning potential. However, while the training error is satisfactory, it is

essential to evaluate the performance of the machine learning potential on testing data. As shown in Figure 2.11b, the errors in the testing data are centered around 1.1 meV per atom, which suggests an increase in testing error but the error remains below our target threshold. Note that RMSE is assessed to indicate the weighted average error regarding the performance of the machine learning potential. Figure 2.12 illustrates the correlation of energy between the predicted ANN values and DFT calculation results among the training dataset, revealing the error distribution among sampled configurations. It is noteworthy that the majority of the six trials exhibit a strong correlation of energy between the predicted values and the reference DFT results. However, Trial 3 displays a slight discrepancy between the ANN prediction and the DFT reference values, with underestimation for low-energy states and over-prediction for relatively high-energy states in the training data. Following the removal of two symmetry functions from the initial set of 30, a total of 28 symmetry function cases were generated, resulting in the creation of 100 machine learning potentials. As depicted in Figures 2.13a and 2.13b, the RMSE sharply decreases within the first four steps and converges to relatively low values within 20 steps. The histogram of the converged RMSE for all 100 cases is illustrated in Figure 2.14a for the training data and Figure 2.14b for the testing data. The errors for the training data cluster around 0.5 meV per atom, while those for the testing data center around 1.2 meV per atom. This suggests that removing one additional symmetry function does not substantially affect the performance of the machine learning potential. Although seven cases exhibit RMSE beyond 1.4 meV per atom for training and 1.7 meV per atom for testing, 93% of cases have RMSE values below 0.8 meV per atom for training and 1.5 meV per atom for testing. These findings are promising and indicate the necessity for further exploration into determining the size of the encoding system based on symmetry functions. Further analysis of the RMSE data reveals that removing angular symmetry functions is more likely to result in machine learning potentials with lower accuracy. Additionally, machine learning potentials with converged RMSE values at the higher end of the histogram plots in Figures 2.14a and 2.14b often have the 29th angular symmetry function removed or have two angular symmetry functions removed. A small number of trials were conducted for cases with three and four symmetry functions removed, showing low converged RMSE values, approximately 0.5 meV per atom for the training data and 1.25 meV per atom for the testing data. These results suggest redundancy in the encoding system, which should be impacting the computational efficiency of the current MLPs. However, the this study is limited by the size of the training and testing data (100 training samples and 30 testing samples) due to the computational cost of developing machine learning potentials. This limitation may introduce bias, as the data may be confined to certain phases or deformed conditions, potentially yielding incomplete results. Increasing the size of the training and testing data will be necessary in future studies to draw robust conclusions and identify critical symmetry functions essential for ensuring the reliability of the developed machine learning potential.

2.5 Conclusions

The emergence of machine learning potential represents significant advancement in research, automating the development of high-fidelity interatomic potentials for atomistic simulations aimed at characterizing materials at a fraction of the cost compared to experimental testing and first-principle calculations. In this study, we embarked on developing machine learning potentials employing artificial neural networks (ANNs) and subsequently conducted molecular dynamics (MD) simulations utilizing these interatomic potentials. The potential energy within these MLMD simulations is assessed through the interpolation of the potential energy surface of graphene, derived from ANN models at each time step or as and when needed by the

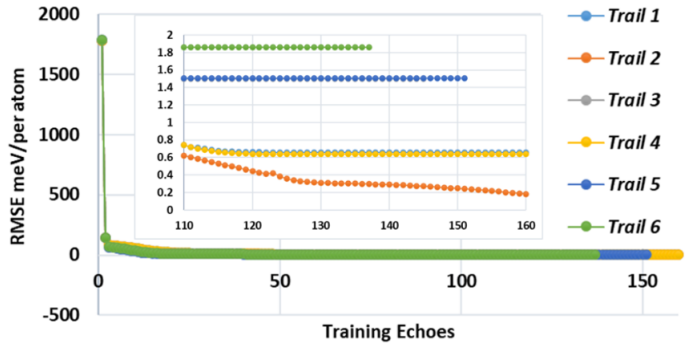

(a)

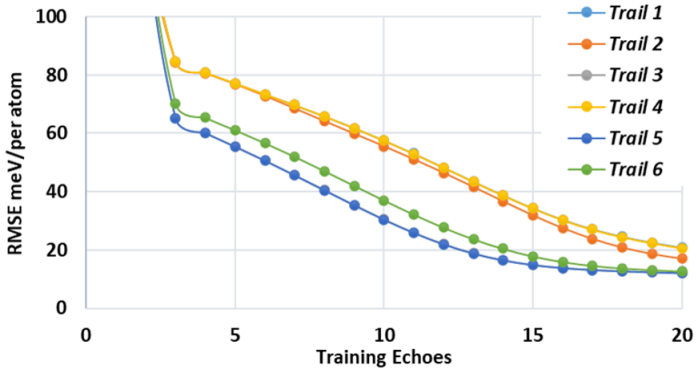

(b)

Figure 2.13: The training history of machine learning potentials based on training data generated using 28 symmetry functions

MD simulation software. To construct our MLP, we generated a training dataset using Density Functional Theory (DFT) simulations by subjecting graphene to stretching in both armchair and zigzag directions. To represent the atomic environment of reference structures for ANN training, we adopted radial and angular symmetry functions. In our investigation, we used two distinct training methods: Gradient Descent (GD) and Levenberg-Marquardt (LM). Our comparative analysis revealed that the LM method showcased remarkable computational efficiency in achieving the target accuracy of the developed Machine Learning Potentials (MLP), outperforming the GD method in this regard.

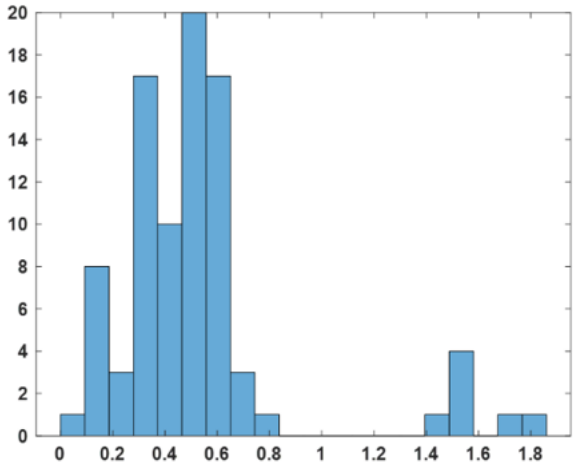

(a)

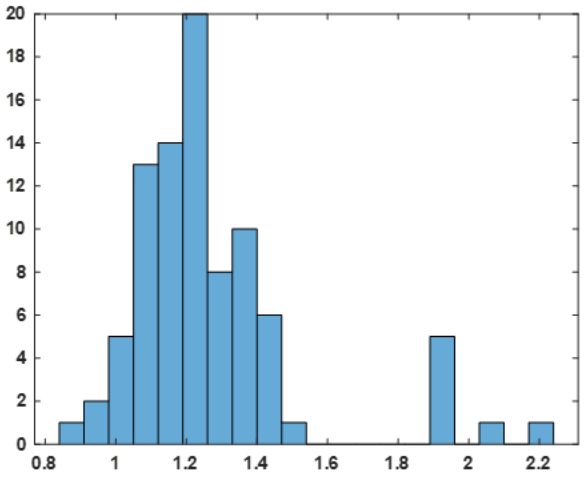

(b)

Figure 2.14: The histogram of converged RMSE for the cases with 28 symmetry functions. (a) is for training data and (b) is for testing data.

We conducted thorough validation to assess the quality of the developed MLPs in this study. Our findings illustrate that by leveraging Artificial Neural Networks (ANN) and symmetry functions, we can establish a dependable interatomic potential for graphene. This MLP offers precise predictions of crucial material properties of graphene such as lattice parameter, Young's modulus, ultimate tensile strength, and coefficient of thermal expansion. We observed that the size of the reference training dataset, which serves as a structural

representation of the phase space, and the strategy used for representing the atomic environment significantly influence the accuracy of the developed MLP. Our study demonstrates that by systematically controlling these pivotal factors, the fidelity of ANN-based MLP can be effectively enhanced. Also, we noted that our MLMD simulations effectively capture the transition in the governing mechanism of the Coefficient of Thermal Expansion of graphene across a broad temperature range from 125 K to 1000 K. This investigation suggests the feasibility of employing ANN to streamline the development of interatomic potential for graphene, thereby accelerating the discovery and design of novel graphene-based functional materials. We also investigated the impact of the encoding system on the performance of the machine learning potential and performed uncertainty quantification through sensitivity analysis. We conducted sensitivity analysis by removing a certain number of symmetry functions to decrease the dimension of training and testing inputs. In our initial study, we examined cases where one or two symmetry functions out of the initial 30 symmetry functions were removed, revealing that all trails in both scenarios exhibited reasonably low Root Mean Square Error (RSME) values for both training and testing data, below the target value. In some case we observed above-average RSME errors, typically involving the removal of certain angular symmetry functions. Moreover, further elimination of symmetry functions, resulting in cases with 27 and 26 symmetry functions, had minimal impact on the performance of the developed machine learning potentials, displaying consistently low RSME values. These preliminary findings suggest significant redundancy in the current encoding system and suggest the potential for dimension reduction in MLP. While further investigation is necessary to mitigate potential biases in the adopted training and testing data, our study suggests the importance of enhancing the encoding system based on the Behler-Parinello method to achieve reduced-dimension training inputs for developing machine learning potential. This will enhance computational efficiency and accuracy, paving the way for future studies aimed at developing MLPs for graphene with structural motifs to characterize unique material behaviors.

In the next chapter, we will delve into the design and development of nanocomposites based on 2D materials. Our focus so far has been on enhancing interatomic potentials for 2D materials to obtain accurate material properties. While 2D materials possess remarkable properties, their practical use as standalone materials is limited due to challenges associated with their one-atomic-layer thickness. To harness the exceptional material properties of 2D materials, a new class of materials known as 2d material based nanocomposites has gained prominence in the last two decades. 2D material based nanocomposites utilize 2D materials as fillers or fibers within a polymer matrix. The domain of nanocomposites presents several challenges, and we have chosen one material system i.e. $MoSe_2$/graphene and polyethylene to address certain material characteristics such as deliberate creation of anisotropy in the developed nanomaterials using 2D materials. The fundamental idea is to adjust the material properties of nanomaterials by incorporating 2D materials. However, understanding the interaction between polymers and 2D materials is crucial, as the interfacial characteristic between these two materials becomes of untmost importance. In the next chapter, our focus will be on investigating the templating effect of 2D materials in conjunction with polymers. We have selected $MoSe_2$/graphene as the 2D material and polyethylene as the polymer to initiate our exploration. By studying the interfacial crystallography, we aim to gain insights into how these materials interact and how this information can serve as a means to modulate the material properties of the resulting nanocomposites. This understanding will provide us with a valuable tuning mechanism to tailor the properties of nanocomposites effectively.

Chapter 3

TEMPLATING EFFECTS OF 2D MATERIALS

3.1 Introduction

Two-dimensional materials possess distinct properties such as large surface area, low specific weight, high specific strength, and well-ordered atomic structure [5], [44], [45] as compared to 3D materials. Graphene, discovered in 2004 by Novoselov et al. [1], was the first naturally occurring 2D material discovered. Subsequently, other 2D materials like h-BN, Phosphorene, MoS_2, $MoSe_2$, among many other 2D materials, have been identified till date. These 2D materials find themselves useful for diverse applications including gas/chemical sensors, electrochemical energy storage devices, aerospace components, membranes, solar cells, flexible electronics [46]–[49] etc. To exploit their exceptional material properties, 2D materials are frequently combined with various polymers to create nanocomposites, offering enhanced material properties compared to polymers for specific applications. These enhancements include improved mechanical strength, thermal, electrical properties, over pure polymer materials. Previous studies [26], [50]–[53] have demonstrated that the addition of 2D materials to polymers, introduces new functionalities in the resulting 2D material based nanocomposites. The overall performance of 2D material based nanocomposites is influenced by multiscale factors, ranging from nanoscale chemical composition to microscale dispersion and alignment of 2D materials, to macroscale constituent composition. Extensive research has highlighted the critical role of interface/interphase (between 2D material and polymer) in determining nanoscale transport behavior between 2D materials and polymer chains [54]. Studies by Hanieh et al. [54] also reveal that mechanical properties of these 2D material based nanocomposites are sensitive to moisture and molecular adhesion effects, indicating interface adhesion degradation when wetted by water for certain 2D material based nanocomposites. Researchers have devoted considerable efforts in characterizing the interface/interphase and its relationship with overall performance of nanocomposites [18], [55], [56]. At the nanoscale level, Li et al. [18] investigated the effect of interfacial load transfer in carbon nanotube–polyethylene nanocomposites on macroscopic bulk elastic material properties of the nanocomposite. Similarly, Pande et al. [56] demonstrated that macroscopic geometric parameters of carbon nanofibers can be altered by using different adhesive layers of catalysts, indicating the impact of change in interfacial behaviour on macrolevel properties of carbon nanofibers.

The microscopic characteristics of the interface/interphase properties in nanocomposites stem from both the interfacial crystallographic form and the morphology of the interphase region, which are outcomes of the

polymer assembly process during crystallization around 2D materials. This process involves heterogeneous nucleation and growth, wherein new phases form on the surface of 2D materials in the case of 2D materials based nanocomposites. Heterogeneous nucleation plays a critical role in determining various material properties of the resulting 2D materials based nanocomposites, such as polymorph selection, crystalline size distribution, melting temperature, stiffness, hardness, chemical resistance [57] etc. In heterogeneous nucleation, nucleating agents often facilitate the crystallization process at the interface between nucleating agent and crystallizing melt. These nucleating agents can be either 2D or 3D in terms of their crystal structure. Compared to 3D nucleation agents which has less controlled surface atomic patterns, 2D materials offer highly controllable atomic patterns, smooth surfaces, and high surface area to mass ratio which facilitates efficient crystallization. Understanding the polymer assembly along the surface of 2D materials, under the influence of interfacial interactions, atomistic structure, processing and environmental conditions, is vital for controlling the crystallization process in polymer-based nanocomposite fabrication. This understanding is critical for us to be able to tailor interface/interphase properties, enabling the design of novel 2D materials based nanocomposites with precise molecular-level design and predictable material properties [55], [58], [59]. Previous studies have delved into the effects of functional groups on interfacial shear properties in nanocomposites, as well as the wettability of 2D materials and their interactions with liquids. These studies have utilized molecular dynamics (MD) simulations to characterize load transfer between functionalized graphene-polymer interfaces and investigate normal and sliding mode force-separation responses [55], [58], [59]. However, there has been limited exploration of dynamic polymer assembly during the crystallization process along the surface of 2D materials, considering nanoscale material structure details. Experimental exploration becomes even more difficult due to relevant (extremely small) length and temporal scales during the crystallization process. Till date, most insights into the crystallization process of 2D materials based nanocomposites have relied on passive evidences such as macroscopic characterization rather than direct observation [60], [61].

In materials science, interface-induced crystallization stands as a complex phenomenon emerging at the intersection of crystalline polymers and solid substrates. While this research extensively delves into the intricate mechanisms governing this process, it's crucial to recognize the pivotal roles of adsorption and pre-freezing phenomena in shaping the interaction between polymers and surfaces. Adsorption is phenomenon where polymer chains adhere to substrate surfaces and fundamentally influences the crystallization kinetics and structural organization of polymers [62]. The attachment of polymer chains to solid substrates precedes crystallization and significantly affects the nucleation and growth of crystalline domains on/around the surface of nucleating agent. Another phenomenon known as pre-freezing in which polymer segments near the substrate experiences reduced mobility and undergo amorphous-to-ordered transition is also critical in understanding the initial stages of interface-induced crystallization [63] processes. These phenomena have been investigated across various material systems, including polymer-metal interfaces, polymer-graphene interfaces, and polymer-semiconductor interfaces [64] in the previous studies. Acknowledging the influence of adsorption and pre-freezing is crucial in understanding the complexities of polymer behavior at interfaces. Thus, adsorption and pre-freezing process understanding is particularly relevant in the context of current study where we investigate crystallization of polyethylene on $MoSe_2$ surface (which is explored in this study).

Computational methods such as molecular dynamics (MD), Monte Carlo simulations, and multi-physics simulations serve as invaluable tools for simulating material behavior, especially in cases where experimental studies face challenges in providing insights due to limitations in technology, cost, and time scales of material activity [65]–[68]. MD simulations, in particular, have gained widespread adoption for simulating and

unraveling material behaviors at small length and time scales [69], offering a new perspective to already present experimental studies. Previous MD simulation studies by researchers have explored the dynamic assembly of organic and inorganic molecules under varying environmental and processing conditions [70]–[72]. For instance, Bourque et al. [71] used MD simulations to systematically vary interatomic interactions, enabling a comprehensive screening of entire material families for nucleating agent activity. Bourque et al. [71] found that the induction time for heterogeneous nucleation during polyethylene crystallization on tetrahedrally coordinated crystals depends on the crystallographic registry between the nucleating agent and the size of critical nucleus of polyethylene. Another study by Ming et al. [72] investigated crystal nucleation and growth in structurally restricted polymer systems using MD simulations, revealing that the presence of more grafted chains increases the number of crystal nuclei, shortens the nucleation induction time and accelerates crystallization process. Previous studies, in general, provide valuable insights into the dynamic crystallization process of polymer molecules at the nano-level and shed some light on the mechanism governing the assembly of polymer molecules in the presence of nucleating agents. Additionally, MD simulations offer valuable insights into the macro-level material properties of 2D material based nanocomposites, particularly the effects of interphase/interface, which can be challenging to establish experimentally [73], [74]. For example, Chanwook et al. [73] demonstrated through MD simulations that the bulk-level mechanical properties of graphene-reinforced nanocomposites, including shear modulus, depends strongly on the interfacial adhesion between graphene and the epoxy matrix. They also suggested that functionalizing the interface between graphene and epoxy can alter the shear modulus significantly. Similarly, Xiong et al. [74] investigated the interfacial mechanical characteristics of carbon nanotube (CNT)-reinforced epoxy composites using MD simulations. They found that the interfacial shear strength of CNT-epoxy nanocomposites can be improved by adjusting parameters such as epoxy density, CNT length and diameter of CNT. These studies suggests the utility of MD simulations in characterizing the interfaces of nanocomposites, which play a crucial role in determining the macro-level mechanical properties of resulting nanocomposites.

Numerous studies have delved into the crystallization of polyethylene, but little attention has been paid to investigating the heterogeneous nucleation process using 2D materials as nucleating agents. Moreover, molecular-level investigations of the crystallization and assembly of polyethylene chains on the surface of 2D materials are exceedingly rare. In this research, we conducted all-atom simulations to analyze the assembly of polyethylene chains on the surface of $MoSe_2$ using molecular dynamics (MD) simulations. $MoSe_2$, a member of the transition metal dichalcogenide family MX_2 (M=Mo, W, X=S, Se), crystallizes in 2H-MoS_2 structures and is renowned for its superior electrical conductivity, finding applications in the development of solar cells [75]–[77]. Conversely, polyethylene stands as one of the most prevalent semi-crystalline polymers in contemporary usage, boasting commendable chemical and physical attributes coupled with economical production costs. Among all the variants of polyethylene available, low density polyethylene (LDPE), high density polyethylene (PE), and ultra-high molecular weight polyethylene (UHMWPE) enjoy widespread popularity. LDPE finds utility in products where attributes like low tensile strength, heightened flexibility, and reduced density are paramount, such as grocery bags, plastic wraps, and food containers. HDPE is favored for structural applications where attributes like abrasion resistance and superior mechanical properties, including stiffness and tensile strength, are critical for example HDPE is usually seen in drainage pipes and outdoor furniture. UHMWPE is used in contexts where characteristics like low friction, high wear resistance, impact strength, and resistance to corrosive chemicals are vital, for example UHMWPE is used in packaging machinery parts and making bulletproof vests. Polyethylene, being a semi-crystalline polymer, undergoes crystallization below its melting temperature [78]. Notably, different types of polyethylene exhibit varying

melting temperatures, with LDPE crystallizing at 367 ± 5 K [79], PE crystallizing at 402 ± 5 K [80], and UHMWPE crystallizing at 419 ± 5 K and below. Accurately simulating the crystallization temperature of polyethylene becomes important as it mirrors the diverse behaviors of its variants and helps in simulating the accurately interfacial registry of polyethylene on the $MoSe_2$ surface, in this study.

Combination of $MoSe_2$ and polyethylene forms a hybrid material system with potential applications in flexible electronics, solar cells, electrochemical devices, healthcare equipment, and beyond [3], [5], [81]. Given its wide-ranging applications, the $MoSe_2$-polyethylene composite stands out as a crucial material system poised to transform various aspects of our lives, thus meriting attention in this study. This research focuses on exploring the process of polyethylene crystallization on the surface of $MoSe_2$, including the resulting crystal orientation and other pertinent parameters governing the assembly process. MD simulations, conducted by the Large-scale Atomic/Molecular Massively Parallel Simulator (LAMMPS) [23], were used to model the behavior of the $MoSe_2$-polyethylene material system. To the best of our knowledge, there exist no prior MD simulation studies investigating $MoSe_2$ as a nucleating agent for polyethylene crystallization. Our hypothesis posits that the larger surface area and regular patterns exhibited by $MoSe_2$ may promote more efficient polymer crystallization, leading to the formation of polymer chains with uniform assembly and long-range order. The primary objective of this study is to showcase the utility of MD simulations in systematically capturing the activity of 2D nucleating agents and elucidating their mechanisms of action. Key aspects of the $MoSe_2$-polyethylene material system investigated in this study include simulating an accurate melting temperature of polyethylene, understanding/analyzing crystallization process of polyethylene on $MoSe_2$ surface, effect of separation distance between crystallized polyethylene and the $MoSe_2$ surface at the interface, adsorption of polyethylene on the $MoSe_2$ surface, interfacial crystallography, pre-freezing effects and crystalline structure of the polyethylene in $MoSe_2$-polyethylene nanocomposites.

3.2 Methodology

This section explains the methodology used for conducting molecular dynamics simulations in the present study. It is divided into two main subsections. The first subsection explores the interatomic potentials and the associated mathematical formulations utilized to facilitate the investigation. The second subsection delves into the specifics of the molecular dynamics simulations, covering details such as the chosen ensemble, operational parameters, and other pertinent factors utilized to mimic the real-world behavior of $MoSe_2$-polyethylene nanocomposite in MD simulations.

3.2.1 Interatomic potentials

To conduct molecular dynamics simulations of the $MoSe_2$-polyethylene hybrid material system, all-atomic models were created. The simulation setup comprised n-pentacosane (n=91) chains to simulate the behavior of polyethylene, while a single-layer $MoSe_2$ sheet with 360 atoms represented the nucleating agent present in all simulations condcuted in this study. For interactions within the $MoSe_2$ layer, Stillinger-Weber (SW) potentials were used. Intrachain interactions within the polyethylene chains were determined using the Consistent Valence Forcefield (CVFF) potential, incorporating bonds, angles, and dihedral interactions. Harmonic potentials governed bond and angle interactions, while OPLS potentials described dihedral interactions. Interactions between polyethylene chains themselves and the interface with Mo and Se atoms were characterized using Lennard-Jones (LJ) potentials. The Stillinger-Weber potential integrates two-body and three-body interactions, considering the bond energy's reliance on atomic distances and bond angles. The total energy in

the SW potential is expressed as a summation of two-body and three-body interactions. Specifically, the SW potential is represented by Equation 3.1, while the equations governing the two-body interactions (3.2) and three-body interactions (3.3) are provided as follows:

$$\phi_{sw} = \sum_{i} \sum_{j>i} \phi_2 \left(r_{ij}\right) + \sum_{i} \sum_{j=i} \sum_{k>j} \phi_3 \left(r_{ij}, r_{ik}, \theta_{ijk}\right) \tag{3.1}$$

$$\phi_2 \left(r_{ij}\right) = A_{ij}\epsilon_{ij} \left[B_{ij} \left(\frac{\sigma_{ij}}{r_{ij}}\right)_{ij}^{p} - \left(\frac{\sigma_{ij}}{r_{ij}}\right)_{ij}^{q}\right] \times \exp\left(\frac{\sigma_{ij}}{r_{ij} - a_{ij}\sigma_{ij}}\right) \tag{3.2}$$

$$\phi_3 \left(r_{ij}, r_{ik}, \theta_{ijk}\right) = \lambda_{ijk}\epsilon_{ijk} \left(\cos\theta_{ijk} - \cos\theta_{0ijk}\right)^2 \times \exp\left(\frac{\gamma_{ij}\sigma_{ij}}{r_{ij} - a_{ij}\sigma_{ij}}\right) \times \exp\left(\frac{\gamma_{ik}\sigma_{ik}}{r_{ik} - a_{ik}\sigma_{ik}}\right) \tag{3.3}$$

Here, r_{ij} represents the bond length between i_{th} and j_{th} atoms, θ_{ijk} signifies the bond angle formed by the bonds r_{ij} and r_{jk} at the j_{th} vertex. Parameters like A, B, p, and q are utilized for the evaluation of two-body interactions, while λ and θ_0 are used for both two and three-body interactions. γ parameter is only used in three-body interactions.

In the case of polyethylene, the total energy associated with the stretching of covalent bonds can be described using a two-body potential that captures the change in distance between two atoms bonded together. This potential is formulated as shown in Equation 3.4:

$$E_b = \sum_{i=1}^{nb} K_b^i \left(r^i - r_o^i\right)^2 \tag{3.4}$$

Here, r^i represents the distance between two atoms connected by the i_{th} covalent bond, r_o^i is the equilibrium distance between these atoms for the i_{th} covalent bond, K_b^i denotes the stiffness of the covalent bond, and nb signifies the total number of covalent bonds in the system. Note that each covalently bonded atom has preferred angular orientations. Hence, there exists a potential energy component associated with these angular orientations, described by Equation 3.5:

$$E_a = \sum_{i=1}^{na} K_\theta^i \left(\theta^i - \theta_o^i\right)^2 \tag{3.5}$$

In this equation, θ^i represents the angle formed between the i_{th} pair of two covalent bonds, θ_o^i is the equilibrium angle for this pair, K_a^i is the stiffness parameter used for angular interactions, and na indicates the total number of angles in the system. Similarly, the torsional interaction involving four adjacent atoms, known as dihedrals, contributes to the potential energy. This interaction is shown in Equation 3.6:

$$E_t = \sum_{i=1}^{nd} K_\phi^i \left[1 + d_i \cos\left(m^i \left(\phi^i - \phi_o^i\right)\right)\right] \tag{3.6}$$

Here, ϕ_o^i represents the equilibrium dihedral angle between atoms i, j, k, and l, d_i is a parameter defining the sign convention (which can be either +1 or -1), m^i is a non-negative integer coefficient, K_ϕ^i is the stiffness parameter used for dihedral interactions, and nd represents the total number of dihedrals in the material system. Lastly, a non-bonded pair potential arises from interactions between non-covalently bonded atoms, commonly referred to as van der Waals interactions. This interaction is described by the Lennard-Jones

potential, as shown in Equation 3.7:

$$E_p = 4 \sum_{i=1,j\ =i}^{n} \epsilon_{ij} \left[\left(\frac{\sigma_{ij}}{r_{ij}} \right)^{12} - \left(\frac{\sigma_{ij}}{r_{ij}} \right)^{6} \right], r < r_c \tag{3.7}$$

In this equation, ϵ_{ij} represents the energy well depth between the i_{th} and j_{th} atoms, r_{ij} is the distance between i_{th} and j_{th} atoms, σ_{ij} denotes the equilibrium distance between i_{th} and j_{th} atoms, n stands for the total number of atoms in the system, and r_c is the cutoff distance beyond which the force between the atoms can be considered negligible. Consequently, the total potential energy of the $MoSe_2$-polyethylene composite system can be established by summing up the six distinct potential energy components, as shown in Equation 3.8.

$$E_{total} = E_b^{poly} + E_a^{poly} + E_t^{poly} + E_p^{poly-poly} + E_{sw}^{MoSe_2} + E_p^{poly-MoSe_2} \tag{3.8}$$

Here, E_b^{poly} represents the bonded energy of polyethylene, which can be computed using Equation 3.4. E_a^{poly} signifies the angular energy stored in polyethylene chains, which can be derived from Equation 3.5. E_t^{poly} denotes the torsional energy stored in polyethylene chains, computed using Equation 3.6. $E_p^{poly-poly}$ corresponds to the non-bonded van der Waals interaction between different polyethylene chains, computed using Equation 3.7. $E_{sw}^{MoSe_2}$ encompasses the total energy of $MoSe_2$, which can be obtained using Equations 3.1-3.3 using Stillinger-Weber potentials. Lastly, $E_p^{poly-MoSe_2}$ characterizes the non-bonded van der Waals interaction between polyethylene and $MoSe_2$, computed using Equation 3.7.

Tuning interatomic potentials for establishing melting temperature of polyethylene

The behavior of n-pentacosane chains, representing polyethylene in this study, is heavily influenced by interchain interactions, particularly impacting their crystallization and melting behavior. Therefore, to accurately model the crystallization behavior of polyethylene chains, the Lennard-Jones (LJ) potentials governing the intermolecular interactions among n-pentacosane chains were adjusted. In this study, the LJ potential parameters based on the work of Li et al. [55] were utilized as a reference in this investigation. These parameters include values of $\epsilon = 0.0034692$ eV and $\sigma = 3.4745\mathring{A}$ for the van der Waals interaction between carbon atoms within different polyethylene chains i.e. interchain interactions.

Evaluation of melting temperature (T_m) across different polyethylene models was conducted via MD simulations, utilizing varied interchain interactions and temperatures, as shown in Figure 3.1. To gauge the crystallization process and monitor the transition between crystallization and melting, a global crystalline parameter, denoted as P_2 [71], was used. This parameter, derived from the global average of the local order parameter $p_2(i)$, aids in characterizing the degree of crystallinity within polyethylene. In all the MD simulations presented in this study, the starting point is a partially crystallized polyethylene system with an initial P_2 value of 0.311 that underwent equilibration for 5 ns with different value of interaction parameter (each in a different MD simulation). The temporal evolution of P_2 was recorded across various combinations of different LJ parameters and temperatures, as shown in Figure 3.1. An upward trend in P_2 over time signifies the onset of nucleation and crystallization, while a decline in P_2 over time indicates a melting process. Thus, the melting temperature can be estimated as the average of two temperatures, T_1 and T_2, where P_2 increases at T_1 and decreases or stabilizes at T_2. In this study, LJ parameters were borrowed from Li et al.'s study [55] which served as a reference interatomic interactions between polyethylene chains. The interchain interaction within polyethylene was adjusted by applying a common factor to the van der Waals interaction between

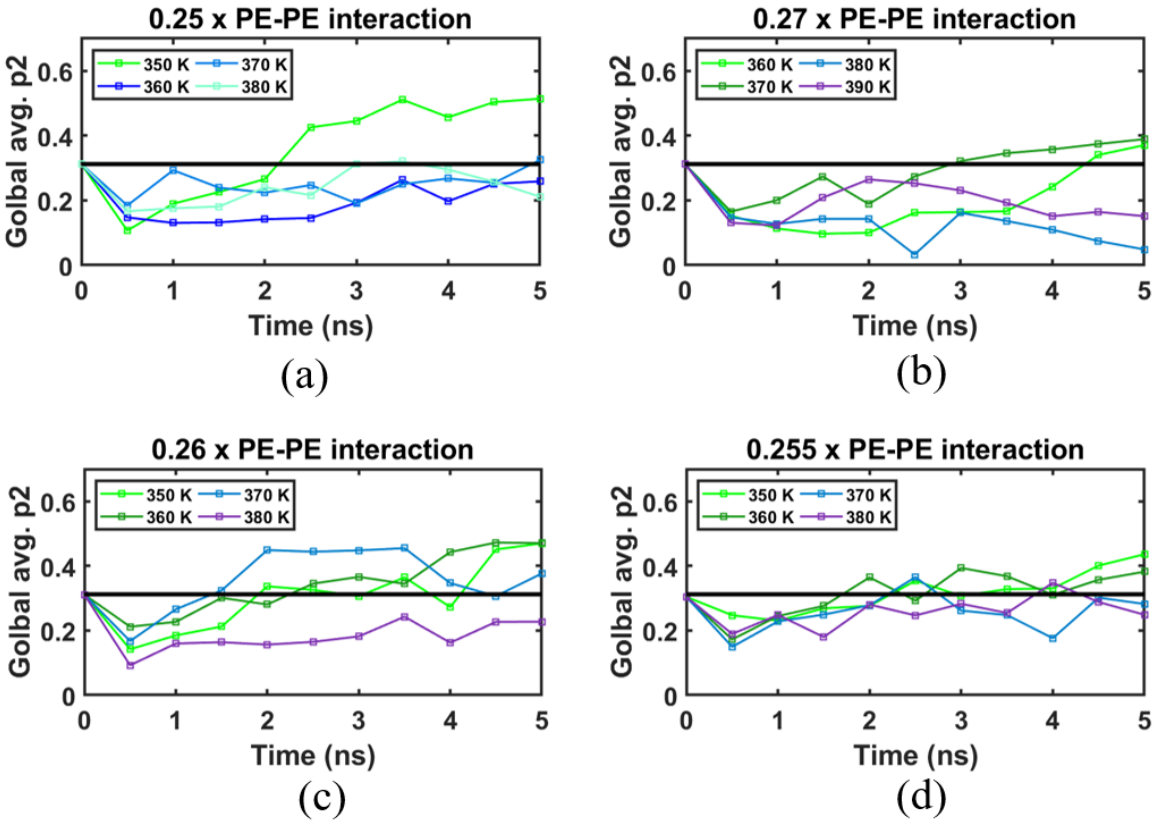

Figure 3.1: The effect of the Lennard-Jones parameter governing polyethylene-polyethylene (PE-PE) interactions on the melting temperature of polyethylene (n-pentacosane chains) is examined. In (a), the crystallization of polyethylene on the $MoSe_2$ surface is depicted with a PE-PE interaction parameter set to 0.25 times interaction parameter from Li et al.'s investigation [19]. This graph suggests a melting temperature range of 350 - 360 K. Similarly, in (b), with a PE-PE interaction parameter of 0.27 times interaction parameter from Li et al.'s investigation [19], the estimated melting temperature of polyethylene falls within the range of 370 - 380 K. (c) illustrates the polyethylene melting temperature range between 370 - 380 K with a PE-PE interaction parameter of 0.26 times interaction parameter from Li et al.'s investigation [19]. Finally, in (d), for a PE-PE interaction parameter of 0.255 times interaction parameter from Li et al.'s investigation [19], the polyethylene melting temperature range spans 360 - 370 K.

carbon-carbon, carbon-hydrogen, and hydrogen-hydrogen interactions, as represented by the Lennard-Jones interaction parameter ϵ in the MD simulations. Figure 3.1 (a) depicts the $MoSe_2$-polyethylene system with a 0.25-times interchain interaction from Li et al.'s study [55]. Notably, the parameter P_2 decreases at 360 K and increases at 350 K. This behavior suggests that the melting temperature T_m falls between 350 K and 360 K, yielding an estimated melting temperature of approximately 355 K. In Figure 3.1 (b), the $MoSe_2$-polyethylene system with a 0.27-times interchain interaction from Li et al.'s study [55] exhibits an estimated T_m of around 375 K. Similarly, in Figure 3.1 (c), the system with a 0.26-times interchain interaction from Li et al.'s study [55] shows a comparable T_m of approximately 375 K. In Figure 3.1 (d), the scenario with a 0.255-times interchain interaction from Li et al.'s study [55] suggests a melting temperature of about 365 ± 5 K. Interestingly, this value corresponds well with experimental observations [79], which reported a melting temperature of polyethylene as $T_m = 367$ K. Consequently, an interchain interaction of 0.255-times has been adopted for all subsequent simulations. These findings indicate a consistent increase in T_m with a rise in the PE-PE interchain interaction, thereby providing a valuable parameter to control the behavior of short/long alkane chains to accurately represent the melting temperature in longer polyethylene chains.

Theory of crystallization

To understand the crystallization process, it is essential to introduce key concepts crucial for subsequent discussions. One such concept is the local orientation parameter denoted as p_2, which is fundamental in assessing the crystallinity of carbon atoms within polyethylene as established by Rutledge et al and Bourque et al. [71], [82]. In this study of $MoSe_2$-polyethylene material system, p_2 was computed for all 25 carbon atoms in each of the 91 polyethylene chains. This parameter, p_2, is defined by Equation 3.9:

$$p_2(i) = \langle (3 < \cos^2 \theta_{ij} > -1)/2 \rangle_j \tag{3.9}$$

Here, $p_2(i)$ represents the local orientation parameter for the ith carbon atom. It is computed for each atom i within the material system, considering another atom j within a specified cutoff distance r_{ij}. θ_{ij} denotes the angle between the vector linking the $(i-1)$th carbon atom and the $(i+1)$th carbon atom, and the vector connecting the $(j-1)$th carbon atom to the $(j+1)$th carbon atom. While p_2 parameter quantifies crystallization for individual carbon atoms, it doesn't capture the overall crystallization state of the material system.nTo quantitatively determine the crystallization state of the entire material system at each time step, polyethylene in this study, an ensemble average of p_2 is computed, referred to as the global orientation order parameter P_2. Equation 3.10 outlines the definition of the global orientation order parameter P_2.

$$P_2 = \langle (3 < \cos^2 \theta_{ij} > -1)/2 \rangle_{i \neq j} \tag{3.10}$$

In this equation, the average of p_2 is computed over all pairs of i and j carbon atoms within the material system, irrespective of the distance between them. To categorize an atom as crystallized, a threshold $p_{2,th}$ is selected, where carbon atoms with p_2 values exceeding $p_{2,th}$ are designated to the crystal phase. Moreover, the determination of whether two carbon atoms, i and j, belong to the same crystal nucleus involves verifying that $r_{ij} < r_{th}$. To understand crystallization in polyethylene, appropriate values for r_{p2}, r_{th}, and $p_{2,th}$ must be chosen. Referring to the findings of Rutledge et al. [82], we have chosen $r_{ij} = 1.5\ \sigma_{pp}$, $r_{p2} = 2.5\ \sigma_{pp}$, and $p_{2,th} = 0.4$, where σ_{pp} represents σ_{ij} from Equation 3.10, related to the polyethylene-polyethylene van der Waals interaction within this investigation.

3.2.2 Molecular dynamics simulations

Molecular dynamics (MD) simulations conducted in this study were carried out using isothermal-isobaric ensemble, maintaining a temperature of 360 K and a pressure of 1 atmospheric unit. The positions and velocities at each time step (ts = 1 fs) were generated using non-Hamiltonian equations based on the Nose-Hoover style. To smooth pressure and temperature fluctuations, a barostat with a pressure damping frequency of $\omega_P = \left(\frac{1}{1000fs}\right)$ and a thermostat with a temperature damping frequency of $\omega_T = \left(\frac{1}{100fs}\right)$ were utilized. The $MoSe_2$-polyethylene simulation box had a triclinic shape due to the inherent symmetry of $MoSe_2$, with dimensions of 46 x 33.5 x 42 $\AA^3$ and an inclination of 120° in the xy plane. All side lengths of the box were allowed to independently fluctuate, while periodic boundary conditions were applied in all three directions. The $MoSe_2$ sheet was positioned at the lowermost part of the simulation box, and the polyethylene model consisted of 91 chains, each containing 25 carbon atoms. In total, the material system comprised 7367 atoms, including the 2D $MoSe_2$ sheet with 360 atoms.

The initial configuration involved positioning fully extended polyethylene chains into 7 layers, with each layer containing 13 chains, resulting in an initial density of 0.945 g/cc. An energy minimization using the conjugate gradient algorithm was performed to establish a stable initial configuration and alleviate internal stresses. Following energy minimization, the MD simulations were initiated under the NPT ensemble. The $MoSe_2$-polyethylene model was equilibrated at 20 K for 100 picoseconds (ps) to mitigate pressure fluctuations and achieve stabilization. Subsequently, the temperature was gradually increased from 10 K to 500 K over 100 ps to establish a temperature well above the melting point of polyethylene to achieve a randomly mixed polyethylene chains. Afterward, the system was equilibrated for 1 nanosecond (ns) at the elevated temperature to stabilize the polyethylene in a liquid state. To simulate the assembly process of the polymer, the simulation model was rapidly cooled from 500 K to 360 K within 100 ps, creating a temperature just below the melting point. Following this, the $MoSe_2$-polyethylene material system was allowed to crystallize for 100 ns at a temperature of 360 K, observing the dynamic assembly process during this period.

Crystallization process

After adjusting the interchain interaction parameters to achieve a melting temperature of approximately 365 ± 5 K, in the next phase we observed the crystallization process of polyethylene chains on 2D $MoSe_2$ surface. The initial mixture of polyethylene chains at 500 K was allowed to crystallize at 360 K for 100 ns. To monitor the progress of crystallization, the $MoSe_2$-polyethylene model was divided into multiple layers with a thickness of 0.36 nm each, starting from the $MoSe_2$-polyethylene interface moving along the positive z direction (as illustrated in Figure 3.2). The chosen slice thickness corresponds to the typical thickness of single crystallized layers of polyethylene chain segments in the direction of crystal growth found from previous literatures.

To track the advancement of crystallization within each slice over time, the number of crystalline carbon atoms ($N_c(z)$) were monitored using the local order parameter $p_2(ij)$ as well as the fractional crystallization parameter $X(z)$. Crystalline carbon atoms are identified within each slice based on specific criteria: $p_2(ij) > 0.4$, $r_{ij} < 1.5\sigma_{pp}$ [71], and both atoms i and j should belong to the same slice. The fractional crystallization of a slice, denoted as $X(z)$, is calculated as the ratio of the total number of crystallized atoms to the total number of atoms in the slice along the z direction, expressed as $X(z) = N_c(z)/N_T(z)$ [71], [82].

Figure 3.2 illustrates the progression of fractional crystallinity $X(z)$ profiles at different timesteps i.e. from 0 to 100 ns after the quenching process. Each line in the figure represents the fractional crystallization

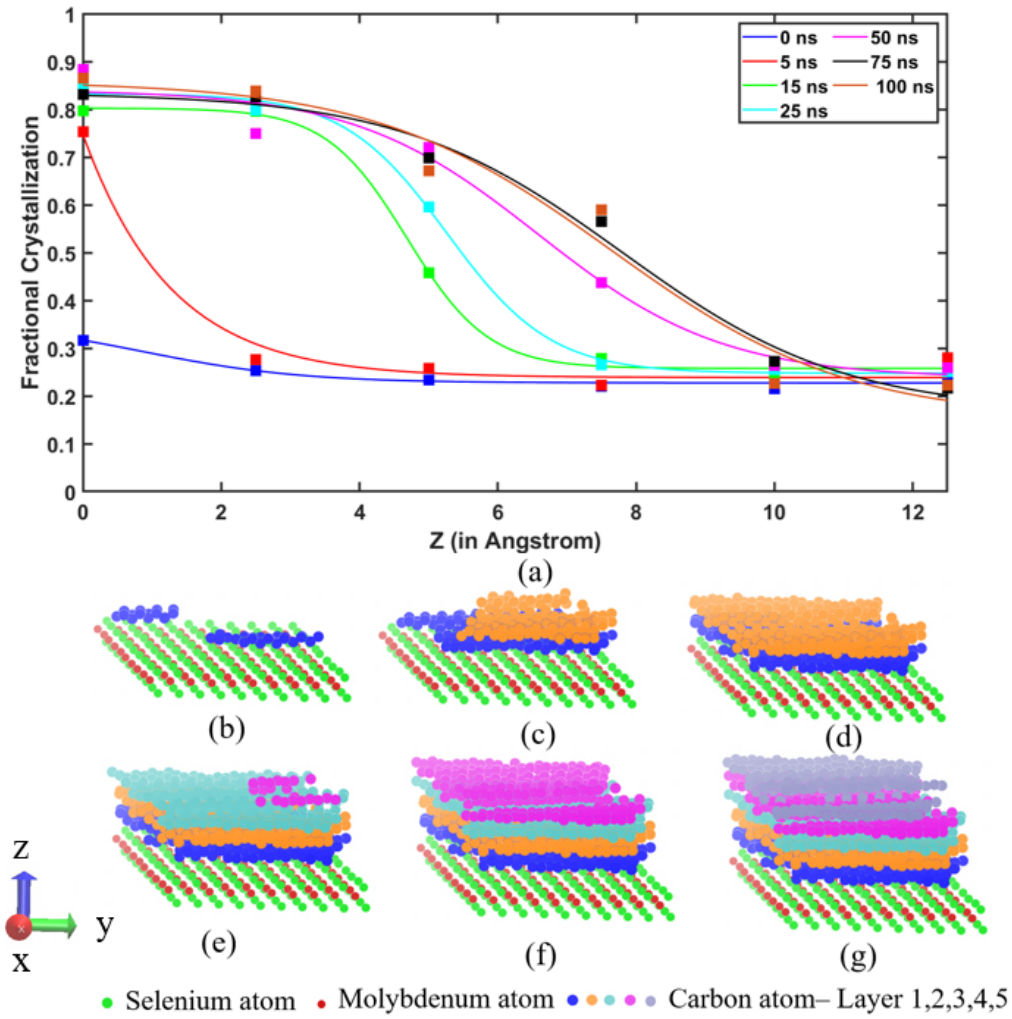

Figure 3.2: (a) This figure illustrates the fractional crystallization profiles of $MoSe_2$ over time just after quenching to 360 K from 500 K. The solid curves represent curve fits of a hyperbolic tangent function to the fractional crystallinity profiles. A vertical line parallel to the y-axis can be drawn that will denote a crystallization growth front at time t suggesting fractional crystallization ($X > 0.4$) on the left side of the crystallization growth front and ($X < 0.4$) on the right side of the crystallization growth front. The images below showcase the crystallization process of polyethylene on the $MoSe_2$ surface with the Miller-Braivais direction index $[\bar{1}2\bar{1}0]$ at (b) 0 ns, (c) 5 ns, (d) 10 ns, (e) 25 ns, (f) 50 ns, and (g) 100 ns after the quenching process

at a specific time, plotted against the distance from the polyethylene-$MoSe_2$ interface in the positive z direction. At the beginning, $t = 0$ ns, $X(z)$ is around 0.3, indicating minimal crystallization. Within the initial 5 ns, $X(z = 0)$ experiences a swift increase from 0.3 to 0.75, marking the onset of crystallization at the $MoSe_2$-polyethylene interface. As time elapses, the z value corresponding to $X(z) = 0.4$ shifts from 1.83 Å at 5 ns to 8.96 Å at 100 ns, indicating that the crystallization growth front starts at the $MoSe_2$-polyethylene interface and moves parallel to the interface towards the bulk polyethylene with the increase in time.

The crystallization growth front can be envisioned as a theoretical plane parallel to the $MoSe_2$-polyethylene interface, moving along the positive z direction starting from the interface. On one side of this crystallization growth front, significant crystallization occurs or crystallized polyethylene, while on the other side, crystallization is minimal or a melted polyethylene. It's important to note that due to periodic boundary conditions, there are two polyethylene-$MoSe_2$ interfaces in our simulation model, situated on opposite sides of the $MoSe_2$ surface and converging toward each other in the z direction. However, Figure 3.2 illustrates the fractional crystallization and crystallization profiles from only one $MoSe_2$-polyethylene interface for clarity. Initially after the quenching process, limited crystallization is observed during the first 5 ns. Then, the crystallization growth front advances rapidly until around 25 ns when multiple layers of highly ordered crystalline polyethylene chains form. Between 25 and 75 ns, the growth front progresses at a slower rate due to competition between the growth fronts from both interfaces, which try to converge and attempt to crystallize the middle section of the simulation box. These two crystallization growth fronts often have different crystallization orientations, leading to incompatibility and slower growth in the intermediate region. Snapshots of ordered and aligned polymer chains growing from the polyethylene-$MoSe_2$ interface is provided in Figure 3.2 (b)-(g) at time points of 0, 5, 10, 25, 50, and 100 ns. These visualizations only display the crystalline carbon atoms, with different colors indicating crystalline carbon atoms in distinct layers for clarity. It's evident that the polymer chains crystallize within their respective layers and subsequently propagate to neighboring layers. After 100 ns, a total of five layers of aligned polymer chains are observed on top of the $MoSe_2$ surface in our MD simulations model.

3.3 Interfacial crystallography and surface guided crystallisation of polyethylene chains on $MoSe_2$ surface

Several MD simulations were carried out to explore how 2D $MoSe_2$ influences the crystallization pattern of polyethylene chains. The interface between polyethylene and $MoSe_2$ was studied to understand their templating effects on polyethylene crystallization. In each simulation run, $MoSe_2$-polyethylene system underwent an initial equilibration phase at 500 K, lasting for 1 ns. Subsequently, the system was rapidly cooled to 360 K to create a temperature below melting temperature and observe the polyethylene crystallization process on $MoSe_2$ surface. Snapshots of the system were taken every 100 ps during the 2.4 ns equilibration period, and these 24 snapshots served as the starting configurations for the crystallization simulations. In total, 24 distinct MD simulations were conducted to capture various realizations of the crystallization process with different starting mix of polyethylene chains on $MoSe_2$ suraface.

Figure 3.3 illustrates the interfacial crystallographic orientations observed in the first layer of polymer chains on the $MoSe_2$ surface. Miller-Bravais direction indices are utilized to represent the crystallographic planes and orientations, employing a 4-axis coordinate system commonly used for characterizing hexagonal crystal structures in three dimensions. In Figure 3.3 (a), (b), and (c), the crystallized polyethylene in the first layer exhibits chain directions aligned with $[\bar{1}2\bar{1}0]$, $[2\bar{1}\bar{1}0]$, and $[\bar{1}\bar{1}20]$ on the (0001) plane of $MoSe_2$. Notably,

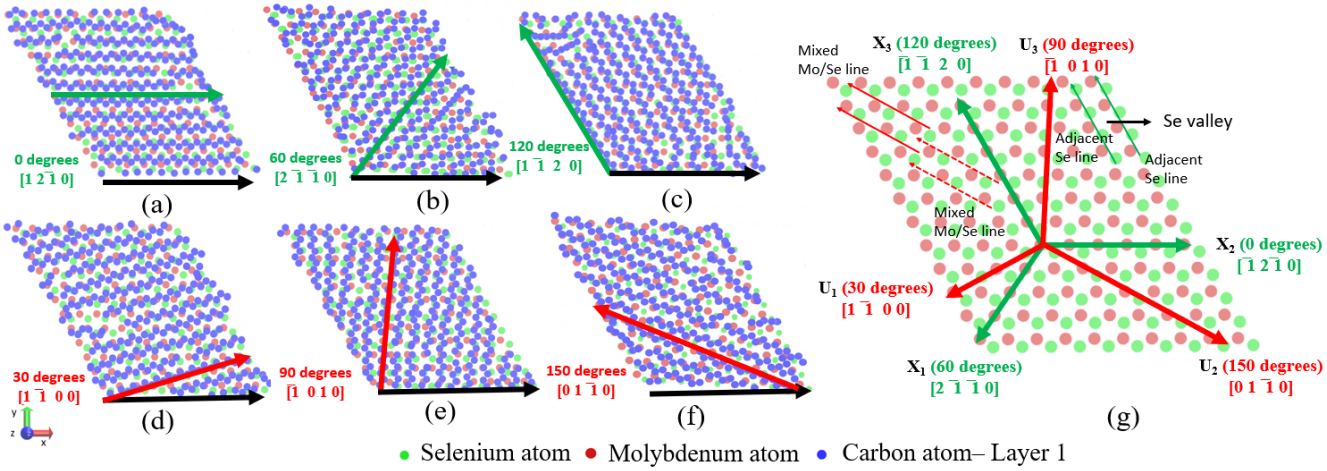

Figure 3.3: Six distinct crystallization orientations were identified from a total of 24 MD simulations where each MD simulation was conducted for 100 ns after quenching from 500 K to 360 K. The reference Miller-Bravais direction index, marked by black arrows, represents 0 degrees/$[\bar{1}2\bar{1}0]$. Green and red arrows denote the angles measured counterclockwise from the Miller-Bravais direction index, 0 degrees/$[\bar{1}2\bar{1}0]$. For clarity, only one layer of crystallized polyethylene is shown in each orientation: (a) 0 degrees/$[\bar{1}2\bar{1}0]$, (b) 60 degrees/$[2\bar{1}\bar{1}0]$, (c) 120 degrees/$[\bar{1}\bar{1}20]$, (d) 30 degrees/$[1\bar{1}00]$, (e) 90 degrees/$[\bar{1}010]$, and (f) 150 degrees/$[01\bar{1}0]$. Image (g) illustrates the Miller-Bravais indices of directions for equivalent configurations. The principal hexagonal directions, X_1, X_2, and X_3, represent symmetric/equivalent valleys between adjacent Se lines. Similarly, U_1, U_2, and U_3 are three other symmetric/equivalent directions representing valleys between mixed Mo/Se lines.

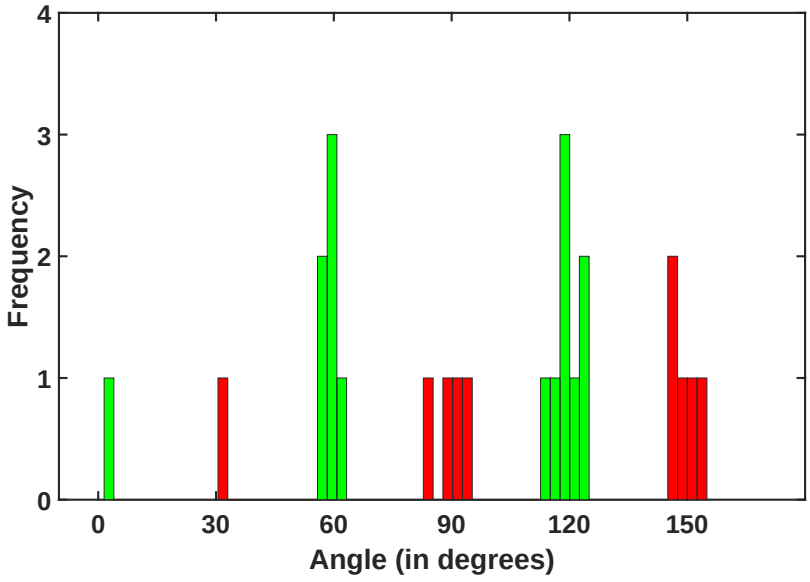

Figure 3.4: The histogram represents the distribution of angles observed counterclockwise with the Miller-Bravais direction index $[\bar{1}2\bar{1}0]$ across 24 individual crystallization simulations of polyethylene on the $MoSe_2$ surface. Crystallization orientations at 0°, 60°, and 120° are displayed in green, while those at 30°, 90°, and 150° are displayed in red

the polyethylene chains align in the valleys between Se lines, denoted by the green lines in Figure 3.3 (g). On the other hand, Figure 3.3 (d), (e), and (f) depict crystallized polyethylene chains oriented along $[1\bar{1}00]$, $[\bar{1}010]$, and $[01\bar{1}0]$ on the (0001) plane of $MoSe_2$. These orientations suggest that the polyethylene chains tend to align between mixed Mo/Se lines, illustrated by the red lines in Figure 3.3 (g). By using $[\bar{1}2\bar{1}0]$ as the reference direction at 0°, the orientations $[\bar{1}2\bar{1}0]/[2\bar{1}\bar{1}0]/[\bar{1}\bar{1}20]$ are considered for 0°/120°/60°, while $[1\bar{1}00]/[\bar{1}010]/[01\bar{1}0]$ are considered for 30°/90°/150° for specifying crystallization orientations. Each direction within these two sets of crystallographic orientations exhibits a 60° difference. Importantly, these two sets of crystallization orientations $[\bar{1}2\bar{1}0]/[2\bar{1}\bar{1}0]/[\bar{1}\bar{1}20]$ and $[1\bar{1}00]/[\bar{1}010]/[01\bar{1}0]$ maintain symmetry relative to the (0001) plane of $MoSe_2$, owing to the atomic structure symmetry of molybdenum and selenium atoms. These observed crystallographic orientations of the crystalline polyethylene chains exhibit a standard deviation of ± 5° when characterizing the angles.

Table 3.1: The crystallization orientations were observed across 24 independent MD simulations, each starting with mixed polyethylene on the $MoSe_2$ surface. The angles, measured in degrees, represent the deviation in a counter-clockwise direction from the reference Miller-Bravais direction index $[\bar{1}2\bar{1}0]$ The total number of crystallized structures corresponding to each Miller-Bravais direction index out of the total 24 simulations has also been indicated

Angle (in degrees)	Miller-Bravais dir.	No. of Config.
0	$[\bar{1}2\bar{1}0]$	1
60	$[2\bar{1}\bar{1}0]$	5
120	$[\bar{1}\bar{1}20]$	8
30	$[1\bar{1}00]$	1
90	$[\bar{1}010]$	4
150	$[01\bar{1}0]$	5

From Table 3.1, it is evident that 58.3% of the MD simulations, accounting for 14 out of 24 simulations, exhibit interfacial crystallographic orientations aligned with (0°/$[\bar{1}2\bar{1}0]$, 60°/$[2\bar{1}\bar{1}0]$, 120°/$[\bar{1}\bar{1}20]$). Similarly, 41.7% of the MD simulations, comprising 10 out of 24 simulations, demonstrate crystalline polyethylene chains oriented towards (30°/$[1\bar{1}00]$, 90°/$[\bar{1}010]$, and 150°/$[01\bar{1}0]$). Figure 3.4 illustrates the frequency of observed crystallographic orientations showing orientation angles with the reference direction set at 0°/$[\bar{1}2\bar{1}0]$, for all 24 MD simulations. It is apparent that the guided assembly of polyethylene chains on $MoSe_2$ surface tends to favor the crystallization orientation (0°/$[\bar{1}2\bar{1}0]$, 60°/$[2\bar{1}\bar{1}0]$, 120°/$[\bar{1}\bar{1}20]$).

To analyze the difference between two interfacial crystallographic orientations, we closely examined how polymer chains align on the MoSe2 surface. Figure 3.5 illustrates the mutual interfacial crystallographic orientation in the directions $[2\bar{1}\bar{1}0]$ (a) and $[01\bar{1}0]$ (b). In Figure 3.5, the polyethylene chains are numbered, while the Se lines and mixed Mo/Se lines are labeled to illustrate the positioning of polymer chains on the MoSe2 surface. Note that in Figure 3.5, selenium (green) atoms are depicted on top, molybdenum (red) atoms are in the middle, and bottom selenium (green) atoms are obscured due to overlap from the top selenium atoms. Carbon atoms are represented in purple, and hydrogen atoms are omitted for clarity. In Figure 3.5 (a), for the interfacial crystallographic orientation (0°/$[\bar{1}2\bar{1}0]$, 60°/$[2\bar{1}\bar{1}0]$, 120°/$[\bar{1}\bar{1}20]$), alternate polyethylene chains 2, 4, and 6 reside in the Se valleys, while chains 1, 3, and 5 lie atop Se lines. In contrast, for orientations 30°/$[1\bar{1}00]$, 90°/$[\bar{1}010]$, and 150°/$[01\bar{1}0]$, polyethylene chains tend to align within the narrow valleys of mixed Mo/Se lines, as depicted in Figure 3.5 (b). Further investigation into epitaxial lattice matching along the contact plane in the hybrid polyethylene/$MoSe_2$ system aimed to understand the preference of interfacial crystallographic orientations. Epitaxy typically entails order in the relative orientation of identical crystals

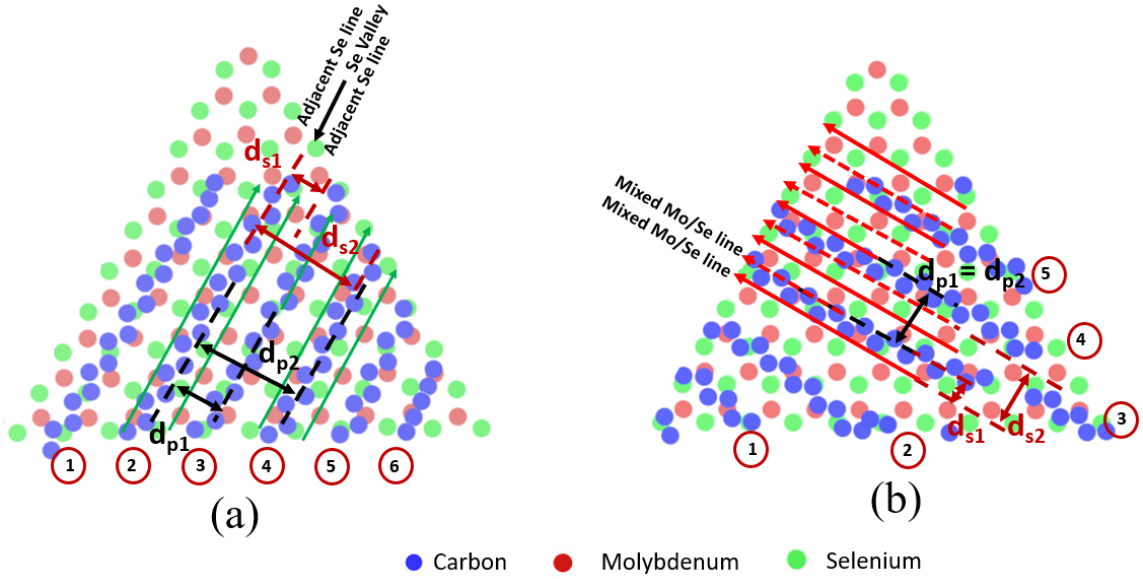

Figure 3.5: (a) Illustrates the crystallization of polyethylene on the $MoSe_2$ surface with a 60 degrees/$[2\bar{1}\bar{1}0]$ orientation. Domain epitaxial matching between polyethylene chains and the $MoSe_2$ surface is evident as polyethylene chains number 2, 4, and 6 (highlighted in red circles) align themselves in Se valleys, meaning every alternate polyethylene chain is positioned between two adjacent Se lines (b) Depicts the crystallization of polyethylene on the $MoSe_2$ surface with a 150 degrees/$[01\bar{1}0]$ orientation. Domain epitaxial matching between polyethylene chains and the $MoSe_2$ surface is observed as polyethylene chains number 3, 4, and 5 (highlighted in red circles) are positioned between alternate mixed Mo/Se lines, leaving one mixed Mo/Se line between two crystallized polyethylene chains

nucleated and grown on a large single-crystal seed surface, where the deposited crystalline film is termed an epitaxial film or layer. This study is a case of heteroepitaxy where the crystalline seed is 2D $MoSe_2$, while the crystal film/layer is polyethylene, with the mutual orientations along the contact plane defined as (0001) for $MoSe_2$ and (100) for polyethylene. The interfacial orientation relationship is largely determined by the intralayer strain energy or lattice misfit along the interface, defined as $\Delta = 100(d_p - d_s)/d_s$ [83], where d_p and d_s are the lattice parameters of polyethylene and $MoSe_2$, respectively. According to Wittmann and Lotz [84], $\Delta < \pm 15\%$ is an acceptable range of lattice mismatch for continuous epitaxial growth. For the orientation ($0°/[\bar{1}2\bar{1}0]$, $60°/[2\bar{1}\bar{1}0]$, $120°/[\bar{1}\bar{1}20]$), with $d_{s1} = 0.332 \cos 30°$ nm and $d_{p1} = 0.4837$ nm, the lattice mismatch is 68.24%, suggesting a large mismatch. However, domain epitaxial growth is observed, where every alternate polyethylene chain lies between two adjacent Se lines (Se valleys), resulting in a minimized intralayer strain and small domain lattice-mismatch strain. A region of the substrate with a size of nd_{s1} is aligned with md_{p1} of the epilayer, resulting in a slight residual domain mismatch strain. In Figure 3.5 (a), it can be observed that every second polyethylene chain lies between two neighboring Se lines (Se valleys), while the remaining chains overlap the Se lines. This configuration corresponds to n=3 and m=2, leading to $d_{p2} = 2d_{p1}$ and $d_{s2} = 3d_{s1}$. The domain lattice-mismatch, calculated using d_{p2} and d_{s2}, is 12.1%, indicating a minor domain lattice-mismatch strain. Similarly, for the orientation $30°/[1\bar{1}00]$, $90°/[\bar{1}010]$, and $150°/[01\bar{1}0]$, the lattice mismatch is estimated to be 183.7%, suggesting unfavorable growth. For the domain lattice-mismatch, this configuration results in n=1 and m=3, leading to $d_{p2} = d_{p1}$ and $d_{s2} = 3d_{s1}$. The domain lattice-mismatch calculated using d_{p2} and d_{s2} is -8.1%. This minimizes intralayer strain within the epilayer, thereby facilitating epitaxial growth in orientations such as $30°/[1\bar{1}00]$, $90°/[\bar{1}010]$, and $150°/[01\bar{1}0]$. Hence, it can be inferred that in systems with significant lattice mismatch, such as the hybrid polyethylene/$MoSe_2$ system studied here, the epitaxial orientation relationship is governed by domain epitaxial growth, resulting in a substantial reduction in energy from the fully coherent state.

Another crucial aspect influencing epitaxial growth alongside lattice misfit is the density of coincident atom sites at the interface, which correlates with the steric hindrance among atoms along the $MoSe_2$-polyethylene interface. Notably, the primary steric hindrance arises from the interaction between selenium atoms in the top layer of 2D $MoSe_2$ and carbon atoms in the polyethylene chains. Examining the atomic arrangements along the interface in the two interfacial crystallographic orientations, Figure 3.6 showcases detailed images of one polyethylene chain. In orientation $0°/[\bar{1}2\bar{1}0]$, $60°/[2\bar{1}\bar{1}0]$, $120°/[\bar{1}\bar{1}20]$, carbon atoms within chains 2, 4, and 6 encounter minimal steric hindrance from selenium atoms as they are positioned between two Se lines. Similarly, in orientations $30°/[1\bar{1}00]$, $90°/[\bar{1}010]$, and $150°/[01\bar{1}0]$, all carbon atoms experience steric hindrance with the top selenium atoms. The observed interfacial cohesive energy for orientations $0°/[\bar{1}2\bar{1}0]$, $60°/[2\bar{1}\bar{1}0]$, $120°/[\bar{1}\bar{1}20]$ is notably lower compared to $30°/[1\bar{1}00]$, $90°/[\bar{1}010]$, $150°/[01\bar{1}0]$. Through MD simulations, the interfacial cohesive energy for orientations $0°/60°/120°$ is estimated to be 5.32 ± 1.81 eV lower on average than that for orientations $30°/90°/150°$. Thus, it can be inferred that crystallographic orientations ($0°/[\bar{1}2\bar{1}0]$, $60°/[2\bar{1}\bar{1}0]$, $120°/[\bar{1}\bar{1}20]$) are more favorable for epitaxial growth than orientations ($30°/[1\bar{1}00]$, $90°/[\bar{1}010]$, $150°/[01\bar{1}0]$). This observation aligns with the higher frequency (58.3%) of occurrences of orientations ($0°/[\bar{1}2\bar{1}0]$, $60°/[2\bar{1}\bar{1}0]$, $120°/[\bar{1}\bar{1}20]$) among the 24 simulations conducted, as indicated in Table 3.1 and Figure 3.4.

3.3.1 Experimental Characterization

The crystallization process of polyethylene on the $MoSe_2$ surface was also explored using experiments. To get truncated triangles of 2D $MoSe_2$ with selenium edges, a chemical vapor deposition (CVD) method was

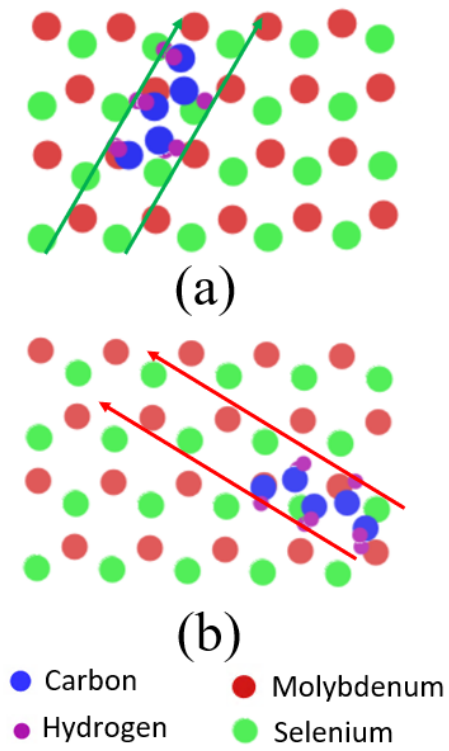

Figure 3.6: (a) Depicts the positioning of carbon and hydrogen atoms on the $MoSe_2$ surface during crystallization at 60 degrees/$[2\bar{1}\bar{1}0]$. One can observe that carbon atoms are situated between the vacancies of adjacent Mo/Se lines (b) Illustrates the arrangement of carbon and hydrogen atoms on the $MoSe_2$ surface during crystallization at 150 degrees/$[01\bar{1}0]$. Here, carbon atoms are observed to settle atop the vacancy of the mixed Mo/Se line, marked by the imaginary line between the two red arrows

used. This involved growing of 2D $MoSe_2$ at 760°C for 10 minutes using CVD in a quartz tube. A silicon substrate with a 285-nm thick top SiO_2 layer supported the weight of 2D $MoSe_2$ layer. The process began with a silicon substrate facing downward, with one ceramic boat containing 15 mg of molybdenum oxide powder (MoO_3) and another boat containing 700 mg of selenium powder placed upstream in the quartz tube. The selenium crucible and molybdenum oxide were positioned 18 cm apart. The temperature was ramped up to 1033 K at a rate of 50 K/min for 10 minutes, followed by rapid cooling. To obtain truncated triangles of 2D $MoSe_2$ with selenium edges, one side of the MoO_3 crucible was removed, and the MoO_3 was placed upstream, promoting an enriched Se environment with low MoO_3 concentration conducive to forming truncated triangles or triangles with Selenium edges/0°/$[\bar{1}2\bar{1}0]$. High-density polyethylene (Sigma-Aldrich, MFI 12 g/10 min) was dissolved in p-xylene (0.1 mg/mL) at 403 K with continuous stirring for 30 minutes. The solution was then transferred to an oil bath maintained at a fixed crystallization temperature of 373 K for 30 minutes. A preheated $MoSe_2$ in pure xylene solution at 373 K was swiftly combined with the polymer/xylene at 373 K for the crystallization process. After 30 minutes of crystallization, the sample was removed and rinsed immediately with xylene at 373 K, followed by drying with nitrogen gas. The scanning electron microscope image in Figure 3.7 illustrates crystallized polyethylene lamellas on the $MoSe_2$ surface. A magnified schematic shows two polyethylene lamellas with crystallized polyethylene chains perpendicular to

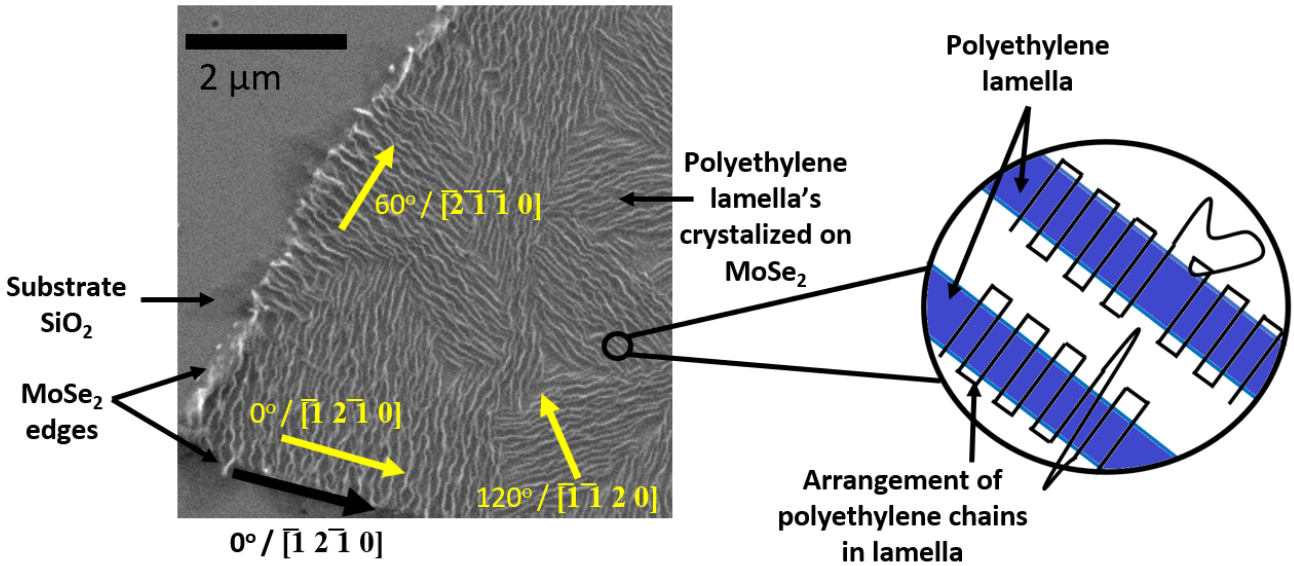

Figure 3.7: The scanning electron microscope (SEM) image depicts crystallized polyethylene lamellas on the surface of $MoSe_2$. In the image, only three crystallization orientations (0°/60°/120°) of polyethylene are observable relative to the 0°/[$\bar{1}2\bar{1}0$] reference line marked in black on the $MoSe_2$ surface. A closer view of a polyethylene lamella reveals that the axis of the polyethylene chains is perpendicular to the axis of the crystallized polyethylene lamella

the lamella orientation. The image highlights polyethylene chains crystallized at 0°/[$\bar{1}2\bar{1}0$], 60°/[$2\bar{1}\bar{1}0$], and 120°/[$\bar{1}\bar{1}20$] (indicated by green arrows) relative to the 0°/[$\bar{1}2\bar{1}0$] reference line (depicted by black arrows) on the $MoSe_2$ surface. The image reveals multiple domains of aligned polyethylene lamellas, indicating a preference for crystallization orientations in 0°/[$\bar{1}2\bar{1}0$], 60°/[$2\bar{1}\bar{1}0$], and 120°/[$\bar{1}\bar{1}20$]. Notably, no crystallized polyethylene orientations were observed in the 30°/[$1\bar{1}00$], 90°/[$\bar{1}010$], and 150°/[$01\bar{1}0$] directions. This suggests that polyethylene preferentially crystallizes on the $MoSe_2$ surface following selenium valleys through specific manufacturing processes. While this example indicates crystallization of polyethylene in 0°/[$\bar{1}2\bar{1}0$], 60°/[$2\bar{1}\bar{1}0$], and 120°/[$\bar{1}\bar{1}20$] orientations together on the $MoSe_2$ surface, further investigations are needed to induce polyethylene crystallization in only one specific orientation on the $MoSe_2$ surface, potentially by straining the 2D $MoSe_2$ surface and introducing asymmetry to the crystallization directions, allowing one selenium valley to become more conducive to crystallization.

3.3.2 Effect of interfacial confinement on polymer assembly

This study investigated how local geometric confinement affects the assembly and crystallization behavior of polyethylene chains on $MoSe_2$ surface by analyzing the separation distance at the interface between polyethylene and $MoSe_2$. This separation distance was determined as the average distance between carbon and selenium atoms at the top layer along the interface for two distinct crystallization orientations, depicted in Figure 3.8. In both cases, the separation distance decreased from the initial value of 4.72 Å during the polymer assembly process and eventually stabilized around 4.35 Å for the 0°/60°/120° orientations, and 4.54 Å for 30°/90°/150°. This reduction in separation distance is attributed to the geometric interface confinement imposed by $MoSe_2$ on the surrounding polymer chains, which significantly influences the

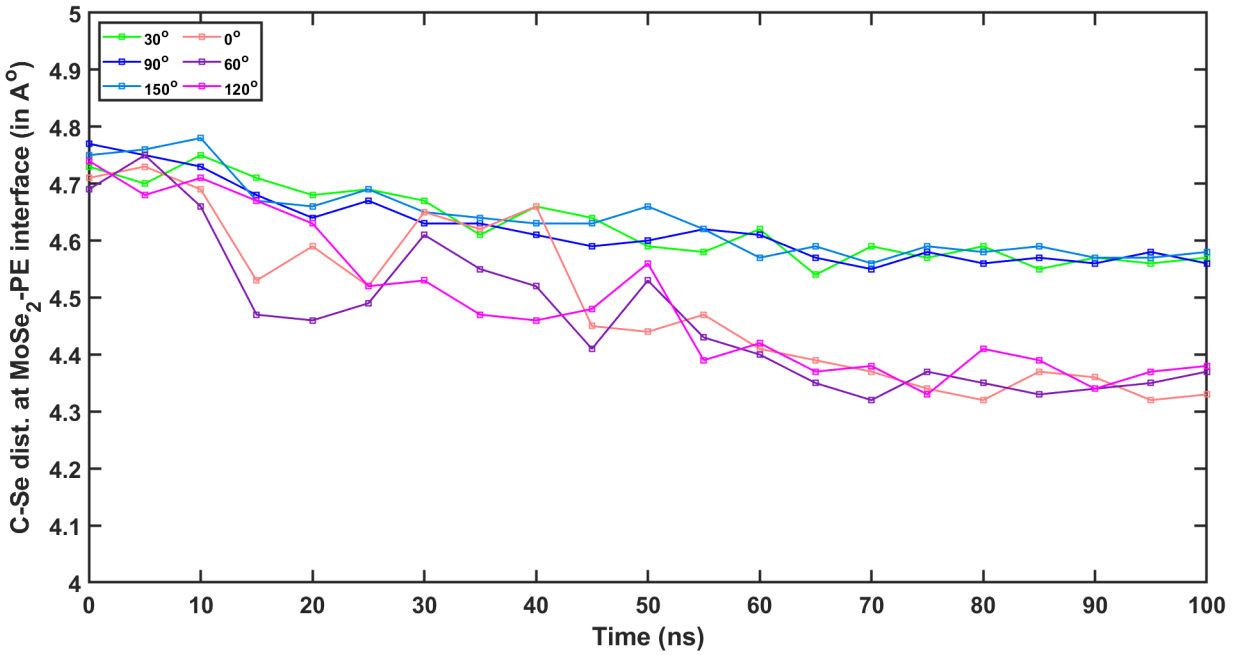

Figure 3.8: Average distance between carbon atoms of polyethylene at the interface and selenium atoms at the top of the interface over 100 ns at 360 K is plotted. Throughout the simulation, it is evident that the interfacial distance decreased over time for all crystallization orientations. Specifically, for crystallization orientations at 0°/60°/120°, the average interfacial distance reached 4.35 Angstrom at the end of 100 ns. Conversely, for crystallization at 30°/90°/150°, the average interfacial distance at the end of 100 ns measured 4.54 Angstrom

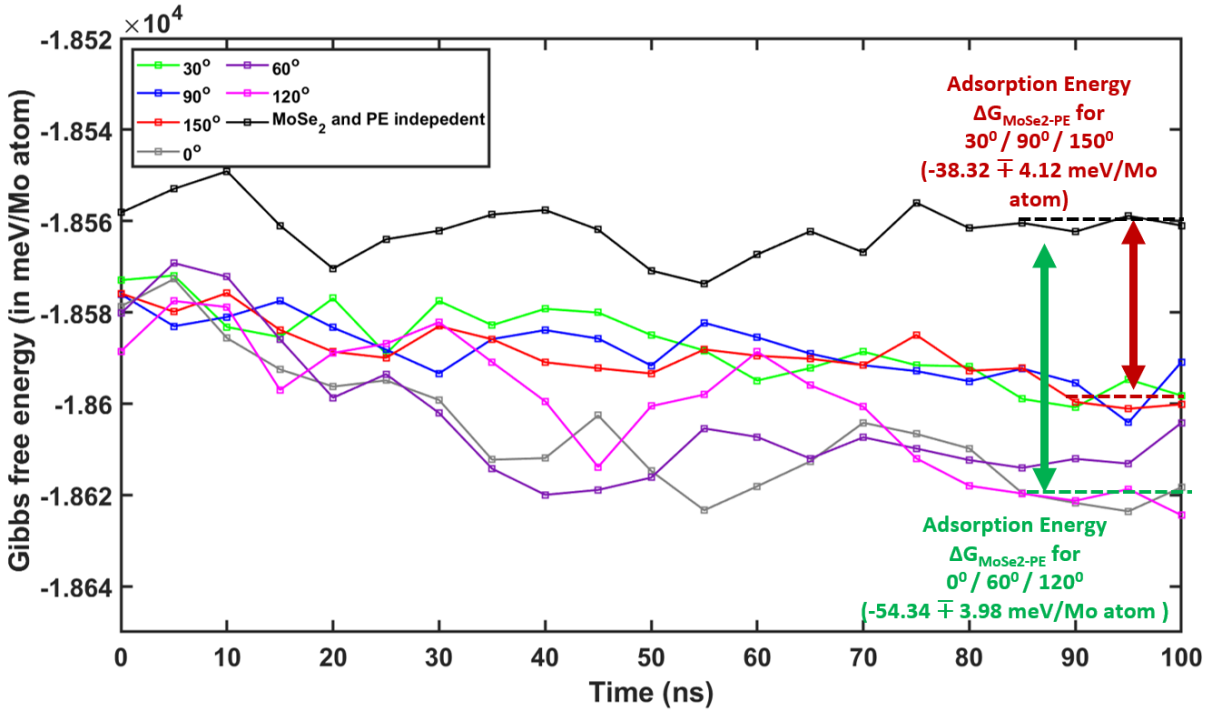

Figure 3.9: The Gibbs free energy of polyethylene on the $MoSe_2$ surface was analyzed over 100 ns during NPT simulations at 360 K. Black line represents the Gibbs free energy of the polyethylene-$MoSe_2$ system when they are sufficiently far apart. The adsorption energy is determined as the difference between the Gibbs free energy of the polyethylene-$MoSe_2$ system and the sum of the individual Gibbs free energies of polyethylene and $MoSe_2$. For crystallization at 0°/60°/120° orientations, the average adsorption energy at 100 ns was found to be -54.34 ± 3.98 meV/Mo atom. In contrast, for crystallization at 30°/90°/150° orientations, the average adsorption energy at 100 ns was -38.32 ± 4.12 meV/Mo atom.

arrangement and orientation of polyethylene chains during crystallization. Particularly for the 0°/60°/120° crystallization orientation, there was a more pronounced decrease in separation distance, suggesting a relatively stronger interface confinement. This enhanced confinement likely facilitates the formation of these specific crystallographic orientations 0°/60°/120°.

3.3.3 Adsorption energy between polyethylene and $MoSe_2$

In this study, the change in Gibbs free energy (ΔG) is utilized to assess the adsorption energy of polyethylene on $MoSe_2$ surface, defined by equation:

$$\Delta G = \Delta U - T\Delta S$$

Here, ΔG denotes the change in Gibbs free energy, ΔU represents the change in internal energy, T is the temperature of the simulation in Kelvin, and ΔS indicates the change in entropy. When polyethylene chains adhere to the $MoSe_2$ surface, the Gibbs free energy changes through two components: first through the total internal energy of the system (ΔU) and second through the change in system's entropy (TΔS). As the polyethylene chains become adsorbed on the $MoSe_2$ surface, the internal energy of the system decreases as well as it is accompanied by a reduction in the randomness of the polyethylene chains (decrease in entropy), leading to a decrease in Gibbs free energy. The Free Energy Perturbation method in LAMMPS is commonly

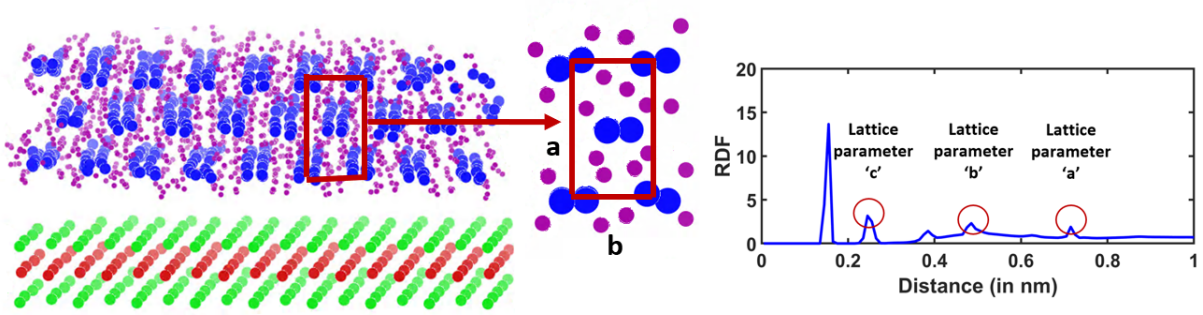

Figure 3.10: The crystallized polyethylene chains exhibit an orthorhombic unit cell structure, depicted in the left figure. To enhance clarity, an enlarged schematic of the orthorhombic unit cell structure of the crystallized polyethylene chains is presented in the middle. The right figure illustrates the radial distribution function for the lattice parameters a, b, and c (in nm) of the crystallized polyethylene

used to evaluate the change in Gibbs free energy of different systems which was used to evaluate Gibbs free energy in this study. The adsorption energy (ΔG_{ads}) of the current system can thus be calculated as the energy difference between the change in Gibbs free energy of the polyethylene-$MoSe_2$ system and the sum of changes in individual Gibbs free energies of polyethylene and $MoSe_2$.

$$\Delta G_{\text{ads}} = \Delta G_{\text{polyethylene-MoSe}_2} - (\Delta G_{\text{polyethylene}} + \Delta G_{\text{MoSe}_2})$$

The symbols $\Delta G_{\text{polyethylene-MoSe}_2}$, $\Delta G_{\text{polyethylene}}$, and ΔG_{MoSe_2} denote the changes in Gibbs free energy for the polyethylene-$MoSe_2$ system, polyethylene alone, and $MoSe_2$ surface, respectively. The quantity ΔG_{ads} provides a measure of the strength of interaction between polyethylene and $MoSe_2$. In molecular dynamics (MD) simulations, ΔG_{ads} is computed by averaging over various configurations or snapshots obtained from the simulation trajectory. This adsorption energy serves to elucidate the thermodynamics of adsorption, determining whether it is favorable (negative ΔG_{ads}) or unfavorable (positive ΔG_{ads}). For the two identified interfacial crystallographic orientations, we analyzed the Gibbs free energy profiles over 100 ns and calculated the adsorption energy, as shown in figure 3.9. To normalize the results, we divided the adsorption energy by the total number of Molybdenum (Mo) atoms in our system, yielding the change in adsorption energy per unit Mo atom. Notably, the adsorption energy for the 0°/60°/120° crystallization orientation (Adsorption energy -54.34 ± 3.98 meV/Mo atom) is lower than that of the 30°/90°/150° crystallization orientation (Adsorption energy -38.32 ± 4.12 meV/Mo atom). Negative adsorption energy values for both orientations imply stable adsorption and crystallization configurations. The magnitude of the adsorption energy reflects the strength of interaction between the polymer chains and the $MoSe_2$ surface. A higher adsorption energy indicates a stronger binding affinity between the polymer and the substrate. Therefore, it suggests that the 0°/60°/120° crystallization orientation is more stable/favorable than the 30°/90°/150° crystallization orientation.

3.3.4 Prefreezing of polyethylene chains on $MoSe_2$ at elevated temperature

The Figure 3.11 illustrates the radial distribution function (RDF) showing the crystallization behavior of carbon atoms in polyethylene chains in the presence of $MoSe_2$ surface at two different temperature conditions. Two curves are presented: the green curve represents a temperature of 360 K, below the melting point, while the blue curve corresponds to 500 K, above the melting point. In the green curve obtained at 360 K for crystallization at 0°/60°/120°, a distinct first peak is observed at approximately 4.35 Angstroms. The

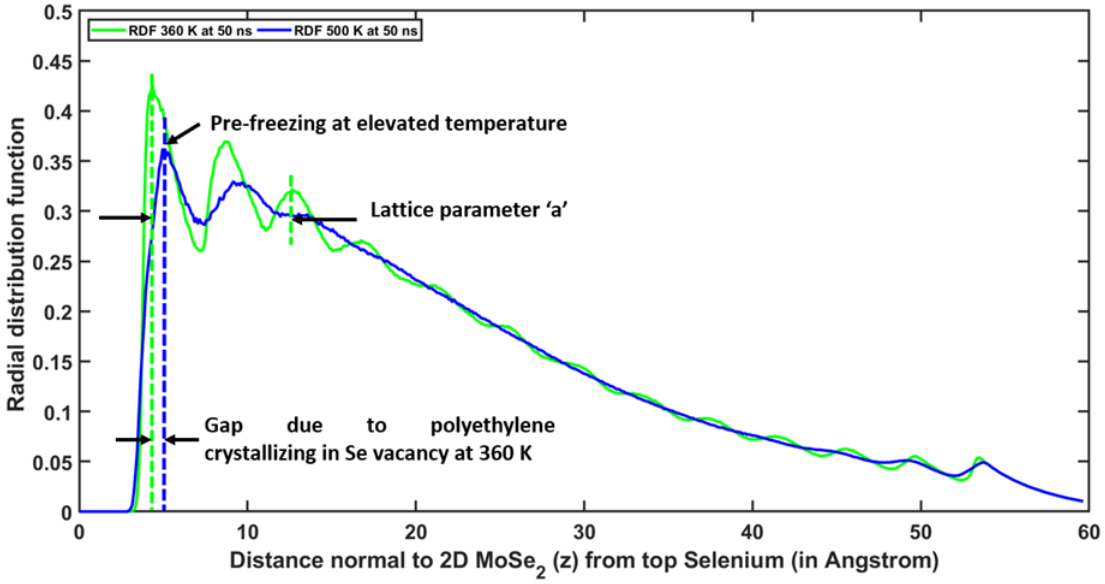

Figure 3.11: Radial distribution function to understand the prefreezing of polyethylene chains on 2D $MoSe_2$ surface below and above melting temperature

spacing between alternate peaks corresponds to the lattice parameter of polyethylene when it crystallizes into orthorhombic unit cells. Additionally, peaks emerge towards the end of the simulation box, indicating polyethylene crystallization from the second interface due to periodic boundary conditions. In contrast, the blue curve at 500 K shows a first peak around 4.54 Angstroms. A second peak suggests that some carbon atoms have crystallized due to the $MoSe_2$ surface even at 500 K. The positioning of the first peak at 4.54 Angstroms in the blue curve implies randomly oriented polyethylene chains not crystallized within the Selenium valleys. The RDF value for the blue curve is approximately 15% lower than the peak in the green curve, indicating either incomplete crystallization or reduced mobility of some atoms at 500 K. This indicates that the $MoSe_2$ surface can induce pre-freezing in polyethylene, serving as nucleation initiation sites upon cooling. The presence of pre-frozen regions above the melting temperature suggests the importance of interfacial effects in influencing crystallization of polyethylene chains on $MoSe_2$ surface.

3.3.5 Crystalline structure of the interphase region

Table 3.2: The lattice parameters of crystallized polyethylene is examined for two different crystallization orientations. Case 1 corresponds to crystallization of polyethylne at (0°/[$\bar{1}$ 2 $\bar{1}$ 0], 60°/[2 $\bar{1}$ $\bar{1}$ 0], 120°/[$\bar{1}$ $\bar{1}$ 2 0]), while Case 2 represents crystallization at (30°/[1 $\bar{1}$ 0 0], 90°/[$\bar{1}$ 0 1 0], 150°/[0 1 $\bar{1}$ 0]). The outcomes display the average values of lattice parameters derived from 24 MD simulations and compare them with experimental investigations. Note that all dimensions are presented here are in nanometers

LP	Expt.[85]	Case 1	Case 2
a	0.7121	0.7284 ±0.012	0.7263 ±0.014
b	0.4821	0.4837 ±0.057	0.4709 ±0.122
c	0.2548	0.2554 ±0.003	0.2536 ±0.004

The crystal structure of polyethylene was initially characterized by Bunn et al. [86], indicating that

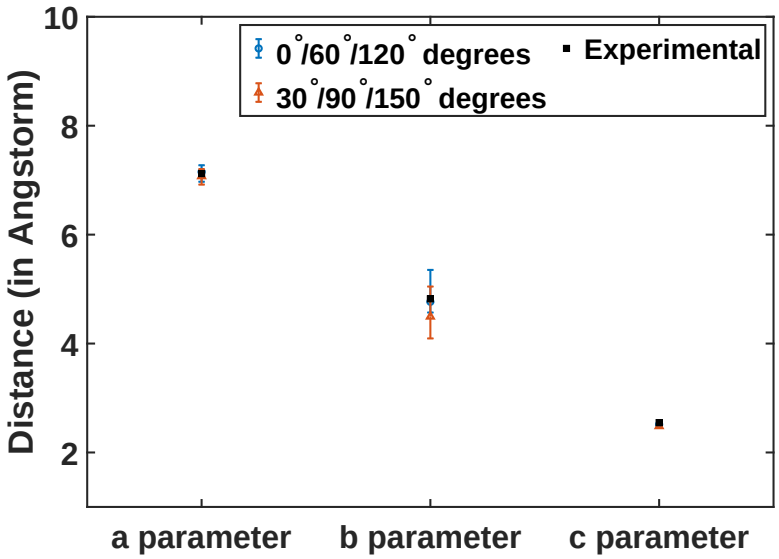

Figure 3.12: The evaluation of lattice parameters a, b, and c for two crystallization orientations is shown: 0°/60°/120°, representing crystallization of polyethylene in Se valleys (shown in blue color), and 30°/90°/150°, representing crystallization of polyethylene in between mixed Mo/Se lines (shown in orange color). These parameters are also compared with experimental findings from Alsaygh et al. [85]. It is worth noting that there is no significant deviation observed in the in-chain lattice parameter c and the out-of-plane lattice parameter a for both cases. However, high deviation is observed in the inter-chain lattice parameter b for crystallization of polyethylene in between mixed Mo/Se lines compared to crystallization of polyethylene chains in between Se valleys

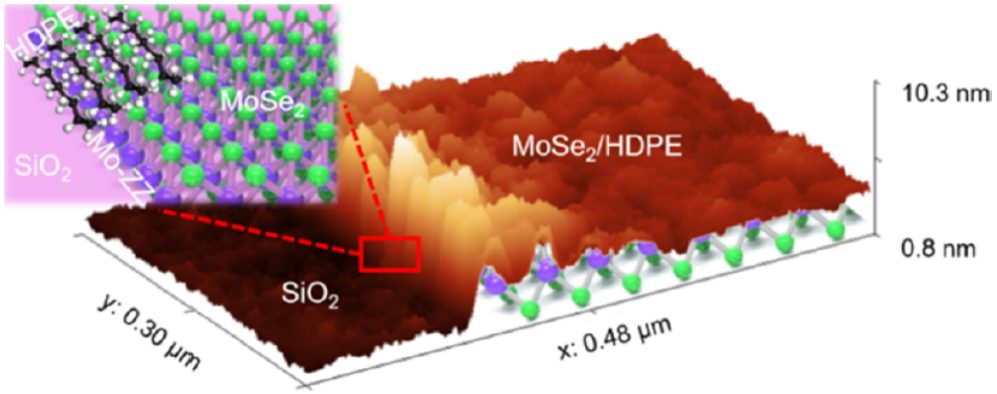

Figure 3.13: Edge guided crystallization of polyethylene chains on $MoSe_2$ surface. Note, $MoSe_2$ is adsorbed on SiO_2 surface in the image shown

polyethylene crystallizes into orthorhombic unit cells, which is considered as the most stable crystal structure of crystallized polyethylene below its melting point. Under specific mechanical loading conditions, polyethylene can also adopt a monoclinic crystal structure as suggested by Olsson et al. [87]. Detailed atomic structure of crystalline polyethylene on a 2D $MoSe_2$ sheet, with orthorhombic crystal structure, is shown in Figure 3.10. The radial distribution function of carbon atoms confirms the orthorhombic lattice parameter of crystallized polyethylene. In the radial distribution function plot, the first peak represents adjacent carbon atoms within the same polyethylene chain, followed by peaks corresponding to lattice parameters c, a, and b. The crystalline polyethylene structures are further characterized in terms of unit cell parameters using the crystallinity parameter p_2 of carbon atoms. Experimental data from Alsaygh et al. [85] reveal that the orthorhombic unit cell of polyethylene has parameters $a = 0.7407$ nm, $b = 0.49491$ nm, and $c = 0.25511$ nm, where lattice parameter c is along the chain axis. Two different types of interfacial crystallographic orientations were identified, displaying different registrations with the $MoSe_2$ substrate, denoted by the Miller-Bravais direction indices: first case ($0°$ /$[\bar{1}2\bar{1}0]$, $60°/[2\bar{1}\bar{1}0]$, $120°/[\bar{1}\bar{1}20]$) and second case ($30°/[1\bar{1}00]$, $90°/[\bar{1}010]$, $150°/[01\bar{1}0]$). For these two cases with different interfacial crystallographic orientations of polyethylene chains on $MoSe_2$ surface, the lattice parameters of crystallized polyethylene chains were evaluated and compared to experimental results of Alsaygh et al. [85]. In both cases, the mean values of the estimated lattice parameter a and c align well with the experimental values. However, for the mean value of lattice parameter b, the former crystallographic orientation ($0°$ /$[\bar{1}2\bar{1}0]$, $60°/[2\bar{1}\bar{1}0]$, $120°/[\bar{1}\bar{1}20]$) matches the reported experimental value, while the latter case ($30°/[1\bar{1}00]$, $90°/[\bar{1}010]$, $150°/[01\bar{1}0]$) exhibits a slightly smaller value, deviating from the experimental results of Alsaygh et al. [85]. Lattice parameter a represents the inter-layer lattice parameter, b indicates the inter-chain lattice parameter in different planes/layers of crystallization, and c signifies the intra-chain lattice parameter within the same plane. It's noteworthy that the inter-chain distance (i.e., b value) in different planes/layers varies in cases with different interfacial crystallographic orientations, while the intra-chain and inter-layer lattice parameters remain consistent. The lower mean value of lattice parameter b observed in the second set of crystallization orientations ($30°/[1\bar{1}00]$, $90°/[\bar{1}010]$, $150°/[01\bar{1}0]$) suggests higher steric hindrance between carbon and selenium atoms at the interface might be leading to lower mean value of lattice parameter b with a higher standard deviation. This implies that interface-induced epitaxial crystallization can potentially modify the crystalline polymer structure in the interphase region through interfacial registration.

3.4 Edge guided crystallization of polyethylene on $MoSe_2$ surface

2D $MoSe_2$ helps crystallize polyethylene along its well-defined atomic edge configurations. In this section experimental, ab-initio and atomistic MD simulations are used to study how atomic edges interact with polyethylene (PE) chains in a dilute solution of 2D $MoSe_2$ and polyethylene and understand the assembly process [3] of polyethylene chains on 2D $MoSe_2$. Our results reveal that Mo-terminated zigzag (Mo-ZZ) edges act as preferred nucleation sites and strongly interact with PE chains as shown in Figure 3.13. The PE chains align in parallel with the Mo-ZZ edges and form arrays of lamellae that are perpendicular to the edges. Atomic edge configurations are dramatically change the crystallization orientations of PE on $MoSe_2$ surface. In experimental setup we observed different crystallization orientations on different edges using a same piece of $MoSe_2$ with had different types of edges. To validate and get deeper understanding we conducted ab initio and MD simulations using n - alkane (n = 5 and 25 carbon atoms segment of PE) and $MoSe_2$ using Mo-ZZ edge atomic structures of $MoSe_2$ and studied the edge effects on crystallization orientation in n -alkane/polyethylene chains. In these computational studies, Mo-ZZ edge was preferred nucleation initiation site where long range alignment of PE lamellae/chains can be realized by creating multiple layer of $MoSe_2$ with parallel atomic steps. This study opens up a new dimension in atomic level crystallization of polymers using 2D nanomaterial. This study also bridges the gap between atomic-level nanocomposites and describes their long-range mesoscopic structures. This also introduces a new mechanism (edge induced crystallization) for creating long-range structural order in semi crystalline polymers such as polyethylene.

3.4.1 Experimental edge guided crystallization of PE on $MoSe_2$ surface

In this subsection we analyze the Mo-ZZ and Se-ZZ edges based specific crystallization of polyethylene in MoSe2-PE nanocomposite via chemical vapor deposition (CVD). Firstly, we need to create planar MoSe2 with specific edges. The edge termination of 2D MoSe2 can be influenced by the precursor ratio/distribution which is controlled by the flow field and precursor-substrate distance during the CVD process. MoSe2 exhibits stability under ambient conditions with organic solvents at elevated temperatures, making it a controllable material for studying interactions with polymer chains. Polyethylene (PE) is chosen as a polymer material because of its simple chain structure which enables clear observation of interactions with atomic structure of MoSe2. For MoSe2-PE nanocomposites a diluted solution, at an elevated temperature, creates a controlled environment which helps heterogeneous nucleation and lamella growth processes. This helps in investigation of interactions between individual MoSe2 edges and PE chains. Figure 3.13 (a) illustrates the crystallization process and the resultant structure of MoSe2-PE nanocomposite. Single-crystal monolayer to multilayer MoSe2, with triangular morphology, is grown on a SiO2/Si substrate with a 280 nm thick thermal oxide layer used using CVD growth process. Figure 3.13 (b) displays a typical optical image of a monolayer/single layer MoSe2 on a SiO2/Si substrate. Characterization techniques like scanning transmission electron microscopy (STEM), Raman, and photoluminescence (PL) spectra were used to confirm the monolayer quality in triangle domains. Amorphous SiO2 surface does not actively interact with PE chains, providing a clear background for observing MoSe2 edge-induced PE crystallization. Crystallization results at 90°C for 30 minutes demonstrate that $MoSe_2$ edges not only serve as preferred nucleation sites but also guide lamellae growth. Polymer chains align parallel to the MoSe2 edge, facilitating perpendicular lamellae growth, as shown in Figure 3.13 (b,c and d). These lamellae exhibit parallel alignment with an average periodicity of 166 ± 100 nm and a length of 223 ± 83 nm. The length of these lamellae, defined as the correlation distance, indicates a range affected by edge guided crystallization of PE. The guiding effect of edge is further evident at the step between the first layer

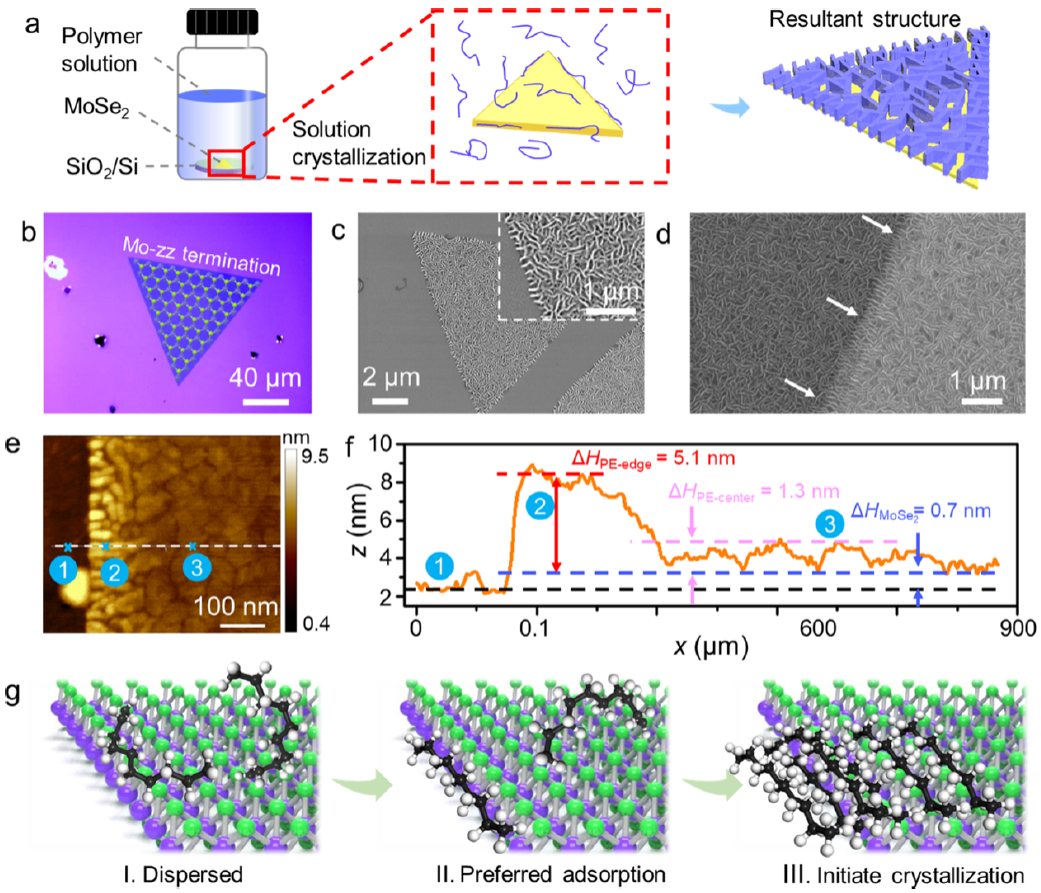

Figure 3.14: Experimental results for preferential edge crystallisation of PE (a) Schematic of solution crystallization process and the resultant hybrid structure. (b) Optical image of a single crystal monolayer of $MoSe_2$ with Mo-ZZ termination edges on SiO_2/Si substrate. (c) SEM image showing the PE crystallization on monolayer $MoSe_2$ surface. The inset shows the enlarged view. (d) SEM image shows the PE crystallization on monolayer $MoSe_2$ and bilayer $MoSe_2$ surface. (e) AFM image of PE crystallization under 100 °C for 5 min (f) The height profile, in panel (e) along the white dashed line is indicated in panel (g) Schematic showing the process of the edge-initiated crystallization process

and the second layer of a multilayer MoSe2, where aligned lamellae were observed. Nucleation of PE chains on the MoSe2 edge leads to lamella growth in two directions: inward toward the MoSe2 and outward toward the bare SiO2 surface. Outward growth from the edge terminates approximately at 58 ± 10 nm. Inward growth competes with basal plane-induced crystallization. As one moves toward the center of MoSe2, the influence of edge guided crystallization diminishes, leading to macroscopically random crystallization arrays on the basal plane. This aligns well with previous studies demonstrating PE chain epitaxial assembly on crystalline planes. However, previous studies focused on bulk crystal assemblies and did not clearly explained the edge-induced crystallization in semi-crystalline polymers. Thus, 2D MoSe2 is one of the few special materials that elucidate edge-preferred crystallization phenomena in polyethylene chains.

The basal plane's also has the potential to initiate nucleation and lamellae growth. This raises a critical question that whether the MoSe2 edge is genuinely the preferred site for PE nucleation and crystallization or not. Thus, to capture the initial crystallization stage, we increased the crystallization temperature to 100°C and reduced the assembly time to 5 minutes. Using the atomic force microscope (AFM), we examined the morphology, as shown in Figure 3.13 (e), near the edge of a 2D $MoSe_2$ (0.7 nm thick). The line profile, as shown in Figure 3.13 (f), indicates that the lamella's height at the edge is 5.1 nm. Conversely, on the basal plane, the AFM image displays ultrathin, irregular-shaped patches of adsorbed PE (0-1.3 nm) with cracks among them, suggesting a very early stage of polymer crystallization. Our experiment suggests that Mo-ZZ edges are indeed preferred sites for nucleation as crystallization initiates at the MoSe2 edge whereas at basal plane the crystallization has still not started. Based on our experimental observations, we propose a Mo-ZZ edge-preferred crystallization mechanism (Figure 3.13 (f)). Initially, in a dilute polymer solution, PE chains exhibits conformational flexibility and are uniformly dispersed (I). When a PE chain encounters a hetero edge/surface, it can be adsorbed to the edges or the basal plane to reduce the Gibbs free energy. In the heterogeneous crystallization process, adsorption and orientation on the nuclei surfaces are believed to be essential steps in determining the crystallization rate. The orientation of PE lamellae (perpendicular to the edge) suggests that the Mo-ZZ edge of $MoSe_2$ is favorable for both adsorption and orientation processes (II). The orientation process of the PE segment concludes when it is absorbed onto an aligned Mo atoms line due to the possible geometric confinement effect. Adsorption and re-orientation of polyethylene chain occur simultaneously, forming stable and parallel to Mo-ZZ edge oriented PE chains. Finally, the orientation of the formed nuclei initiates the crystallization process, and lamellae grow perpendicular to the edge and propagate towards both directions, i.e., the basal plane and the bare SiO_2 (III). While crystallization on the basal plane is possible, it possibly has lower free energy change compared to $MoSe_2$ Mo-ZZ edge. The nucleating capability of PE chains on different atomic motifs is further examined using ab-initio and MD simulations in the following discussion.

3.4.2 Ab-initio simulations for edge guided crystallization of PE on $MoSe_2$ surface

Ab-initio simulations were also utilized to investigate the interaction between a PE segment, represented by a pentane molecule, and various atomic configurations of monolayer MoSe2 as shown in Figure 3.16. The simulation setup involved triclinic simulation box containing 200 Selenium and 100 Molybdenum atoms, representing a monolayer MoSe2, along with a pentane molecule comprising 5 Carbon and 12 Hydrogen atoms. The triclinic simulation box was periodic in the y-direction while it is presumed to be in vacuum from x and z directions. The pentane molecule was positioned in different orientations relative to the MoSe2 layer, including parallel and perpendicular to the Mo-ZZ and Se-ZZ edges, as well as atop the basal plane.

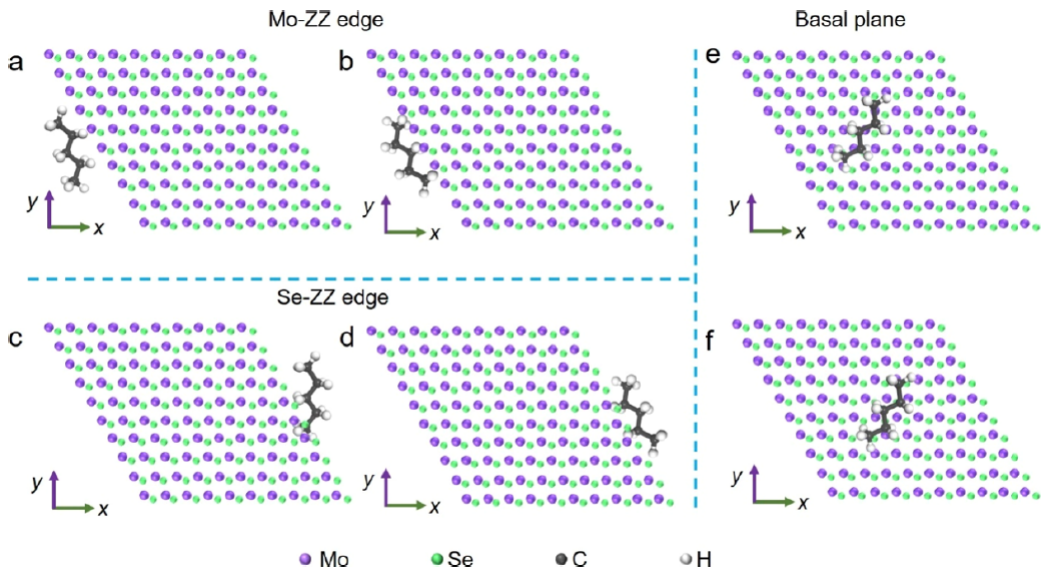

Figure 3.15: Results from ab-initio simulations support the preferential crystallization of PE at the edges. The interaction between a pentane molecule and $MoSe_2$ is depicted in the figures above

In the latter scenario, the pentane was placed above the Se atoms forming the peaks of the surface and the Mo atoms located in the valleys between these peaks. After relaxation, the final energy was computed to determine the binding energy, which quantifies the interaction between the polymer and MoSe2. The calculations used the VASP software, employing the Perdew-Burke-Ernzerhof (PBE) generalized gradient approximation (GGA) with the semiempirical DFT-D3 method, a 1×1×1 Monkhorst-Pack grid, and an energy cutoff of 400 eV. The results revealed that the binding energies to Mo sites, whether at the edges or the basal plane, were stronger compared to their Se site counterparts. Notably, the binding energy to the Mo-ZZ site exhibited a significantly higher value than other sites. This suggests a preference for PE to bind to the Mo-ZZ edges initially, followed by alignment with the Mo sites along the valleys of the basal plane as the polymer populates this plane. These findings support the concept of edge-guided crystallization, where the Mo-ZZ edge facilitates both the adsorption and orientation of PE chains, with a preferable orientation along the valleys of the basal plane. Additionally, on the basal plane, Mo valleys were identified as preferred sites for pentane absorption over Se peaks, indicating stronger interactions between PE molecules and Mo-ZZ edges.

3.4.3 MD simulations for edge guided crystallization of PE on $MoSe_2$ surface

MD simulations were also conducted to simulate the assembly process of PE on a monolayer $MoSe_2$. All-atom models were utilized to accurately represent all atoms in the PE-$MoSe_2$ system. To better capture the long-chain structure of PE molecules, the MD simulations involved 91 polymer chains, each containing 25 carbon atoms, as shown in Figure 3.16. These polymer chains were initially fully extended across 7 layers of 13 chains. Positioned adjacent to a monolayer of $MoSe_2$ comprising 360 atoms, the simulations applied periodic boundary conditions in the y- and z-directions, with vacuum added in the x-direction to expose the Mo-ZZ and Se-ZZ edges on each side. Using NPT ensemble with a pressure of 1 atm, the simulations starts with an equilibration phase at 500 K for 1 ns, above the melting temperature of PE, to achieve

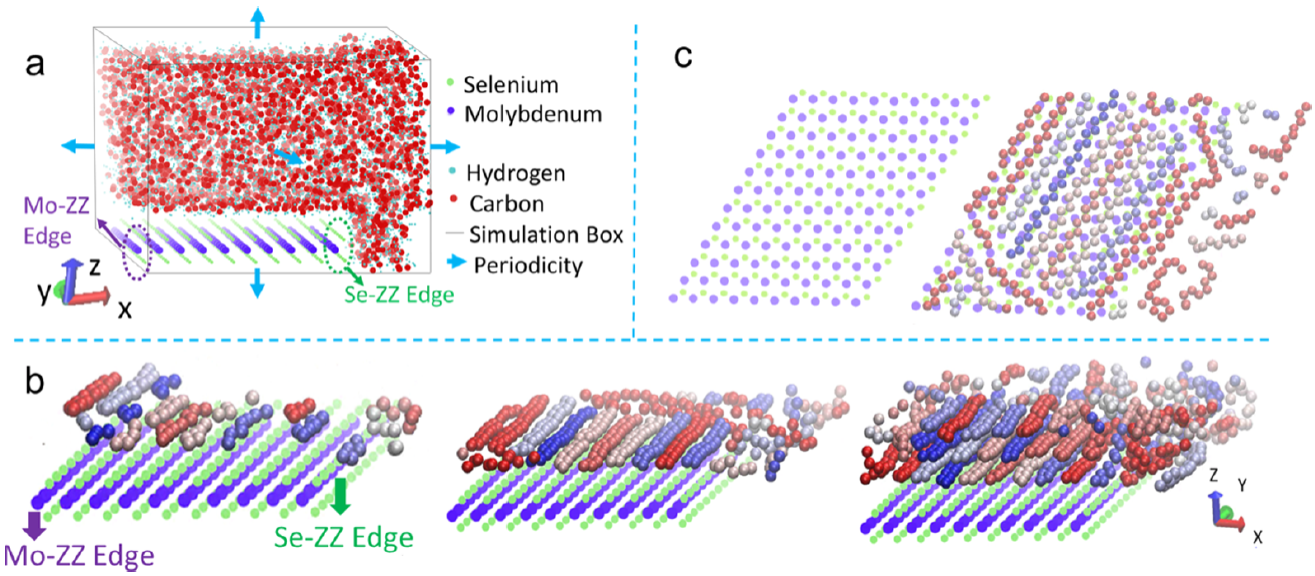

Figure 3.16: MD simulation results for the edge preferred crystallization of PE is shown as follows: (a) An all-atom MD simulation model is shown, featuring a coloring scheme for each atom type and periodic boundary conditions in all directions (b) The propagation of polymer chain crystallization is observed starting from the Mo-ZZ edge where each PE chain is represented using a distinct color to differentiate oriented chains (c) Surface atomic structure of the nucleating agent $MoSe_2$ is displayed on the left, alongside a snapshot illustrating the arrangement of polyethylene chains within the first layer on the surface of 2D $MoSe_2$ is shown on the right

a randomly mixed polymer chain configuration in the liquid phase. Subsequently, the temperature was quenched to the crystallization temperature of 360 K within 100 ps to start the crystallization process of PE chains. Crystallization initiation was observed at the surface of the $MoSe_2$ substrate, propagating through the z-direction perpendicular to the substrate surface, as shown in Figure 3.16 (b). The initial crystallization state revealed a higher density of oriented PE chains at the Mo-ZZ edge compared to the basal plane and the Se-ZZ edge, suggesting the Mo-ZZ edge's enhanced nucleation ability. With increasing crystallization time, layer-by-layer crystallization occurred, extending up to a maximum of 3 layers in the z-direction away from the $MoSe_2$ substrate surface. The alignment of crystallized chains at the $MoSe_2$ surface exhibited a registry with the underlying crystallographic planes, particularly overlaying with the Mo valleys on the basal planes due to their stronger interaction compared to the Se peaks. MD simulations supported the concept of an edge-guided crystallization mechanism, consistent with experimental findings and ab initio predictions. It's worth noting that n-alkanes (n = 5 and 25) may not fully represent PE's behavior, especially considering the conformational entropic effects of its long-chain structure. Extensive simulations utilizing coarse-grained polyethylene models are necessary to explore the interplay between chain adsorption, crystallization, and entropy, which is beyond the scope of the current study.

3.4.4 Edge type determined preferred crystallization

The ab-initio simulations suggest that the atomic arrangement of edges may influence their interaction with polymer chains, given the significantly different binding energies observed in between different edge types i.e. Mo-ZZ and Se-ZZ edges with n-alkane molecules. Our findings indicate that the Mo-ZZ edge of monolayer

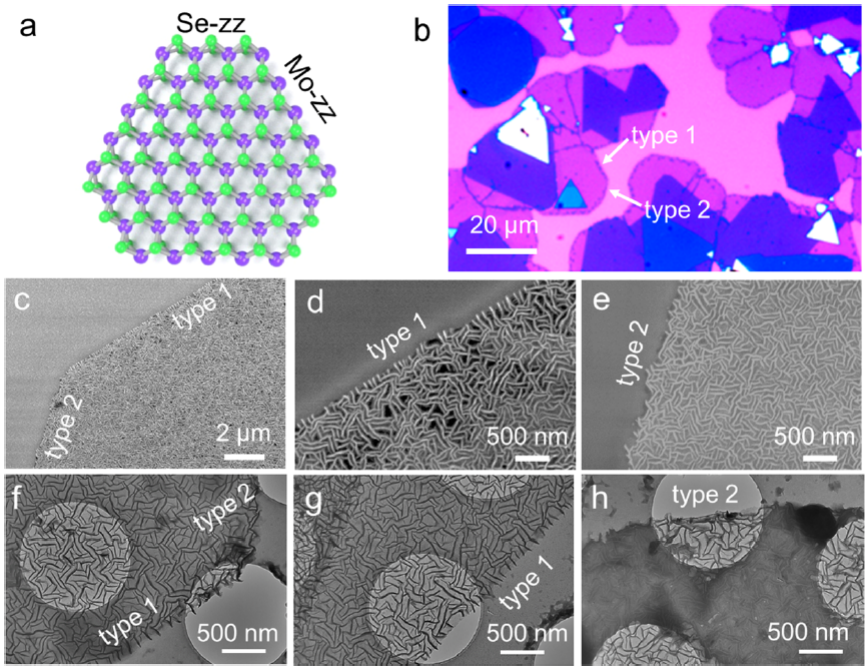

Figure 3.17: (a) The ball and stick model presented in (a) depicts the top-view microstructure of the monolayer $MoSe_2$ crystal, which adopts a truncated triangle shape showing Mo-ZZ and Se-ZZ termination edges. (b) An optical image providing a clear illustration of the as-grown $MoSe_2$ crystal showing the presence of two distinct edge types. Following this, (c-h) present scanning electron microscope (SEM) and transmission electron microscope (TEM) images showcasing the crystallization of PE on the edges of the as-grown $MoSe_2$

$MoSe_2$ is preferred for PE crystallization due to its stronger binding energy compared to the basal plane. Consequently, it is anticipated that the preferred alignment of PE lamellae perpendicular to the edge near the Se-ZZ edge will be reduced, as the Se-ZZ edge exhibits a lower binding energy (-0.405 eV) compared to Mo-ZZ edge. Monolayer transition-metal dichalcogenides often exhibit different edge terminations which is influenced by the crystal growth process. In $MoSe_2$, both Mo-ZZ and Se-ZZ terminations are energetically favorable edges during CVD growth. The transformation of Se-ZZ edges to Mo-ZZ edges is common due to the rapid growth of Se edges, resulting in truncated triangles with alternating Mo-ZZ and Se-ZZ terminations, as shown in Figure 3.17 (a). Figure 3.17b illustrates the growth of $MoSe_2$ in a Selenium rich environment, where truncated triangles begin merging into a continuous film of $MoSe_2$. Distinctive interactions between different edge types and polymer chains is evident in SEM and TEM images (Figure 3.17c-h). Type 1 edges, which are straight, initiate the preferred alignment of PE lamellae perpendicular to the edge (Figure 3.17d,g), as previously demonstrated in Figure 3.14. Conversely, type 2 edges, which are curved, do not exhibit such a preference with respect to the basal plane (Figure 3.17e,h). Although these type 1 and 2 edges are difficult to image even with atomic-resolution SEM at low acceleration voltages (60 keV). Nevertheless, these results support the predictions from ab-initio and MD simulations that changes in edge atomic configuration of a $MoSe_2$ sheet, such as the Se-ZZ or Mo-ZZ edge, can impact its ability to initiate polymer nucleation and crystal growth. Further studies using atomic-resolution imaging of edge configurations are required as it will offer more decisive evidence and understanding of interactions between different atomic edges with polymer chains.

3.5 Strained 2D substrate to induce anisotropy in nanocomposite

In this section we investigate the effect of straining 2D material to investigate the crystallisation angle of PE on top of 2D material. We hypothesize that by straining the 2D material, at interface we can deliberately create preferred crystallization of polymer chains creating anisotropy in the resulting 2D material based nanocomposite material. In this section we use graphene as our 2D material for the sake of simplicity and we again use PE as our polymer to deliberately crystallize the polyethylene material in a desired orientation on the surface of graphene.

A PE-graphene model was created with a PE density of 0.88 g/cc. The model was then allowed to equilibrate at 500K to get rid of residual stresses. The equilibrated PE-graphene model with randomly mixed polymer chains was used as an initial configuration to simulate the crystallization of polymer chains on the surface of graphene. The developed PE-graphene model in our study has periodic boundary conditions in the normal direction of the 2D graphene. Therefore, two crystallization growth fronts can be observed during the crystallization process of the PE in our simulations. To evaluate the crystallization process, fractional crystallization X(z) was estimated for each subdomain with a thickness of 0.35 nm in z direction at certain time steps as shown in Figure 3.18. It can be noted that Figure 3.18 (a) shows propagation of a crystallization front from the surface of graphene till the amorphous region in the middle. Each line represents fractional crystallization at certain distance away from the interface of graphene and PE (in the z direction) at a particular time during the crystallization process. The crystallization growth front proceeds away from the interface, in the bulk polyethylene parallel to 2D material interface, with the progression of time. Very low crystallisation was observed in the first 5 ns but after that crystallization growth front proceeds rapidly until 25 ns when the chains became highly ordered and start competing from other crystallization growth front starting from the second interface. Thus, between 25 ns and 75 ns crystal front moved at a very low

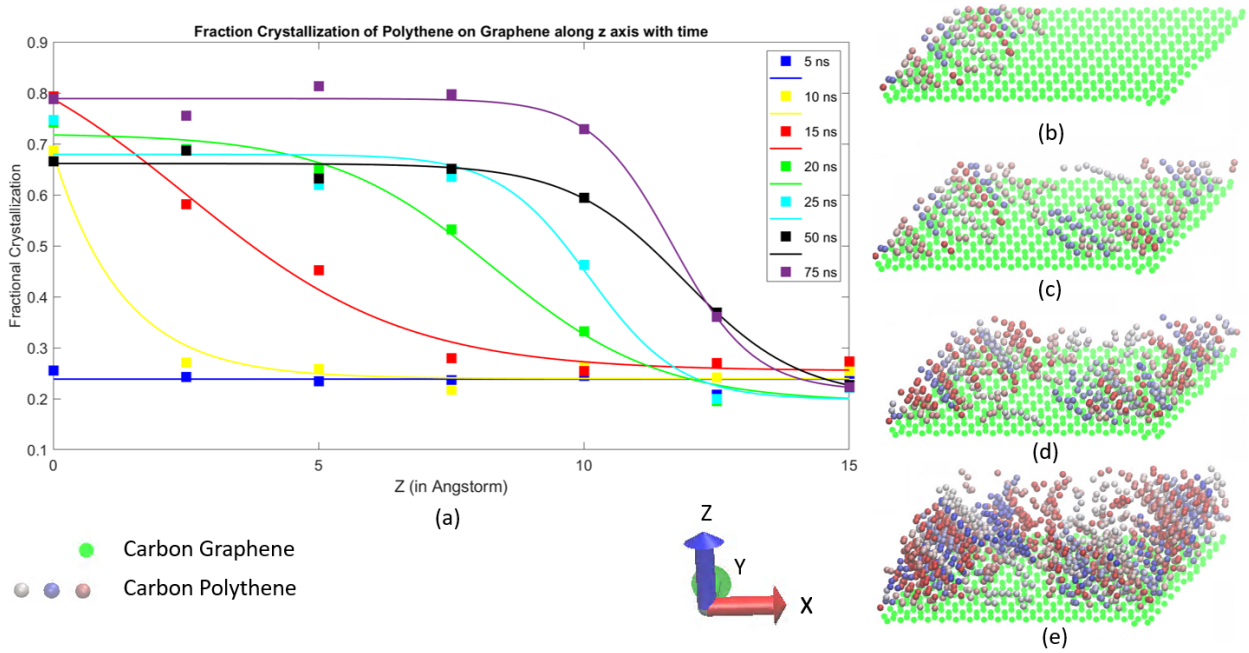

Figure 3.18: Fractional crystallisation profiles for crystallisation of PE on graphene surface

pace. This can be attributed to the fact that crystal front from both ends were competing to crystallize in the middle. Snapshots of polyethylene crystals growing from the surface of graphene is shown in Figure 3.18 (b)-(e). Ordering and densification of polyethylene chains was observed near the graphene surface at first with the axes of crystallized chains aligned at 150 degrees from the zig-zag direction of graphene.

Crystal structure of polyethylene were first characterized by the Bunn [86] as an orthorhombic unit cell. Orthorhombic unit cells are the most stable crystal structure for polyethylene when the temperature of polyethylene is below melting temperature. Polyethylene also exhibits monoclinic unit cells **monoclinic** but these crystal structures are only exhibited under high mechanical stress. Experimentally polyethylene's orthorhombic unit cell has lattice parameters a = 0.7407 nm, b = 0.49491 nm and c = 0.25511 nm where c is along the chain axis shown in Figure 3.19. This gives the crystallized polyethylene a crystal density of 996.2 Kgm^{-3}. Figure 3.19 illustrates the crystallized structure of self-assembled PE on graphene surface. Note, in an enlarged schematic orthorhombic unit cells of crystallized polyethylene chains were observed are shown for clarity.

3.5.1 Statistical quantification of crystallized PE on unstrained graphene surface

Multiple MD simulations were conducted to investigate templating effects of unstrained graphene for the guided crystallization of polyethylene. The interfacial crystallography along the contact plane between the polyethylene and graphene were characterized. In each simulation, graphene-polyethylene system was left to equilibrate at 500 K for at least 1 ns before quenching it to 360 K to observe the crystallization direction/orientation of polyethylene. To create initial crystallization models, after the 1 ns of equilibration, snapshots of randomly mixed PE with $MoSe_2$ at every 100 ps were captured. The snapshots were captured between 0- 2.4 ns simulation time which leads to 24 different realizations in MD simulations. In the simulation model we have two interfaces of graphene- polyethylene nanocomposite due to periodic boundary conditions

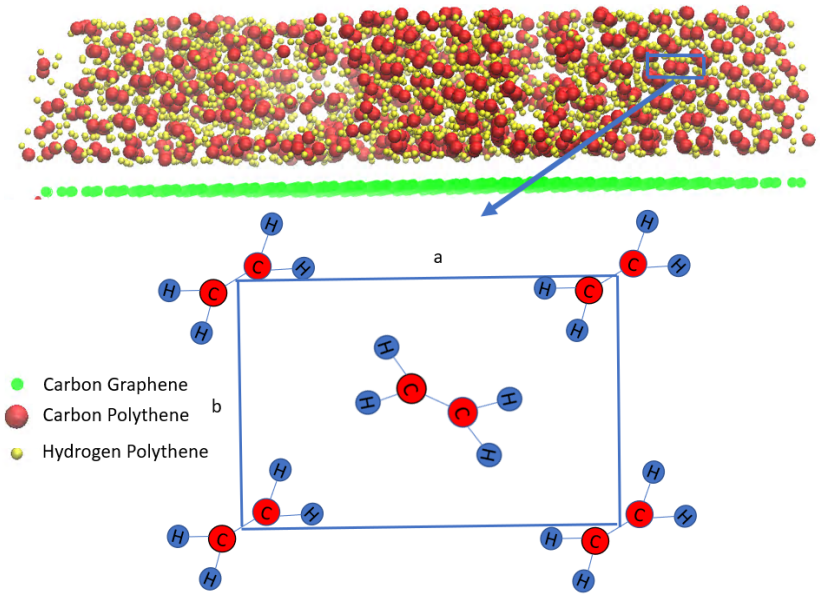

Figure 3.19: Unit cell of crystallised PE on graphene surface. It can be noticed that PE crystallises in orthorhombic crystal structure

in z direction. In x and y axes we have periodic boundary conditions which helps in simulating an infinitely long graphene sheet. Our simulation box has dimensions of 54 x 25.5 x 54 $Å^3$ with a total of 7631 atoms in which our graphene sheet had 624 atoms.

Figure 3.20 shows the observed interfacial crystallographic orientations of the first layer of polyethylene chains on graphene surface. The miller-bravais direction indices are adopted here to represent the crystallographic orientations and planes, which is a 4 axis coordinate system widely used to characterize 3 dimensional hexagonal crystal structure. Figure 3.20 (a)-(f) shows that the crystallized polyethylene in the first layer can have the chain directions at 85° and 165° for Figure 3.20 (a), 165° and 140° for Figure 3.20 (b), 120° for Figure 3.20 (c), 60° for Figure 3.20 (d), 30° and 150° for Figure 3.20 (e) and 30° for Figure 3.20 (f). Note that these crystallization orientations are not exhaustive and we observed other crystallization orientations too. These images, i.e. Figure 3.20 (a)-(f), just show the sample of few crystallised PE orientations observed on graphene surface. Figure 3.20 (g) shows the Miller-bravais indices of directions for equivalent configurations. X_1, X_2 and X_3 are principal hexagonal directions which are symmetric/equivalent and also represents valleys between zigzag lines. U_1, U_2 and U_3 are other three symmetric/equivalent directions representing valleys between armchair lines. It can be noted that there are only two crystallisation directions for PE chains i.e. PE chains can either choose to stay between zigzag valley or armchair valley on graphene surface.

From Figure 3.21 it can be observed that 33.3% of MD simulations i.e 14 out of 42 crystallisation orientations, shows the interfacial crystallographic orientation in (0°/$[\bar{1}2\bar{1}0]$, 60°/$[2\bar{1}\bar{1}0]$, 120°/$[\bar{1}\bar{1}20]$). On the other hand, 66.67% of the MD simulations i.e 28 out of 42 crystallisation orientations, have the crystalline polyethylene chains in the directions (30°/$[1\bar{1}00]$, 90°/$[\bar{1}010]$ and 150°/$[01\bar{1}0]$). Figure 3.21 also shows the frequency of observed crystallographic orientations in terms of exact orientation angles (the reference direction is 0°/$[\bar{1}2\bar{1}0]$) in all 24 MD simulations with 42 crystallisation orientations observed. This suggests that the guided assembly of polyethylene chains on the $MoSe_2$ surface prefer the orientation (30°/$[1\bar{1}00]$, 90°/$[\bar{1}010]$ and 150°/$[01\bar{1}0]$).

To understand the armchair interfacial crystallographic orientation, we tried looking closely at how

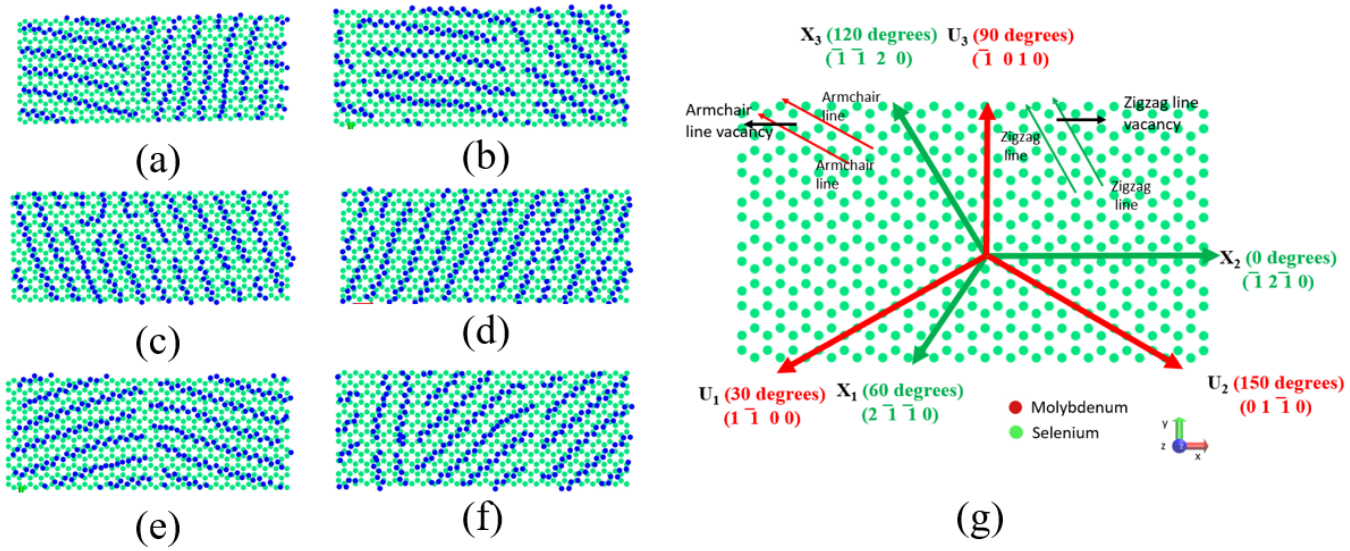

Figure 3.20: (a) Crystallisation of PE at 85° and 165° (b)Crystallisation of PE at 165° and 140° (c) Crystallisation of PE at 120° (d) Crystallisation of PE at 60° (e) Crystallisation of PE at 30° and 150° (f) Crystallisation of PE at 30° (g) shows Miller-bravais indices of directions for equivalent configurations on graphene surface. X_1, X_2 and X_3 are principal hexagonal directions which are symmetric/equivalent and represents valleys between zigzag lines on graphene surface. U_1, U_2 and U_3 are other three symmetric/equivalent directions representing valleys between armchair lines on graphene surface

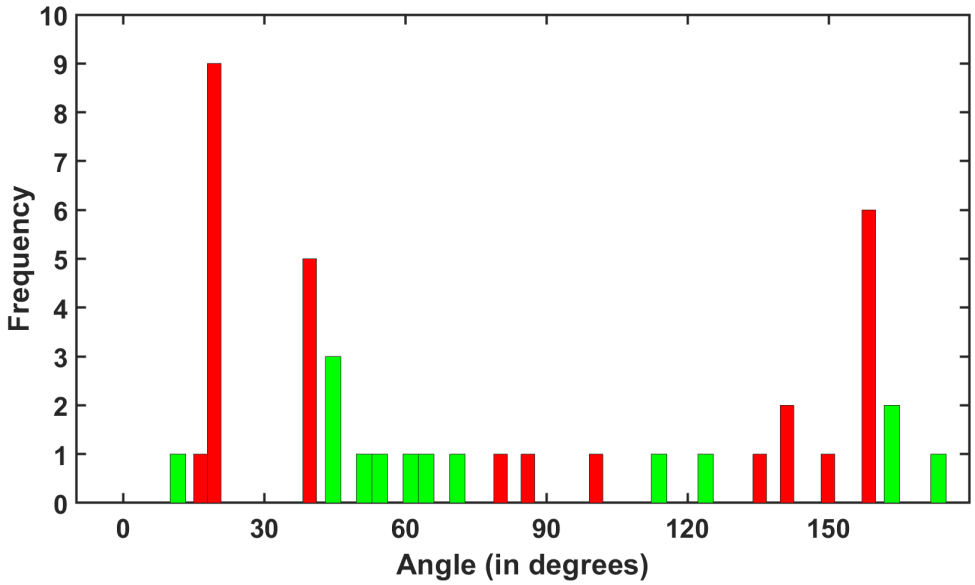

Figure 3.21: Histogram of all the angles observed, in counter-clockwise direction with respect to miller-bravais direction index $[\bar{1}2\bar{1}0]$, in 24 independent crystallization simulations of polyethylene on graphene surface. 0°, 60° and 120° crystallization orientations are shown with green color and 30°, 90° and 150° crystallization orientations are shown with red color

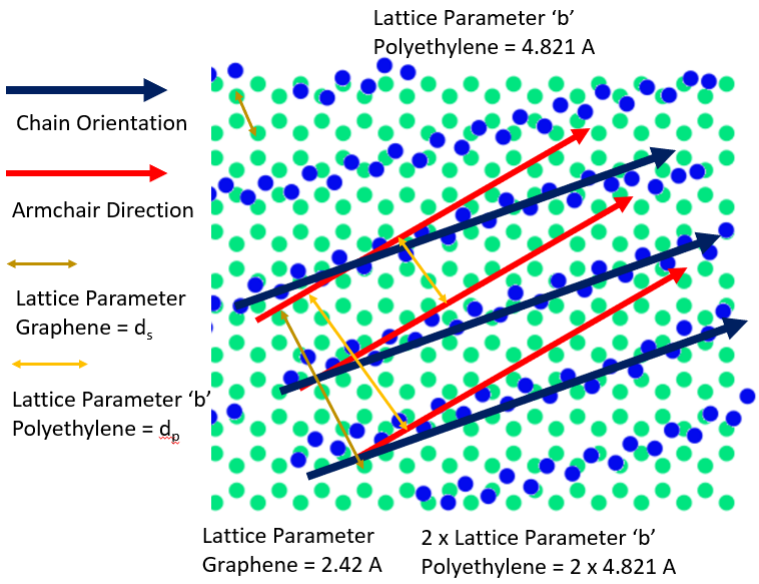

Figure 3.22: Shows 20 degrees crystallisation of polyethylene on graphene surface. Domain epitaxial matching between polyethylene chains and graphene surface can be observed as polyethylene chains repeat on graphene surface after every two armchair valleys

polymer chains register on the graphene surface. Figure 3.22 shows mutual interfacial crystallographic orientation at 20 degrees with horizontal/0 degrees crystallization orientation. Note that in Figure 3.22 carbon of first layer PE (blue) atoms are on top and carbon from graphene (green) atoms are shown at the bottom. Hydrogen atoms are not shown for clarity. In Figure 3.22 for the orientations $30°/[1\bar{1}00]$, $90°/[\bar{1}010]$ and $150°/[01\bar{1}0]$, it can be observed that polyethylene chains prefer to lie in alternate armchair valleys. We further investigated epitaxial lattice matching along the contact plane in the hybrid polyethylene/graphene system to understand the preference for an specific interfacial crystallographic orientations. Epitaxy usually means order in the relative orientation of identical crystals nucleated and grown on a large single-crystal seed surface where the deposited crystalline film is called an epitaxial film or epitaxial layer. In this study, we observe a heteroepitaxy i.e crystalline seed and epitaxial layers are formed from different materials. The crystalline seed is 2D graphene while the crystal film/epitaxial layer is polyethylene. The mutual orientations along the contact plane is (0001) graphene and (100) polyethylene. The interfacial orientation relationship can be largely determined by the intralayer strain energy or lattice misfit along the interface, which is defined as follows $\Delta = 100(d_p - d_s)/d_s$ [83] where d_p and d_s are the lattice parameters of polyethylene and $MoSe_2$ respectively. The epilayer trends to orient itself to minimize the lattice mismatch and lower the intralayer strain. According to Wittmann and Lotz [84] $\Delta < \pm 15\%$ is an acceptable range of lattice mismatch for continuous epitaxial growth. For the orientation $30°/[1\bar{1}00]$, $90°/[\bar{1}010]$ and $150°/[01\bar{1}0]$, d_{p1} is the interchain distance in the polyethylene epilayer while d_{s1} for the (1000) plane of graphene is the distance between alternate carbon atoms in the hexagonal ring of graphene, which were measured as shown in Figure 3.22. With $d_{s1} = 0.242 \cos 30°$ nm and $d_{p1} = 0.4837$ nm, lattice mismatch using these parameters is -99.99 % which suggests a large-lattice mismatch that is not favored by the epitaxial growth of polyethylene on graphene surface. It is reported that domain epitaxial growth can be observed for large-lattice-mismatch system. A domain of size nd_{s1} of the substrate matches with md_{p1} of the epilayer which leads to a small residual domain mismatch strain. As shown in Figure 3.22 (a), we can observe that every alternate polyethylene

chain is lying between armchair line valley. This results in n=2 and m=1 that leads to $d_{p2} = d_{p1}$ and $d_{s2} = 2d_{s1}$. And domain lattice-mismatch evaluated using d_{p2} and d_{s2} is -0.39 % which indicates a small domain lattice-mismatch strain. We believe the minimized intralayer strain within the epilayer from the small domain lattice-mismatch is responsible for domain epitaxial growth with the orientation in 30°/[1$\bar{1}$00], 90°/[$\bar{1}$010] and 150°/[01$\bar{1}$0].

3.5.2 Statistical quantification of crystallisation of PE on strained graphene surface

Multiple MD simulations were conducted to investigate templating effects of strained graphene for the guided crystallization of polyethylene. The interfacial crystallography along the contact plane between the polyethylene and graphene were characterized. We strained graphene in vertical direction i.e. U_3 direction/y-axis from Figure 3.20 (g). We strained the graphene by 10%, 15% and 20% and observed the change in crystallization orientations of crystallized polyethylene on the surface of graphene. The strain in graphene was applied along the armchair direction i.e perpendicular to the zigzag direction. Graphene has a Poisson's ratio of approximately 0.19 therefore stretching graphene along armchair direction shrinks the graphene in zigzag direction. In each simulation, graphene sheet was strained and kept at the bottom of randomly mixed polyethylene chains. Then, the strained graphene-polyethylene system was left to equilibrate at 500 K for at least 1 ns before quenching it to 360 K to observe the crystallization process of polyethylene on a strained graphene sheet. After the 1 ns equilibration, snapshots with an increment of 100 ps were captured and were used as the initial configurations for the crystallization process, which leads to 24 realizations in MD simulations for each strained case. As mentioned in our unstrained case, we have two interfaces of graphene polyethylene due to periodic boundary conditions in z direction. In x and y axes we again have periodic boundary conditions which helps us simulate infinitely long graphene sheet. Our simulation box had a total of 7631 atoms where our strained graphene sheet had 624 atoms.

10% strained graphene for crystallizing PE

Figure 3.23 shows the observed interfacial crystallographic orientations of the first layer of polymer chains on 10% strained graphene surface along armchair direction. The miller-bravais direction indices are again adopted here to represent the crystallographic orientations and planes in the strained graphene. Figure 3.23 (a)-(f) shows that the crystallized polyethylene in the first layer can have the chain directions at 150° for Figure 3.23 (a), 122° and 175° for Figure 3.23 (b), 150° and 30° for Figure 3.23 (c), 150° for Figure 3.23 (d), 155° and 35° for Figure 3.23 (e) and 30° and 15° for Figure 3.23 (f). Note that these crystallization orientations (shown in Figure 3.23) are not exhaustive and we observed other crystallization orientations too. These images, i.e. Figure 3.23 (a)-(f), just show the sample of crystallised PE orientations on 10 % armchair direction strained graphene surface. Figure 3.23 (g) shows the Miller-bravais indices of directions for equivalent configurations. X_1, X_2 and X_3 are principal hexagonal directions which are symmetric/equivalent and also represents valleys between zigzag lines. U_1, U_2 and U_3 are other three symmetric/equivalent directions representing valleys between armchair lines. It can be noted that there are only two crystallisation directions for PE chains. PE chains can either choose to stay between zigzag valley or armchair valley.

From Figure 3.24 it can be observed that 50% of MD simulations i.e 21 out of 42 crystallisation orientations, shows the interfacial crystallographic orientation in (0°, 61°, 122°). On the other hand, 50% of the MD simulations i.e 21 out of 42 crystallisation orientations, have the crystalline polyethylene chains in the directions

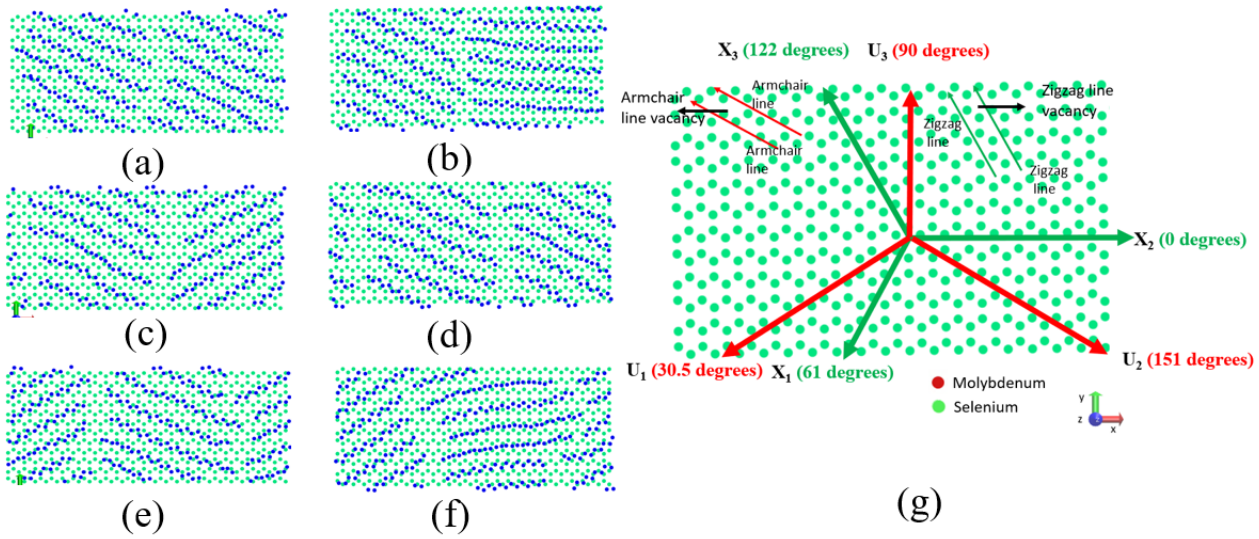

Figure 3.23: (a) Crystallisation of PE at 150° (b)Crystallisation of PE at 122° and 175° (c) Crystallisation of PE at 150° and 30° (d) Crystallisation of PE at 150° (e) Crystallisation of PE at 155° and 35° (f) Crystallisation of PE at 30° and 15° (g) shows Miller-bravais indices of directions for equivalent configurations. X_1, X_2 and X_3 are principal hexagonal directions which are symmetric/equivalent and also represents valleys between zigzag lines. U_1, U_2 and U_3 are other three symmetric/equivalent directions representing valleys between armchair lines. Note that U_1, U_2 and U_3 are not 60 degrees apart and similarly X_1, X_2 and X_3 directions are also not 60 degrees apart due to vertically strained graphene in this case

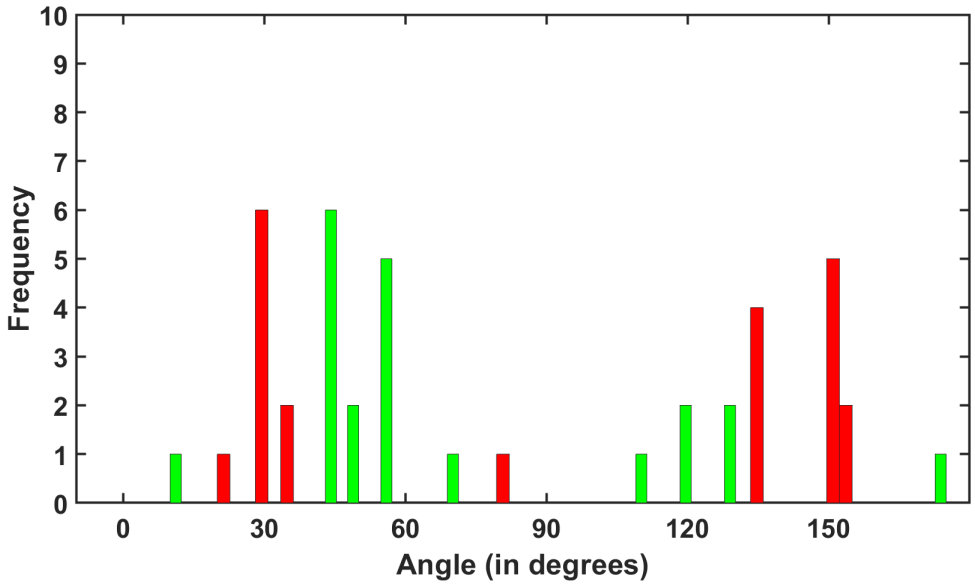

Figure 3.24: Histogram of all the angles observed counter-clockwise with respect to miller-bravais direction index $[\bar{1}2\bar{1}0]$ in 24 independent crystallization simulations of polyethylene on graphene surface. 0°, 61° and 122° crystallization orientations are shown with green color and 30.5°, 90° and 151° crystallization orientations are shown with red color

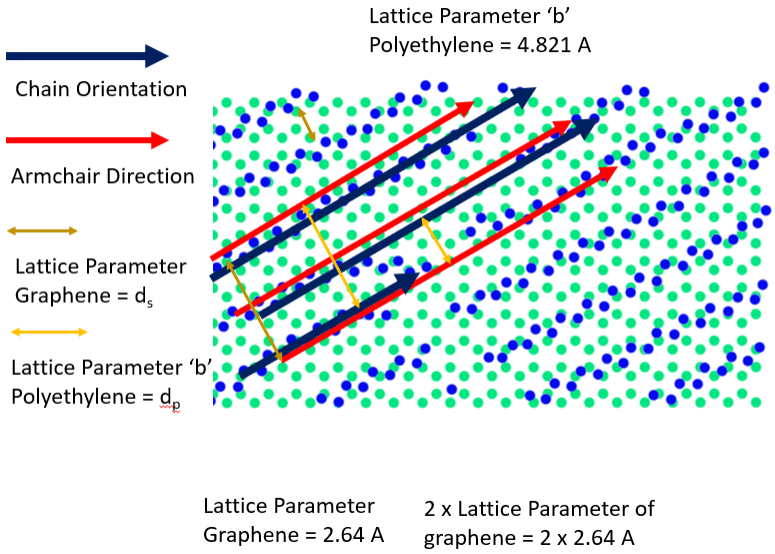

Figure 3.25: Shows 30° crystallisation of polyethylene on graphene surface. Domain epitaxial matching between polyethylene chains and 10 % armchair strained graphene surface can be observed as polyethylene chains repeat after every two armchair valleys

(30.5°, 90° and 151°). Figure 3.24 also shows the frequency of observed crystallographic orientations in terms of exact orientation angles (the reference direction is 0°) in all 24 MD simulations with 42 crystallisation orientation. It can be observed that the guided assembly of polyethylene chains on the $MoSe_2$ surface does not prefer any of the two crystallisation orientations i.e. (30.5°, 90° and 151°)/(0°, 61°, 122°) are almost equally favorable.

To understand the effect of strained graphene on armchair interfacial crystallographic orientation, we tried looking closely at how polymer chains register to the 10% strained graphene surface. Figure 3.25 shows mutual interfacial crystallographic orientation at 30° with horizontal/0 degrees crystallization orientation. Note that in Figure 3.25 carbon atom of first layer PE (blue) atoms are on top and carbon atom from graphene (green) atoms are at bottom. Hydrogen atoms are not shown for clarity. In Figure 3.25 for the orientations 30.5°, 90° and 151°, it can be observed that polyethylene chains prefer to lie in alternate armchair valleys. We further investigated epitaxial lattice matching along the contact plane in the hybrid polyethylene/graphene system to understand the preference of the interfacial crystallographic orientations. The mutual orientations along the contact plane is (0001) graphene and (100) polyethylene. The interfacial orientation relationship can be largely determined by the intralayer strain energy or lattice misfit along the interface, which is defined as follows $\Delta = 100(d_p - d_s)/d_s$ [83] where d_p and d_s are the lattice parameters of polyethylene and $MoSe_2$ respectively. The epilayer tends to orient itself to minimize the lattice mismatch and lower the intralayer strain. According to Wittmann and Lotz [84] $\Delta < \pm 15\%$ is an acceptable range of lattice mismatch for continuous epitaxial growth. For the orientation 30.5°, 90° and 151°, d_{p1} is the interchain distance in the polyethylene epilayer while d_{s1} for the (1000) plane of graphene is the distance between alternate carbon atoms in the hexagonal ring of graphene, which were measured as shown in Figure 3.25. With $d_{s1} = 0.264 \cos 30°$ nm and $d_{p1} = 0.4837$ nm, lattice mismatch using these parameters is -82.61 % which suggests a large-lattice-mismatch that is not favored by the epitaxial growth of polyethylene on graphene surface. It is reported that domain epitaxial growth can be observed for large-lattice-mismatch system. A domain of size nd_{s1} of the substrate

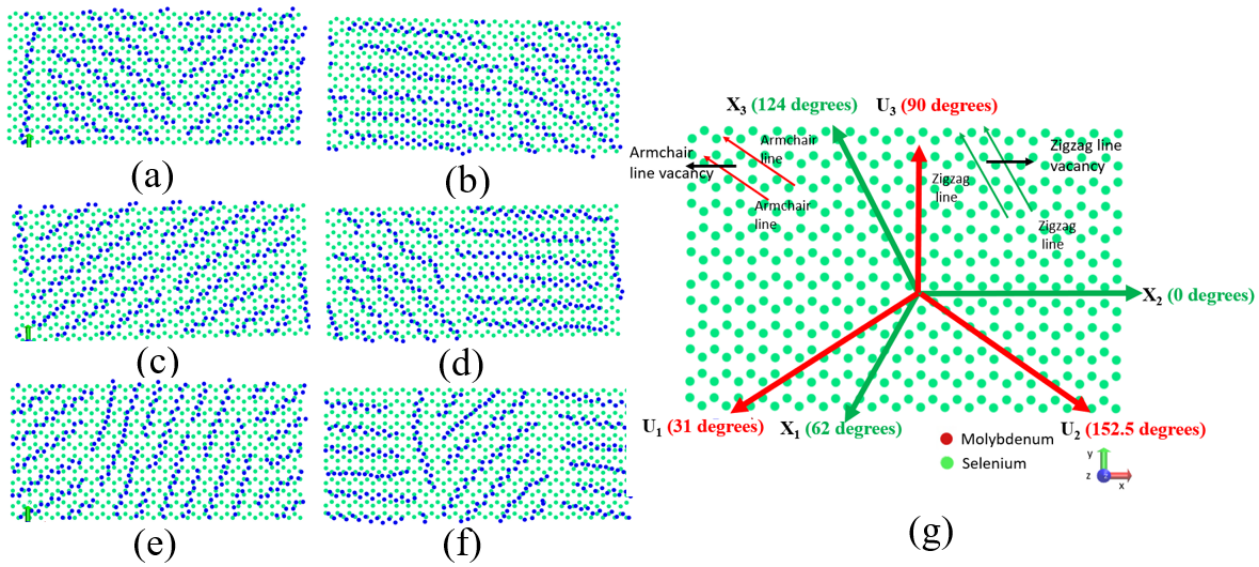

Figure 3.26: (a) Crystallisation of PE at 155° and 45° (b)Crystallisation of PE at 175° and 150° (c) Crystallisation of PE at 35° (d) Crystallisation of PE at 5° and 125° (e) Crystallisation of PE at 80° and 35° (f) Crystallisation of PE at 175° and 45° (g) shows Miller-bravais indices of directions for equivalent configurations. X_1, X_2 and X_3 are principal hexagonal directions which are symmetric/equivalent and also represents valleys between zigzag lines. U_1, U_2 and U_3 are other three symmetric/equivalent directions representing valleys between armchair lines. Note that U_1, U_2 and U_3 are not 60 degrees apart and similarly X_1, X_2 and X_3 directions are also not 60 degrees apart due to armchair (vertically) strained graphene

matches with md_{p1} of the epilayer which leads to a small residual domain mismatch strain. As shown in Figure 3.25 (a), we can observe that every alternate polyethylene chain is lying between armchair line valley. This results in n=2 and m=1 that leads to $d_{p2} = d_{p1}$ and $d_{s2} = 2d_{s1}$. And domain lattice-mismatch evaluated using d_{p2} and d_{s2} is -8.69 % which indicates a small domain lattice-mismatch strain. We believe the minimized intralayer strain within the epilayer from the small domain lattice-mismatch is responsible for domain epitaxial growth with the orientation in 30.5°, 90° and 151°.

15% strained graphene for crystallizing PE

Figure 3.26 shows the observed interfacial crystallographic orientations of the first layer of polymer chains on 15% strained graphene surface along armchair direction. The miller-bravais direction indices are again adopted here to represent the crystallographic orientations and planes in the strained graphene. Figure 3.26 (a)-(f) shows that the crystallized polyethylene in the first layer can have the chain directions at 155° and 45° for Figure 3.26 (a), 175° and 150° for Figure 3.26 (b), 35° for Figure 3.26 (c), 5° and 125° for Figure 3.26 (d), 80° and 35° for Figure 3.26 (e) and 175° and 45° for Figure 3.26 (f). Note that these crystallization orientations are not exhaustive and we observed other crystallization orientations too. These images, i.e. Figure 3.26 (a)-(f), just show the sample of crystallised PE orientations on 15 % strained graphene surface. Figure 3.26 (g) shows the Miller-bravais indices of directions for equivalent configurations. X_1, X_2 and X_3 are principal hexagonal directions which are symmetric/equivalent and also represents valleys between zigzag lines. U_1, U_2 and U_3 are other three symmetric/equivalent directions representing valleys between armchair lines. It can be noted that there are only two crystallisation directions for PE chains. PE chains can either choose to stay between zigzag valley or armchair valley.

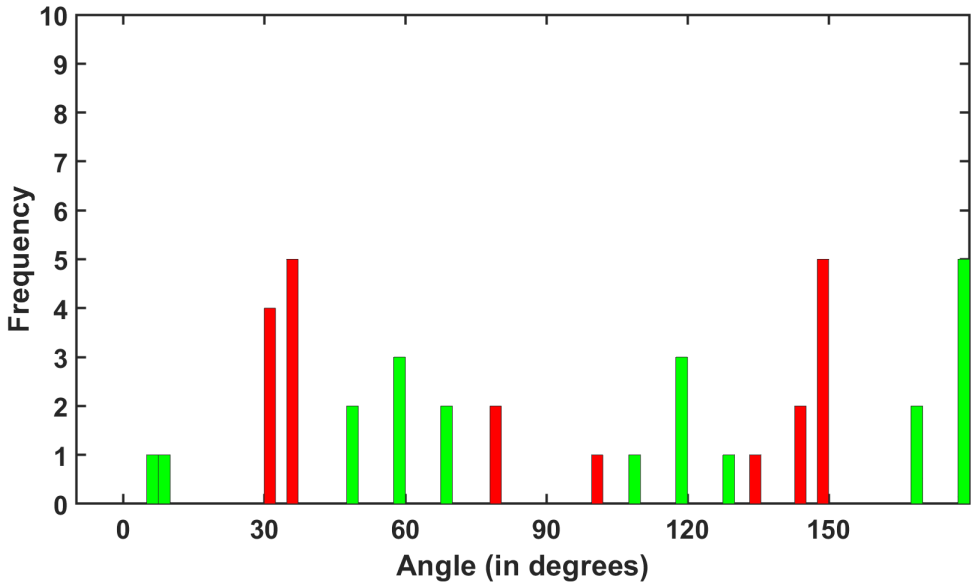

Figure 3.27: Histogram of all the angles observed counter-clockwise with respect to miller-bravais direction index $[\bar{1}2\bar{1}0]$ in 24 independent crystallization simulations of polyethylene on graphene surface. 0°, 62° and 124° crystallization is shown with green color and 31°, 90° and 152.5° crystallization is shown with red color

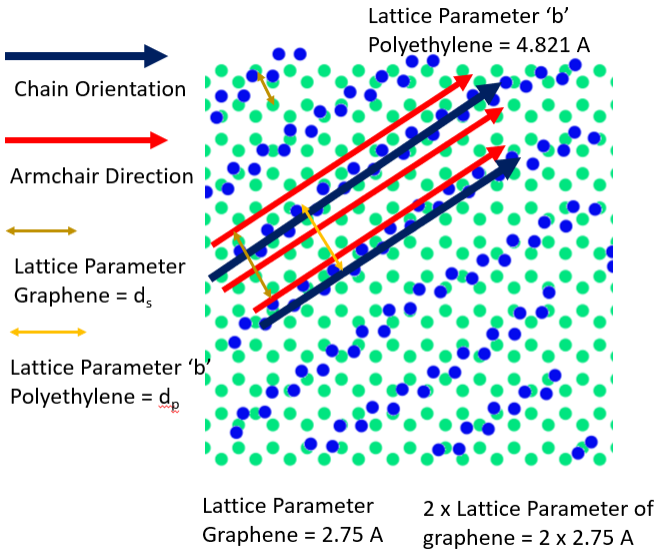

Figure 3.28: Shows 35° crystallisation of polyethylene on graphene surface. Domain epitaxial matching between polyethylene chains and 15 % strained graphene surface can be observed as polyethylene chains repeats after every two armchair valleys

From Figure 3.28 it can be observed that 51.21% of MD simulations i.e 21 out of 41 crystallisation orientations, shows the interfacial crystallographic orientation in (0°, 62°, 124°). On the other hand, 48.79% of the MD simulations i.e 20 out of 41 crystallisation orientations, have the crystalline polyethylene chains in the directions (31°, 90° and 152.5°). Figure 3.27 also shows the frequency of observed crystallographic orientations in terms of exact orientation angles (the reference direction is 0°) in all 24 MD simulations with 41 crystallisation orientation. It can be observed that the guided assembly of polyethylene chains on the $MoSe_2$ surface does not prefer any of the two crystallisation orientations.

To understand the effect of strained graphene on armchair interfacial crystallographic orientation, we tried looking closely at how polymer chains register to the 15% strained graphene surface. Figure 3.28 shows mutual interfacial crystallographic orientation at 35° with horizontal/0 degrees crystallization orientation. Note that in Figure 3.28 Carbon of first layer PE (blue) atoms are on top and carbon from graphene (green) atoms are at bottom. Hydrogen atoms are not shown for clarity. In Figure 3.28 for the orientations 31°, 90° and 152.5°, it can be observed that polyethylene chains prefer to lie in alternate armchair valleys. We further investigated epitaxial lattice matching along the contact plane in the hybrid polyethylene/graphene system to understand the preference of the interfacial crystallographic orientations. The mutual orientations along the contact plane is (0001) graphene and (100) polyethylene. The interfacial orientation relationship can be largely determined by the intralayer strain energy or lattice misfit along the interface, which is defined as follows $\Delta = 100(d_p - d_s)/d_s$ [83] where d_p and d_s are the lattice parameters of polyethylene and $MoSe_2$ respectively. The epilayer trends to orient itself to minimize the lattice mismatch and lower the intralayer strain. According to Wittmann and Lotz [84] $\Delta < \pm 15\%$ is an acceptable range of lattice mismatch for continuous epitaxial growth. For the orientation 31°, 90° and 152.5°, d_{p1} is the interchain distance in the polyethylene epilayer while d_{s1} for the (1000) plane of graphene is the distance between alternate carbon atoms in the hexagonal ring of graphene, which were measured as shown in Figure 3.28. With $d_{s1} = 0.275 \cos 30°$ nm and $d_{p1} = 0.4837$ nm, lattice mismatch using these parameters is -75.3 % which suggests a large-lattice-mismatch that is not favored by the epitaxial growth of polyethylene on graphene surface. It is reported that domain epitaxial growth can be observed for large-lattice-mismatch system. A domain of size nd_{s1} of the substrate matches with md_{p1} of the epilayer which leads to a small residual domain mismatch strain. As shown in Figure 3.28 (a), we can observe that every alternate polyethylene chain is lying between armchair line valley. This results in n=2 and m=1 that leads to $d_{p2} = d_{p1}$ and $d_{s2} = 2d_{s1}$. And domain lattice-mismatch evaluated using d_{p2} and d_{s2} is -12.35 % which indicates a small domain lattice-mismatch strain. We believe the minimized intralayer strain within the epilayer from the small domain lattice-mismatch is responsible for domain epitaxial growth with the orientation in 31°, 90° and 152.5°.

20% strained graphene for crystallizing PE

Figure 3.29 shows the observed interfacial crystallographic orientations of the first layer of polymer chains on 20% strained graphene surface along armchair direction. The miller-bravais direction indices are again adopted here to represent the crystallographic orientations and planes in the strained graphene. Figure 3.29 (a)-(f) shows that the crystallized polyethylene in the first layer can have the chain directions at 115° and 85° for Figure 3.29 (a), 80° for Figure 3.29 (b), 35° for Figure 3.29 (c), 60° and 30° for Figure 3.29 (d), 65° and 125° for Figure 3.29 (e) and 80° and 135° for Figure 3.29 (f). Note that these crystallization orientations are not exhaustive and we observed other crystallization orientations too. These images, i.e. Figure 3.29 (a)-(f), just show the sample of crystallised PE orientations on 15 % strained graphene surface. Figure 3.29 (g) shows the Miller-bravais indices of directions for equivalent configurations. X_1, X_2 and X_3 are principal

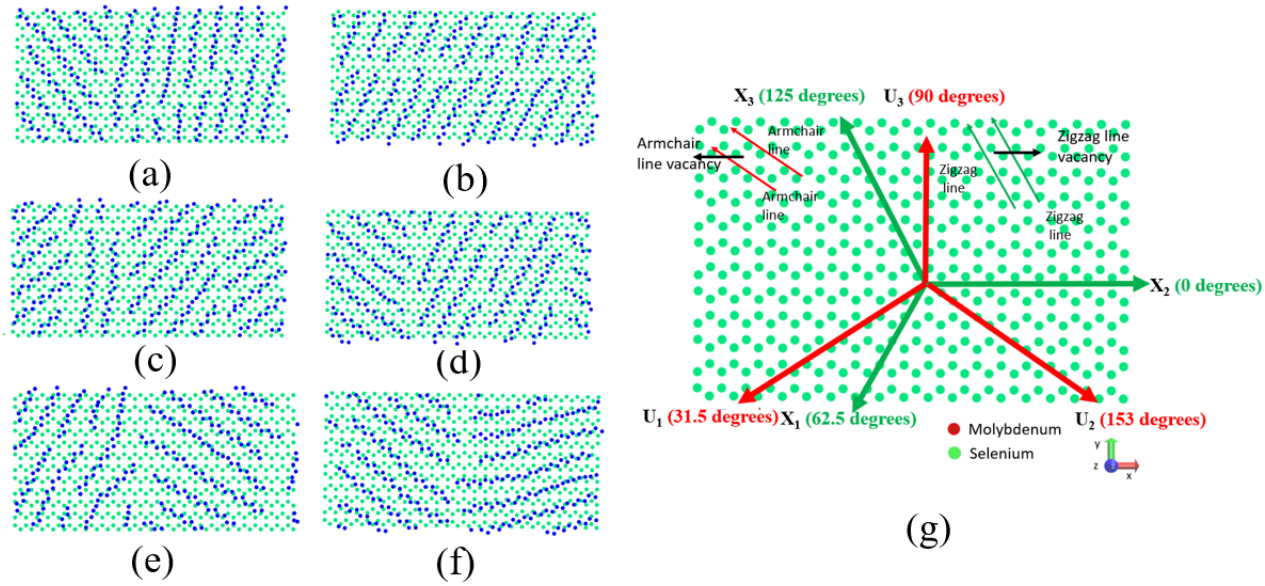

Figure 3.29: (a) Crystallisation of PE at 115° and 85° (b) Crystallisation of PE at 80° (c) Crystallisation of PE at 60° and 30° (d) Crystallisation of PE at 65° and 125° (e) Crystallisation of PE at 80° and 135° (f) Crystallisation of PE at 25° and 120° (g) shows Miller-bravais indices of directions for equivalent configurations. X_1, X_2 and X_3 are principal hexagonal directions which are symmetric/equivalent and also represents valleys between zigzag lines. U_1, U_2 and U_3 are other three symmetric/equivalent directions representing valleys between armchair lines. Note that U_1, U_2 and U_3 are not 60 degrees apart and similarly X_1, X_2 and X_3 directions are also not 60 degrees apart due to armchair (vertically) strained graphene

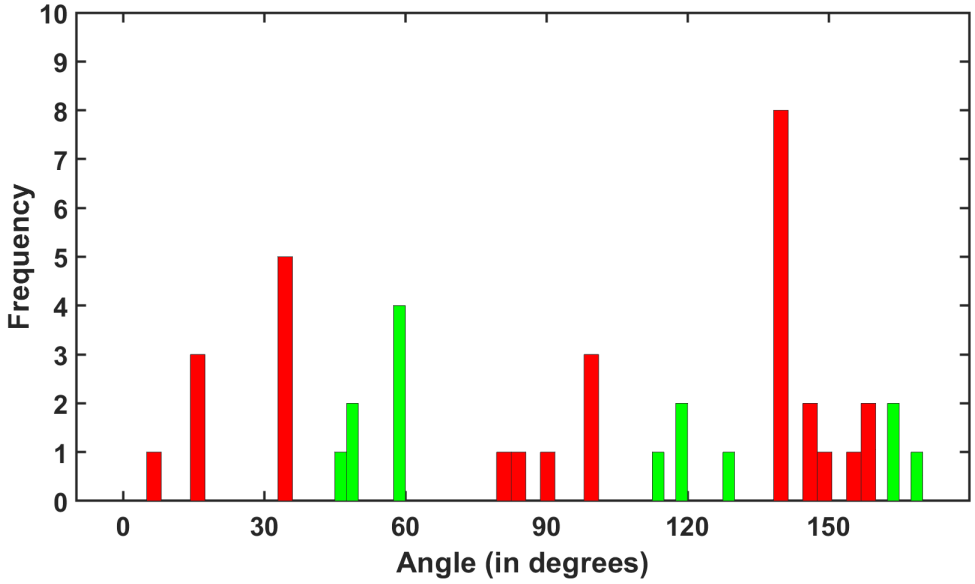

Figure 3.30: Histogram of all the angles observed counter-clockwise with respect to miller-bravais direction index $[\bar{1}2\bar{1}0]$ in 24 independent crystallization simulations of polyethylene on graphene surface. 0°, 62.5° and 125° crystallization is shown with green color and 31.5°, 90° and 153° crystallization is shown with red color

hexagonal directions which are symmetric/equivalent and also represents valleys between zigzag lines. U_1, U_2 and U_3 are other three symmetric/equivalent directions representing valleys between armchair lines. It can be noted that there are only two crystallisation directions for PE chains. PE chains can either choose to stay between zigzag valley or armchair valley.

From Figure 3.31 it can be observed that 32.55% of MD simulations i.e 14 out of 43 crystallisation orientations, shows the interfacial crystallographic orientation in (0°, 62.5°, 125°). On the other hand, 67.45% of the MD simulations i.e 29 out of 43 crystallisation orientations, have the crystalline polyethylene chains in the directions (31.5°, 90° and 153°). Figure 3.30 also shows the frequency of observed crystallographic orientations in terms of exact orientation angles (the reference direction is 0°) in all 24 MD simulations with 43 crystallisation orientation. It can be observed that the guided assembly of polyethylene chains on the $MoSe_2$ surface does prefer the crystallisation orientations (31.5°, 90° and 153°).

To understand the effect of strained graphene on armchair interfacial crystallographic orientation, we tried looking closely at how polymer chains register to the 20% strained graphene surface. Figure 3.31 shows mutual interfacial crystallographic orientation at 38° with horizontal/0 degrees crystallization orientation. Note that in Figure 3.31 Carbon of first layer PE (blue) atoms are on top and carbon from graphene (green) atoms are at bottom. Hydrogen atoms are not shown for clarity. In Figure 3.31 for the orientations 31.5°, 90° and 153°, it can be observed that polyethylene chains prefer to lie in alternate armchair valleys. We further investigated epitaxial lattice matching along the contact plane in the hybrid polyethylene/graphene system to understand the preference of the interfacial crystallographic orientations. The mutual orientations along the contact plane is (0001) graphene and (100) polyethylene. The interfacial orientation relationship can be largely determined by the intralayer strain energy or lattice misfit along the interface, which is defined as follows $\Delta = 100(d_p - d_s)/d_s$ [83] where d_p and d_s are the lattice parameters of polyethylene and $MoSe_2$ respectively. The epilayer trends to orient itself to minimize the lattice mismatch and lower

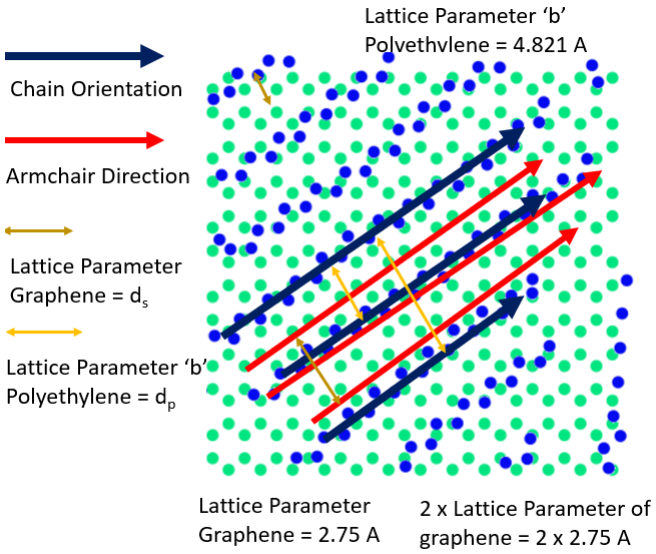

Figure 3.31: Shows 38° crystallisation of polyethylene on graphene surface. Domain epitaxial matching between polyethylene chains and 15 % strained graphene surface can be observed as polyethylene chains after every two armchair valleys

the intralayer strain. According to Wittmann and Lotz [84] $\Delta < \pm 15\%$ is an acceptable range of lattice mismatch for continuous epitaxial growth. For the orientation 31.5°, 90° and 153°, d_{p1} is the interchain distance in the polyethylene epilayer while d_{s1} for the (1000) plane of graphene is the distance between alternate carbon atoms in the hexagonal ring of graphene, which were measured as shown in Figure 3.31. With $d_{s1} = 0.283 \cos 30°$ nm and $d_{p1} = 0.4837$ nm, lattice mismatch using these parameters is -70.35 % which suggests a large-lattice-mismatch that is not favored by the epitaxial growth of polyethylene on graphene surface. It is reported that domain epitaxial growth can be observed for large-lattice-mismatch system. A domain of size nd_{s1} of the substrate matches with md_{p1} of the epilayer which leads to a small residual domain mismatch strain. As shown in Figure 3.31 (a), we can observe that every alternate polyethylene chain is lying between armchair line valley. This results in n=2 and m=1 that leads to $d_{p2} = d_{p1}$ and $d_{s2} = 2d_{s1}$. And domain lattice-mismatch evaluated using d_{p2} and d_{s2} is -14.82 % which indicates a relatively large domain lattice-mismatch strain. We believe that this large domain and epitaxial mismatch of intralayer strain is responsible for not supporting the domain epitaxial growth with the orientation in 0°, 62.5° and 125° and now supports 31.5°, 90° and 153° degrees crystallization orientation.

3.6 Conclusion

In this study, the dynamic polyethylene assembly on $MoSe_2$/graphene surfaces was successfully analyzed by conducting MD simulations. We have investigated the influence of the interchain interactions in polyethylene and interfacial interaction between polyethylene and $MoSe_2$/graphene on the assembly process of polyethylene. It is noted that interchain interaction can strongly impact the melting temperature of polyethylene and the crystallization process while the interfacial interaction shows less influence on the polyethylene assembly process. The melting temperature is found to increase with increased interchain interaction. The assembly process was characterized using fractional crystallization X to show the growth of crystalline polyethylene

as a function of time. Initially we observe a high crystallisation growth rate (up to 25 ns) and then a slow crystallization growth was observed from 25 ns - 75 ns. It is observed that the resulted crystalline polyethylene structure is orthorhombic and in conformance with the experimental results of Alsaygh et.al. [85]. Orthorhombic crystal phase of polyethylene exhibits pronounced anisotropic properties. Thus, oriented crystallisation of polymer on $MoSe_2$ surface can help in achieving directional crystallisation and thus controlled material properties.

Interfacial crystallography was examined at the interface between polyethylene and $MoSe_2$ to study how $MoSe_2$ influences the self-assembly of polyethylene. The study revealed that polyethylene chains align with the surface of $MoSe_2$ in two distinct orientations: (1) $0°/[\bar{1}2\bar{1}0]$, $60°/[2\bar{1}\bar{1}0]$, $120°/[\bar{1}\bar{1}20]$, and (2) $30°/[1\bar{1}00]$, $90°/[\bar{1}010]$, $150°/[01\bar{1}0]$ on the (0001) plane of $MoSe_2$. Among the 24 MD simulations conducted, approximately 58.3% exhibited the former orientation, while 41.7% showed the latter orientation. The lattice mismatch between polyethylene and $MoSe_2$ for full coherence was found to be significant (i.e., 68.24% for the former orientation and 187.3% for the latter orientation), whereas the domain lattice mismatch was relatively small (i.e., 12.1% for the former orientation and -8.1% for the latter orientation), indicating low strain in the epitaxial layer. The reduced strain energy resulting from the domain lattice mismatch favors the epitaxial growth of polyethylene on the $MoSe_2$ surface. In the former orientation, half of the polyethylene chains were observed to lie between Se lines to achieve domain epitaxial lattice matching and minimize epitaxial strain. In contrast, for the latter orientation, polyethylene chains were situated in the narrow valleys between mixed Mo/Se lines. Coincident atom sites observed at the $MoSe_2$-polyethylene interface suggest a preference for the $0°/ [\bar{1}2\bar{1}0]$, $60°/ [2\bar{1}\bar{1}0]$, $120°/ [\bar{1}\bar{1}20]$ orientation over the $30°/ [1\bar{1}00]$, $90°/ [\bar{1}010]$, $150°/ [01\bar{1}0]$ orientation. The steric hindrance between selenium and carbon atoms is less in the former orientation, as carbon atoms settle in the valleys between selenium atoms. This is supported by the evaluation of cohesive energy between the two crystallization orientations, further confirming the preference for the $0°/ [\bar{1}2\bar{1}0]$, $60°/ [2\bar{1}\bar{1}0]$, $120°/ [\bar{1}\bar{1}20]$ crystallization over the $30°/ [1\bar{1}00]$, $90°/ [\bar{1}010]$, $150°/ [01\bar{1}0]$ orientation. This selective preference for the crystallization orientation of polyethylene on $MoSe_2$ illustrates that 2D materials can guide the self-assembly of polyethylene chains in specific orientation directions through epitaxial growth. This presents a promising research direction to control the long-range order in the crystalline polymer and tailor the properties of both the polymer layer and the overall hybrid material. With the ability to attach different functional groups to the alkane chains, guided polymer assembly on 2D materials can be utilized to develop functional hybrid materials with precisely positioned functional groups at the molecular scale in the organic layer relative to the 2D materials substrate, thereby enabling the design of novel flexible electronic and optoelectronic materials. We also investigated the selective crystallisation of PE on graphene and $MoSe_2$ surface by two different strategies. In the first we investigated the selective crystallization of PE on $MoSe_2$ surface through edge crystallisation and have proved that $MoSe_2$ edges (Mo-ZZ) act as selective interfaces and can help guide the crystallization of PE on $MoSe_2$ surface. We also investigated the strained graphene surface for crystallization of PE and have proved that by vertically straining the graphene substrate we can selectively change the crystallization orientation of PE from armchair to zigzag direction (within the physical limit of graphene i.e. 20% strain)

Chapter 4

CONCLUSIONS AND FUTURE WORK

Molecular Dynamics simulations have been used for over two decades to simulate material system at small time and length scales and evaluate material behaviour from non-continuum approach. MD simulations has been used where experimentalists and theorists fail to characterize materials response. This makes MD simulations to become a powerful tool to investigate material behaviour at small length and time scales. This dissertation focuses on the development of computational methods for investigating 2D materials based nanocomposites and address two problems in particular. First, is the development of better interatomic potentials for MD simulations. Second, is the characterization of 2D material based nanomaterials and understanding their interface to investigate their behaviour and potential templating effects of 2D materials in these nanocomposites.

The fidelity of MD simulations has been dependent on the accuracy of empirical potentials used to characterize the material behaviour. Density Functional theory simulations use quantum mechanical approach to investigate the material behaviour at small length and time scale but due to high computational cost associated with these simulations we cannot scale the size and simulation time of DFT simulations. In this study we have created a method to develop machine learning based interatomic potentials for MD simulations learnt from the simulation results of DFT simulations. This gives us the accuracy of DFT simulations in MD simulations and thus we can simulate material properties of materials with higher accuracy with a fraction of computational cost. This dissertation focuses on the development of machine learning potentials for graphene, most prominent 2D material, and evaluate its material properties like coefficient of thermal expansion, lattice parameter, young's modulus and ultimate tensile strength. Especially evaluation of CTE for graphene is an elusive material property for theorists and experimentalists and this dissertation has provided new insights in the evaluation of CTE for graphene.

Once we have developed 2D material's interatomic potentials we can now simulate 2D material based nanocomposite with better accuracy. Now, using these MLPs we can investigate the templating effects of 2D material on crystallization of polymers. This dissertation specifically focuses on the templating effect of $MoSe_2$ and graphene on crystallization of polyethylene. We found through interfacial crystallography that for $MoSe_2$-PE material system $0°/60°/120°$ crystallization orientation of PE is preferred over $30°/90°/150°$ crystallization orientation due to higher adsorption energy, less domain mismatch, lower distance between PE and $MoSe_2$. We also found that for $MoSe_2$-PE material system $MoSe_2$ edge can be used as a template to

specifically crystallize PE parallel to $MoSe_2$ edge. In one other case study in this dissertation using graphene-PE as the material system we have found that straining the graphene sheet can change the preferential crystallization orientation of PE on graphene surface and thus can be used to create anisotropy (tuning knob) to alter material properties in the resulting nanocomposite.

This dissertation still leaves a few open questions that needs to be investigated to get a better understanding of 2D material based nanocomposites. We need to improve the efficiency of MLPs by doing uncertainty quantification of symmetry functions for different materials. From initial studies we can conclude that their is high level of redundancy in symmetry functions used in this study. Also, for understanding the templating effects of 2D materials for the development of nanocomposites we need to further investigate the straining effects of 2D materials in different directions and fine tuned values to help polymer selectively prefer just one crystallization orientation. These questions if addressed will help us to characterize 2D materials based nanocomposites with ease in the future to come.

References

[1] K. S. Novoselov, A. K. Geim, S. V. Morozov, *et al.*, "Electric field effect in atomically thin carbon films," *Science*, vol. 306, no. 5696, pp. 666–669, 2004. DOI: 10.1126/science.1102896.

[2] A. Singh and Y. Li, "Guided self-assembly of polyethene on graphene," in *AIAA SCITECH 2022 Forum*. DOI: 10.2514/6.2022-2143.

[3] D. Zhou, M. Fuentes-Cabrera, A. Singh, *et al.*, "Atomic edge-guided polyethylene crystallization on monolayer two-dimensional materials," *Macromolecules*, vol. 55, no. 2, pp. 559–567, 2022. DOI: 10.1021/acs.macromol.1c01978.

[4] A. Singh and Y. Li, "2d materials guided self-assembly of polymer: Molecular dynamics simulation study," in *AIAA SCITECH 2023 Forum*. DOI: 10.2514/6.2023-0142.

[5] A. Singh, M. Sun, J. Chen, B. Li, and Y. Li, "Templating effect of mose2 on crystallization of polyethylene: A molecular dynamics simulation study," *The Journal of Physical Chemistry C*, vol. 128, no. 5, pp. 2147–2162, 2024. DOI: 10.1021/acs.jpcc.3c06850.

[6] A. F. Carvalho, B. Kulyk, A. J. S. Fernandes, E. Fortunato, and F. M. Costa, "A review on the applications of graphene in mechanical transduction," *Advanced Materials*, vol. n/a, no. n/a, p. 2 101 326, DOI: https://doi.org/10.1002/adma.202101326.

[7] A. A. Balandin, S. Ghosh, W. Bao, *et al.*, "Superior thermal conductivity of single-layer graphene," *Nano Letters*, vol. 8, no. 3, pp. 902–907, Mar. 2008, ISSN: 1530-6984. DOI: 10.1021/nl0731872.

[8] H. Chen, M. B. Müller, K. J. Gilmore, G. G. Wallace, and D. Li, "Mechanically strong, electrically conductive, and biocompatible graphene paper," *Advanced Materials*, vol. 20, no. 18, pp. 3557–3561, DOI: https://doi.org/10.1002/adma.200800757.

[9] C. Lee, X. Wei, J. W. Kysar, and J. Hone, "Measurement of the elastic properties and intrinsic strength of monolayer graphene," *Science*, vol. 321, no. 5887, pp. 385–388, 2008. DOI: 10.1126/science.1157996.

[10] J.-U. Lee, D. Yoon, and H. Cheong, "Estimation of young's modulus of graphene by raman spectroscopy," en, *Nano Lett.*, vol. 12, no. 9, pp. 4444–4448, Sep. 2012.

[11] W. Bao, F. Miao, Z. Chen, *et al.*, "Controlled ripple texturing of suspended graphene and ultrathin graphite membranes," *Nature Nanotechnology*, vol. 4, no. 9, pp. 562–566, Sep. 2009, ISSN: 1748-3395. DOI: 10.1038/nnano.2009.191.

[12] D. Yoon, Y.-W. Son, and H. Cheong, "Negative thermal expansion coefficient of graphene measured by raman spectroscopy," *Nano Letters*, vol. 11, no. 8, pp. 3227–3231, 2011, PMID: 21728349. DOI: 10.1021/nl201488g.

[13] G. Yang, L. Li, W. B. Lee, and M. C. Ng, "Structure of graphene and its disorders: A review," *Sci. Technol. Adv. Mater.*, vol. 19, no. 1, pp. 613–648, Aug. 2018.

[14] S. Manigandan, P. Gunasekar, S. Nithya, G. D. Revanth, and A. V. S. C. Anudeep, "Experimental analysis of graphene nanocomposite on kevlar," *IOP Conference Series: Materials Science and Engineering*, vol. 225, p. 012 061, Aug. 2017. DOI: 10.1088/1757-899x/225/1/012061.

[15] T. Shao, B. Wen, R. Melnik, S. Yao, Y. Kawazoe, and Y. Tian, "Temperature dependent elastic constants and ultimate strength of graphene and graphyne," *The Journal of Chemical Physics*, vol. 137, no. 19, p. 194 901, 2012. DOI: 10.1063/1.4766203.

[16] N. Mounet and N. Marzari, "First-principles determination of the structural, vibrational and thermodynamic properties of diamond, graphite, and derivatives," *Phys. Rev. B*, vol. 71, p. 205 214, 20 May 2005. DOI: 10.1103/PhysRevB.71.205214.

[17] S. A. Hollingsworth and R. O. Dror, "Molecular dynamics simulation for all," *Neuron*, vol. 99, no. 6, pp. 1129–1143, Sep. 2018, S0896-6273(18)30684-6[PII], ISSN: 1097-4199. DOI: 10.1016/j.neuron.2018.08.011.

[18] Y. Li and G. D. Seidel, "Multiscale modeling of the effects of nanoscale load transfer on the effective elastic properties of unfunctionalized carbon nanotube–polyethylene nanocomposites," *Modelling and Simulation in Materials Science and Engineering*, vol. 22, no. 2, p. 025 023, Feb. 2014. DOI: 10.1088/0965-0393/22/2/025023.

[19] Y. Li and G. Seidel, "Multiscale modeling of functionalized interface effects on the effective elastic material properties of cnt–polyethylene nanocomposites," *Computational Materials Science*, vol. 107, pp. 216–234, 2015, ISSN: 0927-0256. DOI: https://doi.org/10.1016/j.commatsci.2015.05.006.

[20] M. H. Rahman, S. Mitra, M. Motalab, and P. Bose, "Investigation on the mechanical properties and fracture phenomenon of silicon doped graphene by molecular dynamics simulation," *RSC Adv.*, vol. 10, pp. 31 318–31 332, 52 2020. DOI: 10.1039/D0RA06085B. [Online]. Available: http://dx.doi.org/10.1039/D0RA06085B.

[21] A. Singh, X. Chen, Y. Li, S. Koric, and E. Guleryuz, "Development of artificial neural network potential for graphene," in *AIAA Scitech 2020 Forum*. DOI: 10.2514/6.2020-1861.

[22] P. Rowe, G. Csányi, D. Alfè, and A. Michaelides, "Development of a machine learning potential for graphene," *Phys. Rev. B*, vol. 97, p. 054 303, 5 Feb. 2018. DOI: 10.1103/PhysRevB.97.054303.

[23] A. P. Thompson, H. M. Aktulga, R. Berger, *et al.*, "LAMMPS - a flexible simulation tool for particle-based materials modeling at the atomic, meso, and continuum scales," *Comp. Phys. Comm.*, vol. 271, p. 108 171, 2022. DOI: 10.1016/j.cpc.2021.108171.

[24] A. Singraber, J. Behler, and C. Dellago, "Library-based lammps implementation of high-dimensional neural network potentials," *Journal of Chemical Theory and Computation*, vol. 15, no. 3, pp. 1827–1840, 2019, PMID: 30677296. DOI: 10.1021/acs.jctc.8b00770.

[25] J. Behler, "Atom-centered symmetry functions for constructing high-dimensional neural network potentials," *The Journal of Chemical Physics*, vol. 134, no. 7, p. 074 106, 2011. DOI: 10.1063/1.3553717.

[26] S. Stankovich, D. A. Dikin, G. H. B. Dommett, *et al.*, "Graphene-based composite materials," *Nature*, vol. 442, no. 7100, pp. 282–286, Jul. 2006, ISSN: 1476-4687. DOI: 10.1038/nature04969.

[27] G. Bebis and M. Georgiopoulos, "Feed-forward neural networks," *IEEE Potentials*, vol. 13, no. 4, pp. 27–31, 1994. DOI: 10.1109/45.329294.

[28] P. Giannozzi, S. Baroni, N. Bonini, *et al.*, "QUANTUM ESPRESSO: A modular and open-source software project for quantum simulations of materials," en, *J. Phys. Condens. Matter*, vol. 21, no. 39, p. 395 502, Sep. 2009.

[29] N. Artrith, A. Urban, and G. Ceder, "Efficient and accurate machine-learning interpolation of atomic energies in compositions with many species," *Phys. Rev. B*, vol. 96, p. 014 112, 1 Jul. 2017. DOI: 10.1103/PhysRevB.96.014112.

[30] M. Fitzner, G. C. Sosso, S. J. Cox, and A. Michaelides, "The many faces of heterogeneous ice nucleation: Interplay between surface morphology and hydrophobicity," *Journal of the American Chemical Society*, vol. 137, no. 42, pp. 13 658–13 669, 2015, PMID: 26434775. DOI: 10.1021/jacs.5b08748.

[31] J. H. Los and A. Fasolino, "Intrinsic long-range bond-order potential for carbon: Performance in monte carlo simulations of graphitization," *Phys. Rev. B*, vol. 68, p. 024 107, 2 Jul. 2003. DOI: 10.1103/PhysRevB.68.024107.

[32] S. J. Stuart, A. B. Tutein, and J. A. Harrison, "A reactive potential for hydrocarbons with intermolecular interactions," *The Journal of Chemical Physics*, vol. 112, no. 14, pp. 6472–6486, 2000. DOI: 10.1063/1.481208.

[33] C. P. Herrero and R. Ramírez, "Structural and thermodynamic properties of diamond: A path-integral monte carlo study," *Phys. Rev. B*, vol. 63, p. 024 103, 2 Dec. 2000. DOI: 10.1103/PhysRevB.63.024103.

[34] K. V. Zakharchenko, M. I. Katsnelson, and A. Fasolino, "Finite temperature lattice properties of graphene beyond the quasiharmonic approximation," *Phys. Rev. Lett.*, vol. 102, p. 046 808, 4 Jan. 2009. DOI: 10.1103/PhysRevLett.102.046808.

[35] G. A. McQuade, A. S. Plaut, A. Usher, and J. Martin, "The thermal expansion coefficient of monolayer, bilayer, and trilayer graphene derived from the strain induced by cooling to cryogenic temperatures," *Applied Physics Letters*, vol. 118, no. 20, p. 203 101, 2021. DOI: 10.1063/5.0035391.

[36] Q. Feng, D. Wei, Y. Su, Z. Zhou, F. Wang, and C. Tian, "Study of thermal expansion coefficient of graphene via raman Micro-Spectroscopy: Revisited," en, *Small*, vol. 17, no. 12, e2006146, Feb. 2021.

[37] V. Singh, S. Sengupta, H. S. Solanki, *et al.*, "Probing thermal expansion of graphene and modal dispersion at low-temperature using graphene nanoelectromechanical systems resonators," *Nanotechnology*, vol. 21, no. 16, p. 165 204, Mar. 2010. DOI: 10.1088/0957-4484/21/16/165204.

[38] S. Linas, Y. Magnin, B. Poinsot, *et al.*, "Interplay between raman shift and thermal expansion in graphene: Temperature-dependent measurements and analysis of substrate corrections," *Phys. Rev. B*, vol. 91, p. 075 426, 7 Feb. 2015. DOI: 10.1103/PhysRevB.91.075426.

[39] J.-W. Jiang, J.-S. Wang, and B. Li, "Thermal expansion in single-walled carbon nanotubes and graphene: Nonequilibrium green's function approach," *Phys. Rev. B*, vol. 80, p. 205 429, 20 Nov. 2009. DOI: 10.1103/PhysRevB.80.205429.

[40] Y. Magnin, G. D. Förster, F. Rabilloud, F. Calvo, A. Zappelli, and C. Bichara, "Thermal expansion of free-standing graphene: Benchmarking semi-empirical potentials," *Journal of Physics: Condensed Matter*, vol. 26, no. 18, p. 185 401, Apr. 2014. DOI: 10.1088/0953-8984/26/18/185401.

[41] W. Gao and R. Huang, "Thermomechanics of monolayer graphene: Rippling, thermal expansion and elasticity," *Journal of the Mechanics and Physics of Solids*, vol. 66, pp. 42–58, 2014, ISSN: 0022-5096. DOI: https://doi.org/10.1016/j.jmps.2014.01.011.

[42] "Temperature-dependent elastic properties of single layer graphene sheets," *Materials and Design*, vol. 31, no. 9, pp. 4445–4449, 2010, ISSN: 0261-3069.

[43] H. Zhao and N. R. Aluru, "Temperature and strain-rate dependent fracture strength of graphene," *Journal of Applied Physics*, vol. 108, no. 6, p. 064 321, 2010. DOI: 10.1063/1.3488620.

[44] A. Singh and Y. Li, "Reliable machine learning potentials based on artificial neural network for graphene," *Computational Materials Science*, vol. 227, p. 112 272, 2023, ISSN: 0927-0256. DOI: https://doi.org/10.1016/j.commatsci.2023.112272.

[45] A. Singh, X. Chen, Y. Li, S. Koric, and E. Guleryuz, "Development of artificial neural network potential for graphene," in *AIAA Scitech 2020 Forum*. DOI: 10.2514/6.2020-1861.

[46] L. Gao, "Flexible device applications of 2d semiconductors," *Small*, vol. 13, no. 35, p. 1 603 994, 2017. DOI: 10.1002/smll.201603994.

[47] X. Huang, C. Liu, and P. Zhou, "2d semiconductors for specific electronic applications: From device to system," *npj 2D Materials and Applications*, vol. 6, no. 1, p. 51, Aug. 2022, ISSN: 2397-7132. DOI: 10.1038/s41699-022-00327-3.

[48] *Machine Learning Potentials for Graphene*, vol. Volume 3: Advanced Materials: Design, Processing, Characterization and Applications; Advances in Aerospace Technology, ASME International Mechanical Engineering Congress and Exposition, Oct. 2022, V003T03A036. DOI: 10.1115/IMECE2022-95341.

[49] A. Singh and Y. Li, "Uncertainty management and reduction of machine learning potential," in *AIAA Scitech 2021 Forum*. DOI: 10.2514/6.2021-1962.

[50] M. G. Rasul, A. Kiziltas, B. Arfaei, and R. Shahbazian-Yassar, "2d boron nitride nanosheets for polymer composite materials," *npj 2D Materials and Applications*, vol. 5, no. 1, p. 56, May 2021, ISSN: 2397-7132. DOI: 10.1038/s41699-021-00231-2.

[51] K. L. Kim, M. Koo, and C. Park, "Controlled polymer crystal/two-dimensional material heterostructures for high-performance photoelectronic applications," *Nanoscale*, vol. 12, pp. 5293–5307, 9 2020. DOI: 10.1039/C9NR10911K.

[52] *Development of an Artificial Neural Network (ANN) Constitutive Model for Mechanical Metamaterials*, vol. Volume 3: Advanced Materials: Design, Processing, Characterization and Applications; Advances in Aerospace Technology, ASME International Mechanical Engineering Congress and Exposition, Oct. 2022.

[53] J. Liu, D. Hui, and D. Lau, *Nanotechnology Reviews*, vol. 11, no. 1, pp. 770–792, 2022. DOI: doi:10.1515/ntrev-2022-0041.

[54] H. Mianehrow, L. A. Berglund, and J. Wohlert, "Interface effects from moisture in nanocomposites of 2d graphene oxide in cellulose nanofiber (cnf) matrix – a molecular dynamics study," *J. Mater. Chem. A*, vol. 10, pp. 2122–2132, 4 2022. DOI: 10.1039/D1TA09286C.

[55] Y. Li and G. Seidel, "Multiscale modeling of functionalized interface effects on the effective elastic material properties of cnt–polyethylene nanocomposites," *Computational Materials Science*, vol. 107, pp. 216–234, 2015, ISSN: 0927-0256. DOI: https://doi.org/10.1016/j.commatsci.2015.05.006.

[56] I. Pande, L. F. Pascual, A. Kousar, E. Peltola, H. Jiang, and T. Laurila, "Interface matters - effects of catalyst layer metallurgy on macroscale morphology and electrochemical performance of carbon nanofiber electrodes," *Diamond and Related Materials*, vol. 131, p. 109 566, 2023, ISSN: 0925-9635. DOI: https://doi.org/10.1016/j.diamond.2022.109566.

[57] J. Xu, G. Reiter, and R. G. Alamo, "Concepts of nucleation in polymer crystallization," *Crystals*, vol. 11, no. 3, 2021, ISSN: 2073-4352. DOI: 10.3390/cryst11030304.

[58] Y. Wang, G. Zou, and J. Liu, "Molecular dynamics simulation of the interfacial shear properties between thermoplastic polyurethane and functionalized graphene sheet," *Polymers*, vol. 14, no. 22, 2022, ISSN: 2073-4360. DOI: 10.3390/polym14225032.

[59] P. Snapp, J. M. Kim, C. Cho, J. Leem, M. F. Haque, and S. Nam, "Interaction of 2d materials with liquids: Wettability, electrochemical properties, friction, and emerging directions," *NPG Asia Materials*, vol. 12, no. 1, p. 22, Mar. 2020, ISSN: 1884-4057. DOI: 10.1038/s41427-020-0203-1.

[60] S. Khurshid, E. Saridakis, L. Govada, and N. E. Chayen, "Porous nucleating agents for protein crystallization," *Nature Protocols*, vol. 9, no. 7, pp. 1621–1633, Jul. 2014. DOI: 10.1038/nprot.2014.109.

[61] J. C. Wittmann and B. Lotz, "Epitaxial crystallization of polyethylene on organic substrates: A reappraisal of the mode of action of selected nucleating agents," *Journal of Polymer Science: Polymer Physics Edition*, vol. 19, no. 12, pp. 1837–1851, DOI: https://doi.org/10.1002/pol.1981.180191204.

[62] D. N. Simavilla, W. Huang, P. Vandestrick, J.-P. Ryckaert, M. Sferrazza, and S. Napolitano, "Mechanisms of polymer adsorption onto solid substrates," *ACS Macro Letters*, vol. 6, no. 9, pp. 975–979, 2017, PMID: 35650878. DOI: 10.1021/acsmacrolett.7b00473.

[63] M. Tariq, O. Dolynchuk, and T. Thurn-Albrecht, "Effect of substrate interaction on thermodynamics of prefreezing," *Macromolecules*, vol. 52, no. 23, pp. 9140–9148, 2019. DOI: 10.1021/acs.macromol.9b01499.

[64] X. Zhang, H. Yan, C. Xu, *et al.*, "Skin-like cryogel electronics from suppressed-freezing tuned polymer amorphization," *Nature Communications*, vol. 14, no. 1, p. 5010, Aug. 2023, ISSN: 2041-1723. DOI: 10.1038/s41467-023-40792-y. [Online]. Available: https://doi.org/10.1038/s41467-023-40792-y.

[65] "Physics-informed machine learning assisted uncertainty quantification for the corrosion of dissimilar material joints," *Reliability Engineering and System Safety*, vol. 227, p. 108 711, 2022, ISSN: 0951-8320. DOI: 10.1016/j.ress.2022.108711.

[66] P. Bansal, Z. Zheng, B. Pan, *et al.*, "Corrosion of al-fe self-pierce riveting joints with multiphysics-based modeling and experiments," *Journal of Manufacturing Processes*, vol. 95, pp. 434–445, 2023, ISSN: 1526-6125. DOI: 10.1016/j.jmapro.2023.04.014.

[67] P. Bansal, Z. Zheng, and Y. Li, "Uncertainty quantification for dissimilar material joints under corrosion environment," Nov. 2022. DOI: 10.1115/DETC2022-89654.

[68] P. Bansal, Z. Zheng, and Y. Li, "Uncertainty quantification on galvanic corrosion based on adaptive surrogate modeling," Feb. 2023. DOI: 10.1115/IMECE2022-95333.

[69] A. Singh and Y. Li, "Guided self-assembly of polyethene on graphene," in *AIAA SCITECH 2022 Forum*. DOI: 10.2514/6.2022-2143.

[70] V. Yamakov, D. Wolf, S. R. Phillpot, A. K. Mukherjee, and H. Gleiter, "Deformation-mechanism map for nanocrystalline metals by molecular-dynamics simulation," *Nature Materials*, vol. 3, no. 1, pp. 43–47, Jan. 2004, ISSN: 1476-4660. DOI: 10.1038/nmat1035.

[71] A. J. Bourque, C. R. Locker, and G. C. Rutledge, "Heterogeneous nucleation of an n-alkane on tetrahedrally coordinated crystals," *The Journal of Physical Chemistry B*, vol. 121, no. 4, pp. 904–911, Feb. 2017, ISSN: 1520-6106. DOI: 10.1021/acs.jpcb.6b12590.

[72] Y. Ming, Z. Zhou, and T. Hao, "Molecular simulation of crystal nucleation and growth of structurally restricted polymer nanocomposites," *Journal of Molecular Liquids*, vol. 380, p. 121 720, 2023, ISSN: 0167-7322. DOI: https://doi.org/10.1016/j.molliq.2023.121720.

[73] C. Park and G. J. Yun, "Characterization of Interfacial Properties of Graphene-Reinforced Polymer Nanocomposites by Molecular Dynamics-Shear Deformation Model," *Journal of Applied Mechanics*, vol. 85, no. 9, Jun. 2018, 091007, ISSN: 0021-8936. DOI: 10.1115/1.4040480.

[74] Q. Xiong and S. Meguid, "Atomistic investigation of the interfacial mechanical characteristics of carbon nanotube reinforced epoxy composite," *European Polymer Journal*, vol. 69, pp. 1–15, 2015, ISSN: 0014-3057. DOI: https://doi.org/10.1016/j.eurpolymj.2015.05.006.

[75] V. Iberi, L. Liang, A. V. Ievlev, *et al.*, "Nanoforging single layer mose2 through defect engineering with focused helium ion beams," *Scientific reports*, vol. 6, pp. 30 481–30 481, Aug. 2016, srep30481[PII], ISSN: 2045-2322. DOI: 10.1038/srep30481.

[76] M. Bougouma, A. Batan, B. Guel, *et al.*, "Growth and characterization of large, high quality mose2 single crystals," *Journal of Crystal Growth*, vol. 363, pp. 122–127, 2013, ISSN: 0022-0248. DOI: https://doi.org/10.1016/j.jcrysgro.2012.10.026.

[77] K.-J. Hsiao, J.-D. Liu, H.-H. Hsieh, and T.-S. Jiang, "Electrical impact of mose 2 on cigs thin-film solar cells," *Physical Chemistry Chemical Physics*, vol. 15, no. 41, pp. 18 174–18 178, 2013.

[78] J. Molnár, Z. Zuba, Ö. Sepsi, *et al.*, "Structural investigation of semicrystalline polymers," *Polymer Testing*, vol. 95, p. 107 098, 2021, ISSN: 0142-9418. DOI: https://doi.org/10.1016/j.polymertesting.2021.107098.

[79] R. S. Mohammadi, A. M. Zolali, S. H. Tabatabaei, and A. Ajji, "Nanoconfinement induced direct formation of form i and iii crystals inside in situ formed poly(butene-1) nanofibrils," *Macromolecules*, vol. 53, no. 4, pp. 1346–1355, 2020. DOI: 10.1021/acs.macromol.9b01684.

[80] A. Awad, A. Aly Abd El-Wahab, R. El-Gamsy, and M. H. Abdel-latif, "A study of some thermal and mechanical properties of hdpe blend with marble and granite dust," *Ain Shams Engineering Journal*, vol. 10, no. 2, pp. 353–358, 2019, ISSN: 2090-4479. DOI: 10.1016/j.asej.2018.08.005.

[81] A. Singh and Y. Li, "2d materials guided self-assembly of polymer: Molecular dynamics simulation study," in *AIAA SCITECH 2023 Forum*. DOI: 10.2514/6.2023-0142.

[82] P. (Yi and G. C. Rutledge, "Molecular simulation of bundle-like crystal nucleation from n-eicosane melts," *The Journal of Chemical Physics*, vol. 135, no. 2, Jul. 2011, ISSN: 0021-9606. DOI: 10.1063/1.3608056.

[83] D. Turnbull and B. Vonnegut, "Nucleation catalysis.," *Industrial & Engineering Chemistry*, vol. 44, no. 6, pp. 1292–1298, 1952. DOI: 10.1021/ie50510a031.

[84] "Epitaxial crystallization of polymers on organic and polymeric substrates," *Progress in Polymer Science*, vol. 15, no. 6, pp. 909–948, 1990, ISSN: 0079-6700. DOI: 10.1016/0079-6700(90)90025-V.

[85] A. A. Alsaygh, J. Al-hamidi, F. D. Alsewailem, I. M. Al-Najjar, and V. L. Kuznetsov, "Characterization of polyethylene synthesized by zirconium single site catalysts," *Applied Petrochemical Research*, vol. 4, no. 1, pp. 79–84, May 2014, ISSN: 2190-5533. DOI: 10.1007/s13203-014-0053-2.

[86] C. W. Bunn, "Molecular structure and rubber-like elasticity. i. the crystal structures of beta gutta-percha, rubber and polychloroprene," *Proceedings of the Royal Society of London. Series A, Mathematical and Physical Sciences*, vol. 180, no. 980, pp. 40–66, 1942, ISSN: 00804630.

[87] P. A. T. Olsson, P. Hyldgaard, E. Schröder, E. P. Jutemar, E. Andreasson, and M. Kroon, "Ab initio investigation of monoclinic phase stability and martensitic transformation in crystalline polyethylene," *Phys. Rev. Materials*, vol. 2, p. 075 602, 7 Jul. 2018. DOI: 10.1103/PhysRevMaterials.2.075602.